OPTICAL STUDIES OF SPIN-DEPENDENT PROCESSES IN FERROMAGNETS AND SEMICONDUCTORS

by

Ryan Michael McLaughlin

A dissertation submitted to the faculty of
The University of Utah
in partial fulfillment of the requirements for the degree of

Doctor of Philosophy

in

Physics

Department of Physics and Astronomy

The University of Utah

August 2017

The University of Utah Graduate School

STATEMENT OF DISSERTATION APPROVAL

The dissertation of **Ryan Michael McLaughlin**

has been approved by the following supervisory committee members:

Zeev Valentine Vardeny	, Chair	**6/5/2017** Date Approved
Christoph Boehme	, Member	**6/12/2017** Date Approved
Sarah Yan Li	, Member	**6/9/2017** Date Approved
Yong-Shi Wu	, Member	Date Approved
Luisa Whittaker-Brooks	, Member	Date Approved

and by **Benjamin C. Bromley** , Chair/Dean of

the Department/College/School of **Physics and Astronomy**

and by David B. Kieda, Dean of The Graduate School.

ABSTRACT

This dissertation documents our experimental studies of spin-dependent electronic processes in two distinct condensed-matter systems with extremely different microscopic properties.

The first of these two systems is the metallic alloy of Nickel and Iron ($Ni_{81}Fe_{19}$) known as permalloy, which is a commonly used metallic ferromagnet used routinely for spintronics applications. The field of spintronics is presently limited by the ability to generate spin currents "on demand," due to the low efficiency, high-power consumption, or difficult engineering constraints of existing techniques such as electrical spin injection, spin pumping, and optical spin alignment. One possible answer to these problems comes from the coupling between heat currents and spin currents in ferromagnets. This coupling, known as the spin Seebeck effect, might allow future spintronic devices to access a continuous supply of spin-polarized electrons simply by applying a temperature gradient to a ferromagnetic film. Analogously to the coupling between heat and charge currents (known as the Seebeck effect) that makes thermocouples and thermoelectric generators work, the spin Seebeck effect converts a heat current into a spin accumulation. We have developed and successfully applied a method for detecting this spin accumulation that is based on a highly sensitive magneto-optical Sagnac interferometer microscope, which is sensitive to spin accumulation without physical contact and without electrical artefacts. We show that this all-optical scheme can detect the elusive spin

Seebeck effect in permalloy thin films, whose existence was previously debated by the field for almost a decade.

Secondly, we have studied another system with rich potential applications to the fields of photovoltaics, computing, an potentially spintronics, which is amorphous hydrogenated silicon (a-Si:H). We have found several spin-dependent electronic processes that govern the time evolution of bound electron-hole pairs, and therefore affect the rates of radiative recombination or dissociation of those pairs. These mechanisms may be studied either optically or electrically, through the magnetic field effects on photoluminescence (PL) or photoconductivity (PC). By fabricating appropriate films and devices and testing their PL/PC efficiency at very large magnetic fields (up to 20T), we derive important conclusions about the role of the spin degree of freedom in the behavior of a-Si:H.

To Tom, for fostering my early interest in physics through a childhood rich in science fairs and kitchen engineering. To Nancy, for her unwavering support, without which I may have never graduated from high school. And to Sonoma, who provided motivation to finish experiments and come home every day

TABLE OF CONTENTS

ACKNOWLEDGEMENTS

First and foremost, I would like to acknowledge my advisor, Dr. Valy Vardeny. My graduate studies would not have been possible without his patience, wisdom, advice (both personal and professional), and sense of humor; the latter has made my five years in the group not only bearable but downright fun. I have been unbelievably fortunate to have the pleasure to work in a group with such a broad scope of scientific experiments and with such a wonderful group of mentors and coworkers. I would especially like to thank Dr. Bhoj Gautam, helped me take my first steps in the Vardeny labs, Dr. Dali Sun, who has generously mentored me with more patience than I likely deserve, and Dr. Chuang Zhang, who made the repeated adventures in Tallahassee a fun and memorable time. Most importantly, I have to thank my beautiful and endlessly supportive fiancée, Sonoma Harris, who brings chicken nuggets to the lab during all-night magnet runs and listens to my ravings with an angelic patience. Without her, this whole adventure would not have been possible.

I would also like to thank the National Science Foundation Materials Research Science and Engineering Center (NSF-MRSEC), which has generously supported by graduate studies for my entire time at the U. I feel extremely fortunate for the opportunities that MRSEC has allowed me to pursue. Extra thanks to the National High Magnetic Field Lab for their hospitality in allowing us to perform our experiments in their facilities.

CHAPTER 1

INTRODUCTION

1.1 Overview

The rich dynamics of spin-dependent phenomena in metals and semiconductors has proven a fertile ground for experimentalists and theorists alike for more than a century. This dissertation documents the experimental work on two avenues of research in spin-dependent phenomena that I have undertaken at the University of Utah.

Our first objective is to solve a long-standing mystery in the field of spin caloritronics, which is the debate over the existence of the "spin Seebeck effect" in metallic ferromagnets. Until this work, the only established experimental techniques for investigating the relationships between heat currents and spin currents was by detecting electrical voltages and currents in electrodes which were physically attached to the sample in question. It was repeatedly shown by others that these electrical measurements were unreliable at best, and at worst, the "real" spin current signals were completely overwhelmed by magneto-thermo-electric artefacts. We invented a noncontact optical measurement scheme which is immune to such electrical artefacts to conclusively show that the spin Seebeck effect is, in fact, a real process that occurs in metallic ferromagnets. Section 1.2.1 will cover the necessary theoretical background and main previous experimental results of the field of spin caloritronics, while Chapter 2 will detail the

optical scheme that is the basis of our contribution to the field. Chapter 3 will contain the results and discussion about the Optically Detected spin Seebeck effect.

As an unrelated but simultaneous avenue of research that I pursued during my time in the Vardeny group, I have looked into spin-dependent recombination/dissociation dynamics of photogenerated charge carriers in amorphous hydrogenated silicon (a-Si:H), which is an extremely well-studied and commercially applied semiconductor system that has been known for decades. Although a-Si solar cells have been manufactured on very large scales for many years (with efficiencies approaching 15%), there are still unresolved mysteries concerning spin-dependent recombination/dissociation processes that take place in the material. We have studied a-Si:H thin films and solar cell devices in very large magnetic fields (up to 25 T) and derived a successful model of the major factors influencing carrier dynamics, which depend on the carrier's energy and wavefunction localization extent. This model is comprised of the "delta-g" mechanism, the hyperfine interaction with surrounding Hydrogen and Silicon-29 nuclei, and a Drude-type magnetoresistance mechanism. The background of the a:Si field will be covered in Section 1.3, while the high-field experiments and theoretical models will be discussed in Chapter 4.

1.2 Spin Caloritronics

Spin caloritronics is a very young field, which may be loosely defined as the study of the coupling between heat and spin currents with the aim of designing next-generation devices with novel functionalities.[1,2] The field (arguably) began in 2006 with the suggestion from Hatami and Bauer[42] that a heat current at the interface between a

normal metal (NM) and a ferromagnet (FM) could be converted into a torque on the magnetization of the FM. Before Hatami and Bauer, several theorists had considered the idea that spin-dependent scattering processes might cause electrons of different spins orientations to interact differently with phonons (and heat currents) at interfaces in magnetic structures or heterostructures.[42-45] However, since the goal of creating functional devices is so integral to the field of spin caloritronics today, the suggestion by Hatami and Bauer that this interplay between heat currents and spin currents might be a *useful tool* in harnessing heat from nanoscale electronic devices and converting it into magnetization torques (which can in turn be used to store or transfer information) was a great leap forward for the field.

Since then, it has been shown that FM metals,[3-5] FM semiconductors,[6,7] FM insulators,[8-14] and even paramagnetic insulators[15-16] may generate a measurable spin current in an adjacent normal metal in the presence of a temperature gradient at the interface. The conversion from heat currents to spin currents, illustrated in Figure 1.1, was dubbed the spin Seebeck effect (SSE)[2-3], analogously with the "regular" Seebeck effect, which is the well-known coupling between heat currents and charge currents discovered in 1821 by the German physicist, Thomas Johann Seebeck. Although not discussed in detail in the context of this dissertation, it is worth noting that the inverse of the SSE (spin current converted into heat current) exists and is dubbed the spin-Peltier effect, just as the inverse of the Seebeck effect is named the Peltier effect (charge current converted into heat current) after its discoverer, Charles Athanase Peltier.

Experimental demonstrations of the spin Seebeck effect are riddled with potential artefacts due to the frighteningly large number of microscopic mechanisms that can

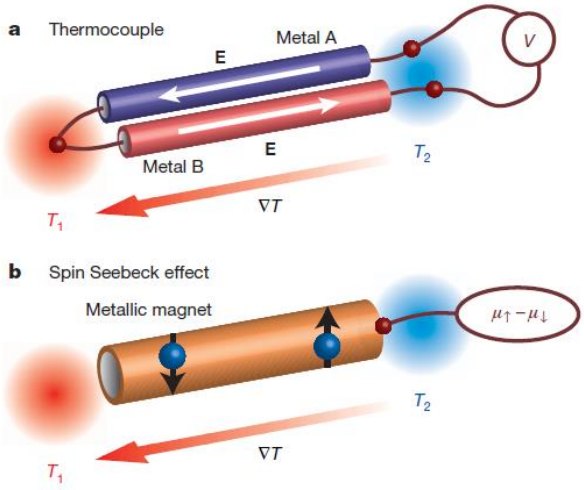

Figure 1.1. (a) Schematic illustration of the Seebeck effect, where charge carriers of opposite sign diffuse to opposite ends of a material under a thermal gradient resulting in a current and voltage. (b) Illustration of the spin Seebeck effect, where instead carriers of opposite *spin* diffuse to opposite ends of a metallic ferromagnet.[3]

generate an electromotive force (EMF) in a metal film in the presence of temperature gradients and strong magnetizations.[18] The field of spin caloritronics has seen much debate over the last decade as to the interpretations of experimental results, dating all the way back to the beginning of the field. Since these debates basically all originate from the use of metallic spin current "detection strips" and the possible electrical artefacts that originate there, our contribution to the field was our invention of a noncontact, entirely optical method for detecting temperature-induced changes in magnetization that is inherently immune to any sort of magneto-thermoelectric artefacts. In order to describe the advance to the field that was made by our novel interferometric approach (which will be the subject of Chapter 3), first it must be explained exactly how these thermally-induced spin currents have been measured up until now. Then we will examine the range of possible experimental artefacts that might interfere with these measurements which are resolved by our use of noncontact optical methods.

1.2.1 Electrically Detected Spin Currents

The concept of spin-to-charge conversion is essential to any electrical scheme for detecting spin currents, and the spin Hall effect (SHE) is central to our understanding of spin-to-charge conversion. First proposed by Russian physicists Dyakonov and Perel in 1971,[97] the spin Hall effect is the name given to the spin-dependent scattering process that results from spin-orbit coupling (SOC) at scattering sites, which allows spin current to be converted into charge currents that may be detected by regular voltage-sensing laboratory hardware.

There exists a surprisingly amount of difficulty in defining precisely what

constitutes a spin current,[98] but we must form at least a working definition before we proceed further. If the spin current is carried by a partially spin-polarized ensemble of charge carriers (this is usually a reasonable model when the spin current exists in a conducting material), then the definition of spin and charge currents is straightforward. Consider the total charge current carried through a material as the sum of the currents carried by the two spin orientations which will be denoted $J_\uparrow$ and $J_\downarrow$ (momentarily ignoring spin-flip scattering that will convert carriers from one spin channel to the other). Then the total charge current is:

$$J_c = J_\uparrow + J_\downarrow \tag{1.1}$$

And the total spin current is:

$$J_s = J_\uparrow - J_\downarrow \tag{1.2}$$

Although this definition is clearly not complete (it is not suitable to describe magnon-carried spin currents in FM insulators like Yttrium Iron Garnet (YIG)), it is a useful mental picture to visualize effects like the spin Hall effect.

Let us first describe the SHE so that we may discuss its potential limitations and possible experiments solutions to those shortcomings. For simplicity, let us consider a nonmagnetic, isotropic, conducting material with strong SOC[97] that allows the spin Hall effect to manifest. These assumptions make the mathematics easier to digest, and turn out to be entirely appropriate for the materials that are commonly used as spin detection layers (platinum, tungsten, gold, etc.). In a semiclassical picture, one can understand the SHE by picturing charge transport taking place by a Drude-like model where the electrons undergo ballistic transport between discrete scattering events. Dyakanov and Perel proposed that the differential scattering cross section $d\Omega/d\sigma$, which is the

probability that a particle impinging on a scattering site will scatter in a given direction (θ, φ) into a differential solid angle $d\Omega$ if the particles scatters from a cross sectional area element $d\sigma$, depends on the orientation of the electron's spin if spin-orbit coupling (SOC) is considered when calculating the scattering cross section. Rather than being scattered isotropically (i.e., $< k_{out} >= 0$, a common assumption in the regular Drude model), in the presence of spin-orbit coupling, the electron is preferentially scattered with a scattering wavevector $\vec{k}_{out} \propto \vec{\sigma} \times \vec{k}_{in}$ as shown in Figure 1.2.

As a result, the spin-dependent conductivity tensors will acquire off-diagonal elements, such that the sign of the off-diagonal elements is opposite for electrons with opposite spins. For a pure charge current (which is not spin-polarized, so it is composed of 50% spin "up" and 50% spin "down" electrons for any choice of quantization axis), the contributions to the off-diagonal conductivity tensor elements are equal and opposite for electrons of opposing spins, so by symmetry, the total electrical conductivity tensor is purely diagonal (again, assuming an isotropic material in zero magnetic field).

However, while the charge current is parallel with the local electric field, the *spin* current is not. The SHE causes a spin current will flow in a direction perpendicular to the charge current, as illustrated in Figure 1.3, and has been proposed as an efficient low-loss spin injection scheme which does not rely on the presence of a FM conductor. In a finite conducting material, the spin current is "bounded" by the physical edge of the conductor, and results in an accumulation of spin-polarized carriers on the lateral edges of the sample, with opposite signs on opposite edges of the sample. In fact, the spin accumulation, which falls off on the length scale of the spin diffusion length, λ_s, can be beautifully imaged using a MOKE microscope very similar to ours, as demonstrated in

gallium arsenide by Y. K. Kato *et al.*[29]

Just as the SHE converts charge currents into spin currents, the same mechanism (spin-dependent scattering cross sections) can be used to convert spin currents into charge currents, an effect dubbed the *inverse* spin Hall effect (ISHE). The ISHE is one of the most valuable tools in the spintronics experimentalist's toolbox, because it is one of only a few methods to experimentally detect spin current and spin accumulation. As illustrated in Figure 1.4, the ISHE converts a pure spin current in the x direction into a charge current in the y direction, which may be detected with a conventional ammeter. This voltage is extremely small due to the very low efficiency with which the ISHE converts spin currents to charge currents. A typical SSE measurement using platinum (Pt) spin detection strips yields a voltage of only 10^{-8} to 10^{-6} V, which is easily confounded by unavoidable magneto-thermoelectric artefacts whose magnitudes can exceed 10^{-3} V in the same measurement.

1.2.2 Nonequilibrium Physics

The field of spin caloritronics has its foundation deeply rooted in the realm of nonequilibrium physics.[24-28] In solid state physics, it is common practice to treat a real crystal as a composite system composed of multiple distinct, but interacting, ensembles of particles or quasiparticles, each described by their own statistics and thermodynamic qualities. In a silicon crystal, for example, one may conceive of the ensemble of electrons as being mathematically distinct from the lattice of silicon nuclei in which they reside. The system of phonons, or vibrations of the underlying silicon lattice, can be mathematically described separately from the system of electrons. In a ferromagnet,

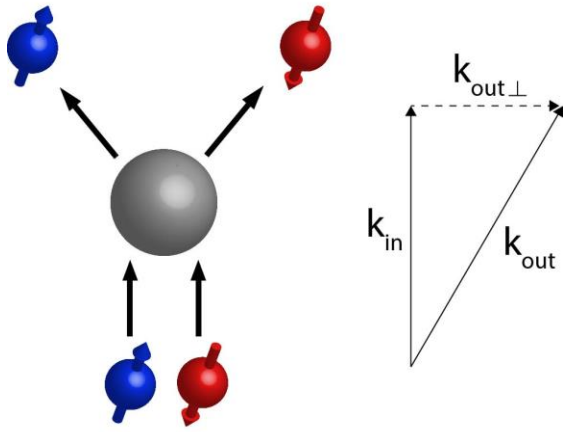

Figure 1.2. An illustration of anisotropic scattering due to spin-orbit coupling at the scattering site. A carrier of the opposite spin will be deflected in the opposite direction.

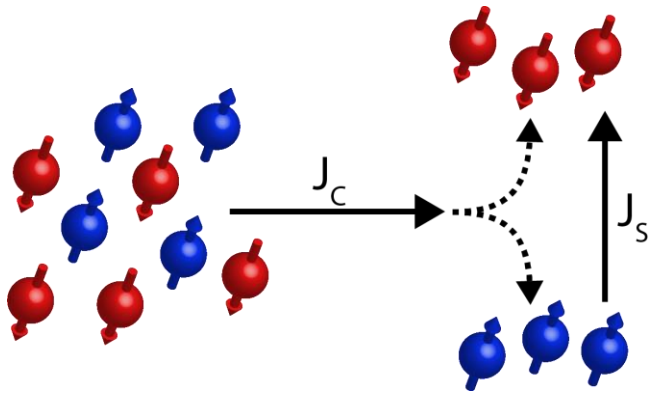

Figure 1.3. Illustration of the spin Hall effect, converting a pure charge current in the x direction into a pure spin current in the y direction.

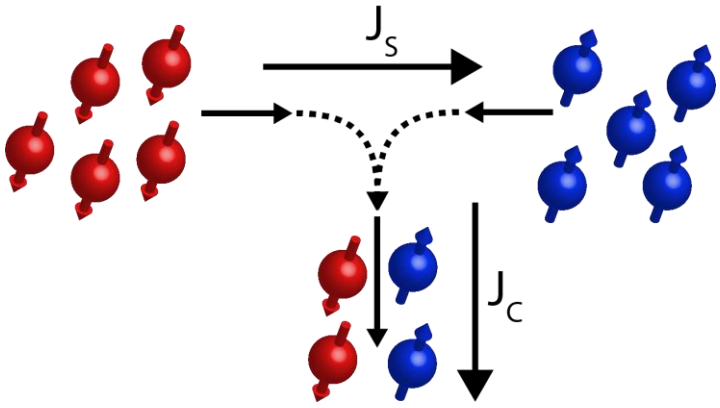

Figure 1.4. Illustration of the Inverse spin Hall effect converting a pure spin current in the x direction into a pure charge current in the $-y$ direction.

quasiparticles resulting from the spontaneous breaking of rotational symmetry by the aligned electron magnetic moments, namely magnons, can be described with their own statistics and thermodynamic behavior. This is an extremely useful abstraction in that it allows fundamental thermodynamics quantities of interest (e.g., temperature, heat capacity, thermal conductivity, etc.) to be defined and measured separately for separate subsystems (electrons, phonons, magnons) composing a real crystal. The basics of this mathematical model are taught in most introductory solid-state textbooks.

It is well known from the study of thermodynamics and statistical mechanics that, for a system in thermal equilibrium, the statistics of a collection of fermions such as electrons will follow a Fermi-Dirac (FD) distribution, while a collection of bosons such as phonons or magnons will follow a Bose-Einstein (BE) distribution.

$$\text{FD: } f(E) = \frac{1}{e^{(E-\mu)/kT}+1} \tag{1.3}$$

$$\text{BE: } f(E) = \frac{1}{e^{(E-\mu)/kT}-1} \tag{1.4}$$

Rather than relying on the formal (entropy-based) definition of temperature, it is useful for an experimentalist to imagine a measurement of an ensemble's temperature in which the energy-dependent occupation probabilities are measured, the data are fit with the appropriate statistical function (either FD or BE, depending on the type of particle), and the temperature is extracted as a fitting parameter. The temperature is said to be ill-defined if the system does not follow the appropriate statistical function for any values of the free parameters, namely the chemical potential and the temperature. One of the more interesting and useful results of this abstraction is that a single crystal, driven out of equilibrium, often cannot be described by a single temperature. Indeed, when the conditions of thermal equilibrium are not satisfied, perhaps it should not be surprising

that temperature is not easy to define. What might be surprising, however, is that the separate temperatures of the electron, phonon, magnon, etc., subsystems might be perfectly well-defined (i.e., the ensembles all obey their respective statistics), but the temperatures of the subsystems may not be equal. When that is the case, the system will try to return to thermal equilibrium by transferring energy between thermodynamic subsystems until equilibrium is restored. That transfer of energy lies at the heart of the field of spin caloritronics. One of the experimental and theoretical challenges for the spin caloritronics research community is the task of predicting and measuring the distinct temperatures of the subsystems composing a real material and learning how the rich interplay between them might result in useful behavior for the next generation of spintronic devices.

Here, we must make a distinction between two mechanisms that have been proposed to explain the spin Seebeck effect, and acknowledge that the terminology used in the literature has been inconsistent since its inception. This is probably the case with any new field, as theorists and experimentalists may not agree on a strict set of definitions and mechanisms in the infancy of the field. Recently, the spin caloritronics community has largely adopted the language and definitions specified in Bauer, Saitoh, and van Wees,[2] which will be adopted in this dissertation. According to Bauer *et al.*, any mechanism that fundamentally relies on a description of single-particle effects is dubbed a spin-*dependent* Seebeck effect (S*D*SE), whereas a description based on the collective excitations of interacting particles or quasiparticles (magnons, phonons, etc.) is dubbed the spin Seebeck effect (SSE). The mechanism based on nonequilibrium physics and the transfer of energy between magnon, phonon, and electron systems as described above

falls into the proper spin Seebeck effect category by today's terminology. It will be shown in Chapter 3 that our experiment demonstrates the nature of the effect in NiFe to be SSE, and not SDSE.

The first experimental confirmation of the SSE took place with a metallic FM and a metallic spin detection strip (NiFe and Pt, respectively), and was explained by the simultaneous action of two spin-dependent conductivity channels ("spin up" and "spin down" carriers) with Seebeck coefficients of opposite sign. In modern terminology, this would be considered a spin-dependent mechanism, and would today be dubbed the SDSE.[2] However, that explanation (illustrated in Figure 1.5) was quickly decided to be unreasonable by theorists in the field, because the SDSE is expected to function only on a length scale smaller than the spin diffusion length in the material, which is several nanometers in NiFe alloys. The enormous length scale (relative to the spin diffusion length) over which the SSE observation occurred was interpreted as evidence that collective effects of magnon/phonon heat transport was responsible.

A further distinction must be made in the naming convention of different SSE geometries, since the effect can be manifest with different relative orientations between the heat current (which is parallel to the temperature gradient) ∇T and spin current, J_s. In electrical detection schemes, the spin current is assumed be to directed out of the plane of the FM film, because otherwise it cannot reach the ISHE detection strips so that it may be detected as a charge current at the electrodes. The heat current, however, has an extra degree of freedom in that it can be directed either in-plane and perpendicular to the resulting spin current, or out-of-plane and parallel to the spin current. The standard terminology in the field, which will be adopted for the rest of this dissertation (shown in

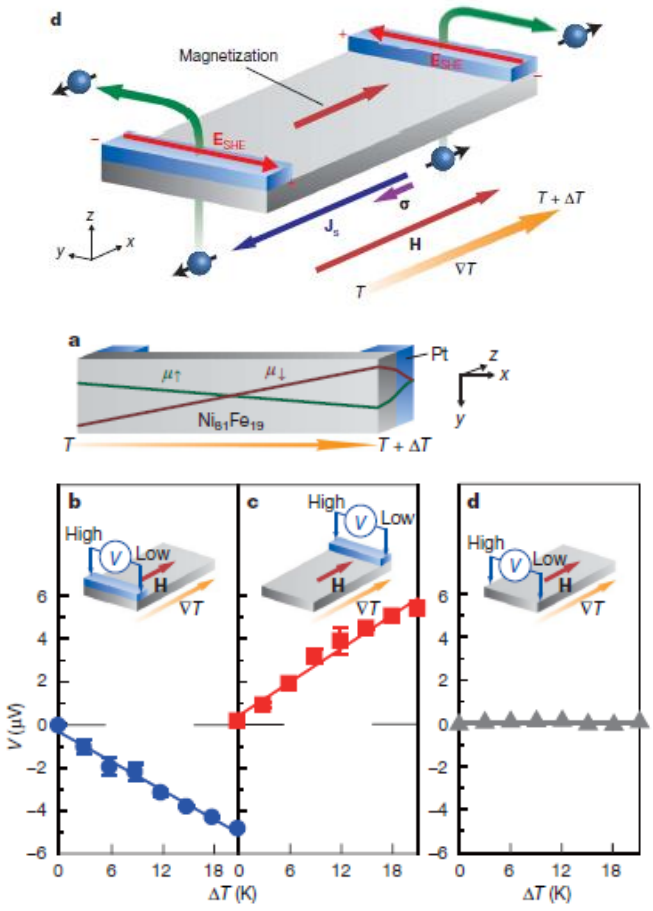

Figure 1.5. The first claimed experimental observation of the transverse spin Seebeck effect (TSSE) in a $Ni_{81}Fe_{19}$ metallic FM by Uchida *et al.*
Reprinted by permission from Macmillan Publishers Ltd: K. Uchida, S. Takahashi, K. Harii, J. Ieda, W. Koshibae, K. Ando, S. Maekawa, and E. Saitoh, Nature **455**, 778 copyright 2008.

Figure 1.6), is that the geometry with the heat current out-of-plane, collinear with the spin current, is dubbed the Longitudinal spin Seebeck effect (LSSE). The geometry with the heat current in the plane of the film, perpendicular to the resulting spin current, is dubbed the transverse spin Seebeck effect (TSSE).[3,6-8] In either case, the direction of the magnetization of the film is taken to be the quantization axis of the carrier spins, and the resulting ISHE current in the detection strips is perpendicular to both the spin current and the film magnetization direction. For reasons that will be explained shortly, the experimental confirmation of the LSSE through electrical detection is more straightforward than measurements concerning the TSSE, which is more susceptible to contamination by electrical artefacts.[17-21]

Since the groundbreaking paper in 2008 from Uchida et.al.[3] that first sought to establish the SSE as experimental fact, experimentalists have attempted to measure the spin accumulation due to the SSE by use of a "spin-detection layer" adjacent to the FM layer. The material used for the spin detection strip must be chosen carefully, since the strength of the ISHE charge current scales with the SOC of the material. Platinum is conventionally chosen as the spin detection layer, although tungsten or other elements with high atomic number Z have also been proven to work.

A typical measurement of the transverse SSE is shown in Figure 1.5. The spatial distribution of the SSE-induced spin accumulation is inferred from the magnitude and sign of the ISHE voltage on the detection strips, which can be placed at any distance along the film. The most surprising result from the TSSE experiments is that the measured spin accumulation is a function of position on the strip, which is typically several millimeters across. The length scale of this distribution of spin accumulation is

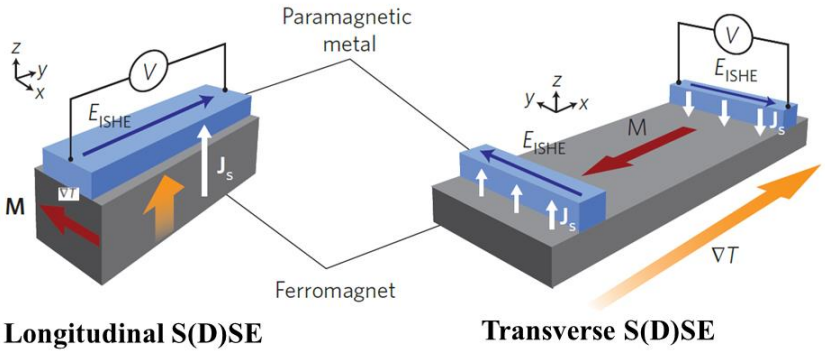

Figure 1.6. Distinction between the longitudinal SSE (LSSE) and the transverse SSE (TSSE). Note that the spin current J_s is restricted to being out-of-plane in order to be injected into the spin-detection layer, leaving only two geometries where the heat current is either in-plane or out-of-plane.
Reprinted by permission from Macmillan Publishers Ltd: K. Uchida, S. Takahashi, K. Harii, J. Ieda, W. Koshibae, K. Ando, S. Maekawa, and E. Saitoh, Nature 455, 778 copyright 2008.

many orders of magnitude larger than the most obvious physical length scale concerning spatial distribution of spins, which is the spin diffusion length (~3nm in NiFe!). This large discrepancy between the "expected" length scale of the spin Seebeck effect and the results of the real experiments led many early investigators to consider alternate explanations for the observed spatially-dependent voltage other than thermally induced spin accumulation as the original authors claimed; that search includes both experimental artefacts and novel mechanisms that might be responsible for real spin accumulation. We will discuss several magneto-thermo-electric artefacts now, approximately in order from less difficult to more difficult to eliminate.

The most obvious mechanism that produces a voltage in the presence of a temperature gradient in the Seebeck effect, which is the underlying mechanism behind thermoelectric generators and thermocouple devices. The electric field produced by the Seebeck effect has the form:

$$E_{Seebeck} = -S\,\nabla T \tag{1.5}$$

where S is a material-dependent quantity known as the Seebeck coefficient and ∇T is the local temperature gradient. There are several straightforward experiments and mathematical arguments that can convincingly prove that the observed voltage in NiFe in a typical SSE experiment is not simply an artefact due to the Seebeck effect. The first feature that emerges after inspection of equation 1.5 is that the Seebeck voltage, V_S, depends only on the difference in temperature between the two contact points on the film, and not on the magnetization. Since the signal is consistently shown to be an odd function of the magnetization of the film, it cannot be accounted for by the Seebeck effect alone.

Furthermore, the Seebeck effect is not expected to manifest in these experiments

due to the geometry of the experiment. The desired temperature gradient in a typical TSSE experiment is purely in the y direction (by the coordinate convention illustrated in Figure 1.6) so that, ideally, $dT/dx = 0$ and therefore $V_S = 0$. However, there are always some experimental imperfections in any real sample, and we must entertain the possibility that $dT/dx \neq 0$ in the experimental reports of SSE voltage in NiFe. If that were the case, however, we should expect the sign of V_s (and of dT/dx) to be as random as the fluctuations from sample to sample and from group to group, but the sign of the SSE effect (for a given material and spin-detection layer) is found to be fixed. For these reasons, it is simply not possible that the experimental observations of SSE voltage in NiFe are due to the ordinary Seebeck effect. Clearly, since V_{SSE} is observed to change with the magnetization of the film, the only plausible artefacts are those that have some dependence on M.

The Hall effect is the name given to the well-known effect where charge carriers moving in a magnetic field are affected by the Lorentz force and their path is diverted from the direction of the local electric field. By this mechanism, the conductivity tensor acquires off-diagonal elements so that the current has a component perpendicular to both E and B. The strength of the Hall effect is quantified by the Hall coefficient, which is defined as the ratio between the induced electric field and the product of the current density and the local magnetic field:

$$R_H = \frac{E_y}{J_x B_z} \tag{1.6}$$

This effect is greatly exaggerated in FM metals due to spin-orbit coupling, so that the measured Hall coefficient in materials like NiFe are many orders of magnitude larger than one would expect from a simple approximation like the Drude model, leading to the

term *Anomalous* Hall effect in FM metals.

The Nernst effect is the name given to the magneto-thermoelectric artefact which can be thought of as the combination of the Hall effect and the Seebeck effect. In the presence of a temperature gradient in a metal, the Seebeck effect (and Seebeck coefficient) describes how current flows parallel to ∇T. Meanwhile, the Hall effect (or Anomalous Hall effect, if applicable) describes how the conductivity tensor acquires off-diagonal elements in the presence of a magnetic field (or magnetization). In the presence of both a temperature gradient and a local magnetic field, the Nernst effect describes the current that flows perpendicular to both ∇T and B, which is quantified by the Nernst coefficient N, which can be thought of as the electric field induced per magnetic field strength unit, per temperature gradient unit so that it has units of $\frac{Volts}{centimeter} / (Telsa * \frac{Kelvin}{meter})$:

$$|N| \equiv ({}^{E_y}\!/_{B_z})/({}^{dT}\!/_{dx}) \tag{1.7}$$

As shown in Figure 1.6, the Nernst voltage should be irrelevant to SSE experiments because the experiment is designed so that ∇T is parallel to B, so that $V_{Nernst} \propto \nabla \mathrm{T} \times \mathrm{B} = 0$. However, not only is there a possibility for slight sample misalignment in the magnetic field or errors in fabrication that make the product $\propto \nabla \mathrm{T} \times \mathrm{B} \neq 0$, but there is the possibility of an accidental *out-of-plane* thermal gradient, which would produce a voltage *with the same direction, angular dependence, magnetization dependence, and thermal gradient dependence as the actual spin Seebeck effect.* This EMF produced by an unintentional out-of-plane gradient is termed the *anomalous* Nernst effect (ANE), and is a seriously frightening possibility for the spin caloritronics

community.

Researchers in the early days of SSE research realized that the out-of-plane thermal gradient might be influenced by heat carried away by the atmosphere at the surface of the device, leading to the surface being colder than the bulk of the film and a nonzero dT/dz, so a possible control experiment would be to remove the atmosphere by performing the experiment under vacuum. However, the SSE-like voltage persisted, and it was realized that heat transfer from the surface by radiation still exists, but also that the spin-detection strips on top of the FM film might act as an unintentional heat sink, draining heat from the FM film and creating the out-of-plane thermal gradient that produces the ANE. That possibility creates a serious conundrum: either keep the electrical detection strips and introduce the ANE (which cannot be separated from the "true" SSE voltage by any temperature or angular dependence), or remove the spin detection strips and remove the ability to measure the spin accumulation. Al alternative control experiment that has been tried with mixed results is to replace the Platinum spin-detection strips with a similar material (similar in terms of electrical/thermal conductivity, heat capacity, etc.) that lacks spin-orbit coupling so that the ISHE voltage will be absent, but presumably the Seebeck and/or Nernst and/or ANE voltage would persist. This approach has proven inconclusive in several studies, where an SSE-like voltage (with the appropriate magnetic field direction and temperature dependence) persists, but with a slightly different amplitude than those experiments that used Pt spin-detection strips. This indicates that the ANE at least plays some role, but it is likely that the observed signal is composed of an inseparable combination of ANE and SSE contributions.

The resolution to this conundrum was realized by our work with the Magneto-Optic Sagnac interferometer, which has sufficient sensitivity and stability to measure the spin accumulation induced by the SSE *without physical contact*, meaning that the out-of-plane thermal gradient induced by the metal contacts does not exist and therefore suppresses the ANE. The measurement of the spin accumulation is instead inferred from the tiny rotation of the plane of polarization of a beam of light that is reflected from the surface of the sample, dubbed the magneto-optic Kerr effect. With no physical contact or voltage measurement, the collection of magneto-thermoelectric artefacts that has plagued the spin caloritronics community from the beginning is no longer a concern. In addition, the possibility of new measurement geometries that were previously not possible with electrical detection are opened with the optical detection methods applied by our group. Due to the directionality of the ISHE voltage ($V_{ISHE} \propto \sigma \times J_s$), the magnetization was previously restricted to being in-plane only. With optical detection, both the magnetization and the thermal gradient are allowed to point at any angle, allowing us to explore new information in the anisotropy of the spin Seebeck effect.

Furthermore, because the heating of the sample due to the laser can in principle interfere with the desired thermal gradient that is under study in a SSE measurement, the extraordinarily low power of the Sagnac interferometer laser (~10μW) is an invaluable asset. Even with 10μW of laser power incident on the sample (of which only ~5% is absorbed), the Sagnac noise levels are an impressive ~200$nRad/\sqrt{Hz}$. This engineering feat is shown to be the breakthrough needed to confirm the existence of the true SSE in NiFe films, and will be more fully discussed in Chapter 3.

1.3 Amorphous Silicon

Silicon is, of course, probably the most studied and commercially developed material system known to humankind. The most commercially relevant form of silicon is undoubtedly crystalline silicon (c-Si), which forms the basis of the vast majority of computing architecture in the modern world. Crystalline silicon also has a strong hold in the photovoltaics (PV) market, where the efficiency of c-Si PV cells routinely exceeds 24% or more. However, c-Si is fairly expensive and time-consuming to produce, since it requires very clean Chemical Vapor Depositoin (CVD) processes at very high temperatures to produce electronics-quality crystalline or polycrystalline thin films that are suitable for PV applications. If one attempts to deposit a silicon film by CVD at lower temperatures, the resulting film is found to be not crystalline but amorphous, with a large density of defects and dangling bonds that make the material unsuitable for semiconductor applications. This amorphous silicon (a-Si) was not considered a serious competitor for PV applications until 1969, when Chittick, Alexander and Sterling found that a-Si thin films deposited from a Silane (SiH_4) gas precursor had a much higher photocurrent (PC) efficiency than was previously reported.[111] It was discovered by Raman spectroscopy that the hydrogen atoms bonds with the dangling bonds in the Silicon network, passivating them (Figure 1.7) and drastically reducing the rate of nonradiative recombination through the mid-gap states created by dangling bonds. Despite early difficulties in doping amorphous silicon, by the mid-1970s, hydrogenated amorphous silicon (a-Si:H) was being commercially developed for lower cost (albeit lower efficiency) photovoltaics, largely due to the breakthrough by LeComber and Spear that allowed p-type or n-type doping in a-Si:H by diborane or phosphine, respectively.

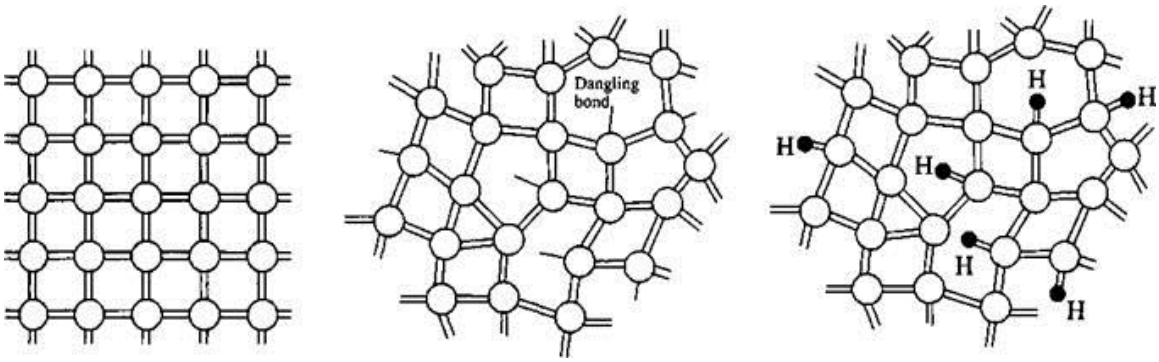

Figure 1.7. Structures of crystalline silicon (c-Si), nonhydrogenated amorphous silicon (a-Si), and hydrogenated amorphous silicon (a-Si:H).

Modern techniques allow for 13-14% power conversion efficiency (PCE) a-Si:H solar cells to be made for a fraction of the price of their c-Si counterparts. There is even promising research into hybrid c-Si/a-Si cells, where the a-Si is primarily used for surface passivation of the c-Si.[53]

Although c-Si is arguably the most well-understood material system in condensed matter, a-Si:H is a surprisingly different beast and most of the understanding of c-Si simply does not transfer to its amorphous cousin. This is because the energetic structure, transport, recombination, etc., in c-Si is very well described by the band structure formalism of quantum mechanics. On a deeper level, this is because the periodic potential imposed on the electron in a c-Si lattice is highly predictable and is known to extreme precision. Small deviations from the regular periodicity of the Si lattice (dopants, defects, interfaces, etc.) are easier to study when the rest of the c-Si structure is known in such great detail. Amorphous silicon, on the other hand, has no regular periodic structure to assist in studying it. The mathematical convenience of the band structure is absent, and the microscopic details about charge transport and recombination are either so complicated that no useful generalizations can be made (with some notable exceptions), or they simply cannot be studied in detail because only "average" effects are observed when measuring a real a-Si:H sample in the macroscopic limit.[82] Despite these difficulties, however, we will see that there are many interesting conclusions that can be made about the microscopic physics of a-Si:H by taking inspiration from the study of amorphous organic semiconductors[104].

The charge transport and recombination kinetics of a-Si:H are very different from c-Si, and are actually closer in spirit to the organic polymers and small molecules that

have been studied in detail for the last ~20 years in the organics community.[68] In c-Si, and indeed in any periodic potential, the solutions to the Schrodinger equation for free carriers (i.e., those with sufficient energy to move between periodic sites) are delocalized with a mathematical form:

$$\psi(\vec{r}) = e^{i\vec{k}\circ\vec{r}}u(\vec{r}) \tag{1.8}$$

Such energy eigenstates of periodic potentials were explored by Swiss physicist Felix Bloch in the 1920s and today are known as Bloch states or Bloch wavefunctions. Since the function $u(\vec{r})$ in solutions of this type must have the same periodicity as the underlying lattice and $e^{i\vec{k}\circ\vec{r}}$ is simply a plane wave, one can see that a wavefunction of this form is, in the approximation of an infinite lattice, infinitely delocalized. In a real crystal, of course, the wavefunction cannot have infinite extent because the crystal potential is interrupted by the boundaries of the sample, nor it is truly periodic insofar as defects, lattice vibrations, dopants (intentional or unintentional), and other perturbations are unavoidable. Nonetheless, Bloch wavefunctions in c-Si can extend over thousands of units cells and are considered highly delocalized.

Amorphous materials are defined by their disorder on a microscopic scale, and this disorder in the potential landscape leads to localization of the wavefunction. As early as 1958,[100] Philip Anderson noted that an electron in a three-dimensional (3D) "square wave" periodic potential, whose depth was allowed to vary randomly about some central value, would no longer have eigenstates that look like a Bloch state but instead would become localized. Although this simplified model clearly avoids the nuances of real materials like a-Si:H, it retains many of the essential properties of amorphous materials. In fact, the existence of these localized states, along with the exponential decrease in their

density away from the band edge (Figure 1.8), is one of the few "universal" properties[82] of amorphous materials. These localized states inside the gap are known as band tail (BT) states. Because carriers will rapidly thermalize to these lower BT states even if they are initially photoexcited or injected with higher energy, transport and recombination kinetics are determined almost entirely by the properties of the band tails.[47]

Charge transport in a-Si:H is typical for amorphous materials in that it is dominated by hopping or tunneling between localized BT states. The mobility of carriers is strongly dependent on their energy,[84] which makes intuitive sense because it is energetically unfavorable for carriers to "hop" to states with higher energy than their current state (although this can occur as a thermally activated process). Since the density of states decays exponentially inside the bandgap, many carriers will eventually get "stuck" on a deep trap until they eventually recombine. For this reason, thermally activated hopping[72] to higher energy localized BT states is necessary for conduction to occur in a-Si:H. The relationship between conductivity and temperature in amorphous systems,[82] including a-Si:H, is described at low temperatures by the variable range hopping (VRH) formula:

$$\sigma(T) = \sigma_0 e^{-(T_0/T)^p} \tag{1.9}$$

where p is a constant typically between ¼ (Mott type[101]) and ½ (Efros-Shklovskii type[109]) that depends on the process limiting the hopping rate, and T_0 is a temperature scale that depends on the density of states at the Fermi level and the localization length of localized carriers. In fact, this exponential dependence of the conductivity on temperature due to the VRH mechanism is another "universal" property of amorphous systems and is well-known in the field of amorphous organic electronics.

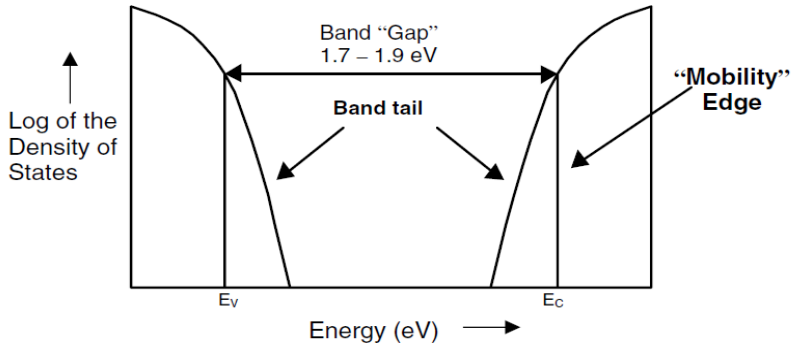

Figure 1.8. Density of states (DOS) plot for a-Si:H. The band tail (BT) states extend into the gap with an exponential decay law away from the band edges.

The fact that conduction in a-Si:H is well-described by VRH, just like organic semiconductors, is a good hint that we should take inspiration from the world of organics if we want to investigate spin-dependent optoelectronic processes in a-Si:H.[72]

1.3.1 Magnetic Field Effect Spectroscopy

Magnetic field effect (MFE) spectroscopy is a very powerful tool for studying spin-dependent physics in semiconductors. The experimental arrangement is generally very straightforward; one fabricates a film or device to study, and measures the change in the rate of some optical/electronic process as an external magnetic field is applied to the sample. If the sample under study is a film or crystal that is only amenable to optical studies, then the quantifiable metric for the optical/electronic process might be regular absorption, photoinduced absorption, photoluminescence intensity, or photoluminescence polarization. If the sample under study can be fabricated into a device structure, then the metric might be (dark) conductivity, photoconductivity, power conversion efficiency, electroluminescence, mobility, and more. The relative increase or decrease in the rates of these processes in an applied magnetic field can reveal the underlying spin-dependent mechanisms that govern recombination, dissociation, and transport in materials. In our study of a-Si:H, two MFE spectroscopies will be used: Magneto-Photoluminescence (MPL) and Magneto-Photoconductivity (MPC):

$$MPL(B) = \frac{PL(B) - PL(0)}{PL(0)} \tag{1.10}$$

$$MPC(B) = \frac{PC(B) - PC(0)}{PC(0)} \tag{1.11}$$

These two measurements are complimentary in the sense that any change in a spin-dependent recombination or dissociation rate is often reflected oppositely in PL and PC.

For example, if the application of a magnetic field increases the probability for an electron-hole pair to radiatively recombine, we should see an increase in PL ($MPL(B) > 0$) and a corresponding decrease in PC ($MPC(B) < 0$), which intuitively makes sense because the total population available to dissociate into free carriers is reduced if more e-h pairs recombine. However, in a-Si:H, the PL and PC measurements can be thought of as probing *two disjoint sets* of photogenerated carriers, because those e-h pairs that recombine generally do so from within a BT states where they are too "trapped" to effectively participate in charge transport, whereas the carriers that do participate in charge transport have higher energy on average (above or near the mobility edge), and so their kinetics may be different from carriers in the BT.

In crystalline materials like c-Si, exciton binding energies E_b are on the order of 10meV and do not drastically affect recombination, especially at higher temperatures where $k_B T > E_b$ where excitons do not remain bound due to thermal dissociation and recombination is generally well-described by band-to-band transitions. Conversely, in amorphous organic materials, recombination is strongly spin-dependent, largely because the recombination process is excitonic with the exciton binding energies E_b on the order of several hundred meV in typical organic semiconductors. That large binding energy, and the close proximity of localized carriers that it implies, leads to a very strong exchange interaction between bound charge carriers. The exchange integral J is written in the position-space basis as:

$$\int \psi_1^*(r_1)\psi_2^*(r_2)\frac{1}{|r_1 - r_2|}\psi_1(r_2)\psi_2(r_1)d^3r_1 d^3r_2 \tag{1.12}$$

It is clear from the form of J that the exchange integral will be large if the carriers are "close" in the sense that their wavefunctions overlap strongly and are localized in space

due to the $1/|r_1 - r_2|$ term in the integral. The exchange interaction determines the energy splitting between the singlet and triplet manifold for a pair of spin-1/2 particles. For a system composed of a spin-1/2 electron and a spin-1/2 hole, each with two possible spin orientations which will be represents as $\uparrow$ ($|\, s,\ m_s > = |\, 1/2,\ 1/2 >$) and $\downarrow$ ($|\, s,\ m_s > = |\, 1/2,\ -1/2 >$, there are four possible spin states which may be written in the single-particle spin basis as $\uparrow\uparrow$, $\downarrow\uparrow$, $\uparrow\downarrow$, and $\downarrow\downarrow$. We may instead use the total spin $S = 1$ of the two-particle system as the basis for writing these four states, which is convenient for a bound e-h pair or exciton. In this combined basis, we have three states with a $S = 1$ (the "triplet" states):

$$|\, 1, 1 > = \uparrow\uparrow$$

$$|\, 1, 0 > = \downarrow\uparrow + \uparrow\downarrow$$

$$|\, 1, -1 > = \downarrow\downarrow$$

There is one state with $S = 0$ (the "singlet" state):

$$|\, 0, 0 > = \downarrow\uparrow - \uparrow\downarrow$$

The distinction between the singlet and triplet spin manifolds is important for two reasons. First, the energy splitting between the singlet and triplet states E_{S-T} is equal to twice the exchange integral J, so it is energetically favorable for the e-h pair to be in the triplet manifold. Second, only the singlet state is strongly optically coupled to the ground state, because the change in the total spin quantum number ΔS must equal zero for electric dipole transitions. Therefore an exciton or e-h pair in the singlet state is significantly more likely to undergo radiative recombination to the ground state than an exciton or e-h pair in the triplet state. Likewise, triplets are more likely to dissociate into free carriers and contribute to electrically detected measurements (e.g.,

photoconductivity). The application of an external magnetic field can influence the inter-system crossing (ISC) rate between the singlet and triplet manifold (the exact mechanics of which will be explored in Chapter 4) and influence the recombination or dissociation rate, which will be experimentally detected as an increase or decrease in the luminescence or current. Because the exchange integral J is significant only when carriers are localized and the two wavefunctions strongly overlap, amorphous materials have the potential for strong exchange interactions and therefore are likely to exhibit large spin-dependent effects. Indeed, at least three separate spin-dependent effects are found to manifest in a-Si:H, which will be discussed in detail in Chapter 4.

CHAPTER 2

EXPERIMENTAL METHODS

2.1 Overview of Experimental Methods

The work presented in Chapter 3 of this dissertation (Optically Detected spin Seebeck effect) was completed using the custom-built Magneto-Optic Sagnac Interferometer microscope, while the work presented in Chapters 4 and 5 were completed using conventional optical spectroscopic techniques (i.e., noninterferometric techniques) in high magnetic field, low-temperature systems at the University of Utah and at the National High Magnetic Field Laboratory (NHMFL). This Chapter will go into detail about both experimental techniques, beginning with the Sagnac Interferometer Microscope.

2.2 Magneto-Optics

The magneto-optic Kerr effect is the rotation of the plane of linear polarization after being reflected from the surface of a material with a nonzero magnetization. The magneto-optic Faraday effect is the related effect where the magnetized material is transparent to electromagnetic radiation, so the effect is measured by transmission rather than reflection. The underlying mechanism for both Kerr and Faraday rotation is circular birefringence induced by a magnetic field, meaning that the refractive index of the

material under study is not equal for circularly polarized light of opposite handedness. To see why a circular birefringence results in the rotation of a linearly polarized beam, let us first examine the relationship between linear and circular polarizations of light. Linearly polarized light can be equivalently described mathematically as the sum of two circularly polarized beams with a specific amplitude and phase (Figure 2.1). Without loss of generality, consider a plane wave polarized in the $\hat{y}$ direction and travel in the $\hat{z}$ direction. The electric field may be written:

$$\vec{E}(x,y,z,t) = E_0\hat{y}\sin(\omega t - k_z z) = \tag{2.1}$$

$$\underbrace{\frac{E_0}{2}(\hat{y}\sin(\omega t - k_z z) + \hat{x}\cos(\omega t - k_z z))}_{\textbf{Left Circular Polarized}} + \underbrace{\frac{E_0}{2}(\hat{y}\sin(\omega t - k_z z) - \hat{x}\cos(\omega t - k_z z))}_{\textbf{Right Circular Polarized}}$$

If this linearly polarized beam travels through a volume possessing circular dichroism, the left circular polarized (LCP) and right circular polarized (RCP) components (initially with equal amplitudes $A_{Li} = A_{Ri} = E_0/2$) will emerge with difference amplitudes $A_{Lf} = A_{Rf}$ and phases φ_L and φ_R. The resulting polarization state will in general be elliptical and rotated, where the rotation angle of the major axis is $\theta = \frac{1}{2}(\varphi_L - \varphi_R)$ and the ellipticity $h = (A_{Lf} - A_{Rf}/A_{Lf} + A_{Rf})$. In most cases, the difference in absorption coefficients for LCP and RCP light is negligible, and only the rotation of the plane of polarization should be measured. Notable exceptions to this generalization occur near resonant transitions, e.g., at the band-edge in a semiconductor with significant spin polarization.

By this reasoning, the Kerr/Faraday rotation angle can be interpreted "geometrically" as a rotation of a plane by an angle θ, or it can be interpreted as a phase

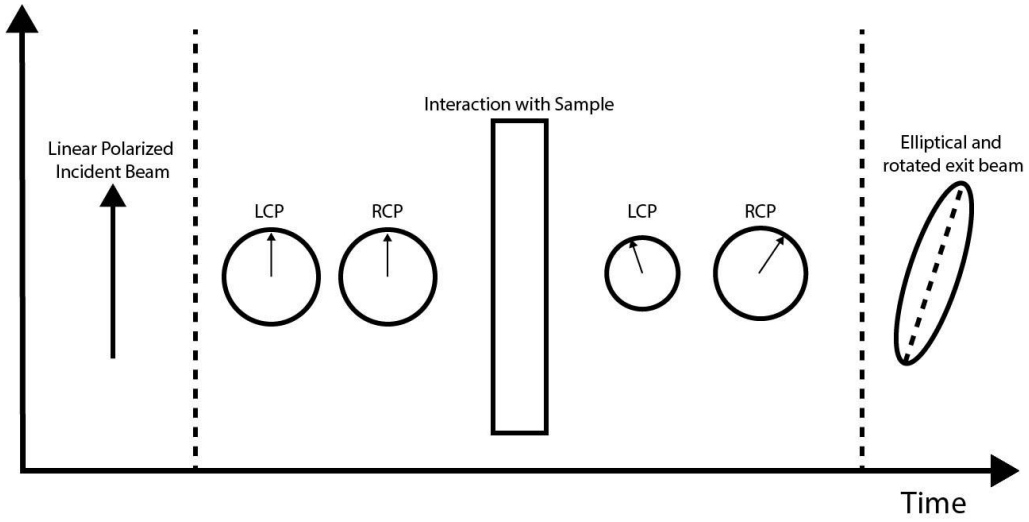

Figure 2.1. LCP and RCP light, initially with equal intensities and zero phase difference, emerge from a circularly birefringent sample with difference intensity and phase. The resulting beam is elliptical and rotated.

shift $\varphi_L - \varphi_R$ between the RCP and LCP components that constitute a linearly polarized beam. The two interpretations are of course mathematically identical, but the "phase shift" interpretation lends itself to the experimental tool of interferometry, which allows for many tricks to improve accuracy, eliminate drift, and reject unwanted sources of signal and noise as compared to a polarimetric scheme.

As discussed in the introduction (Section 1.2), the magneto-optic Kerr effect (MOKE) is a very sensitive probe of surface magnetization which is inherently noncontact and nondisruptive to the sample that is being measured, provided that the optical power of the probe is not so large as to induce heating effects in the sample. The Kerr effect (or Faraday effect, depending on the geometry) is, in its simplest form, very straightforward to measure. In fact, the rotation of the plane of polarization of a collimated light beam travelling through a dense flint glass in the presence of a magnetic field was one of the major discoveries of Michael Faraday, who in 1845, first measured the effect which now bears his name. Using a conventional polarimetric optical scheme, as illustrated in Figure 2.2, one can measure polarization rotation angles on the order of 1°, limited by the sensitivity with which one can measure the angle of the "analyzer" polarizer. This scheme has applications in optical telecommunications, where a magnetic field acting on a material with a large Verdet constant can act as an "on/off" switch for a beam of light (with a large rotation angle of 90°), but has limited use as a tool to investigate subtle physical phenomena.

There are, of course, many improvements that can be made to the sensitivity to a conventional (i.e., noninterferometric) MOKE setup. Since one of the largest sources of uncertainty in the primitive setup pictured in Figure 2.2 is the angle of the analyzing

polarizer, which is assumed to be manually controlled, the first obvious choice is to remove human uncertainty by a employing an electro-optic modulator (EOM) or photo-elastic modulator (PEM) before the analyzing polarizer, shown in Figure 2.3. The EOM/PEM acts as a variable wave plate that introduces a phase delay to one axis, called the slow axis, with respect to light travelling on the fast axis of the EOM crystal. This phase delay is proportional to the voltage applied to the EOM crystal (or the strain in the PEM crystal) and can be very accurately controlled, as well as being made time-dependent by applying an alternating current (AC) voltage to the crystal. The use of an AC polarization modulation, in addition to lock-in amplification, serves to reject many sources of noise or electrical contamination (e.g., cross-talk with 60Hz wall power) that might otherwise interfere with the measurement. Other sources of noise, for example in the amplitude of the light source, can be further reduced by replacing the simple polarization analyzer with a polarizing beam splitter (PBS) and balanced photodiodes.

MOKE measurement schemes similar to the one above are already used routinely in state-of-the-art physics research. In fact, it may seem pointless to try to improve these schemes, since shot-noise limited performance at fairly low optical powers (~$100\mu W$) are already achieved routinely, resulting in a Kerr (or Faraday) rotation equivalent noise on the order of several $nRad/\sqrt{Hz}$. However, a common theme among these measurements is that the source of Kerr (Faraday) Rotation is either modulated as a known AC frequency, allowing for the benefits of lock-in amplification for noise rejection, or are pump-probe measurements where it is only the *transient* polarization behavior that is desired, not the direct current (DC) polarization "background" angle. DC measurements are prone to drift, typically by several μRad, which is not acceptable for

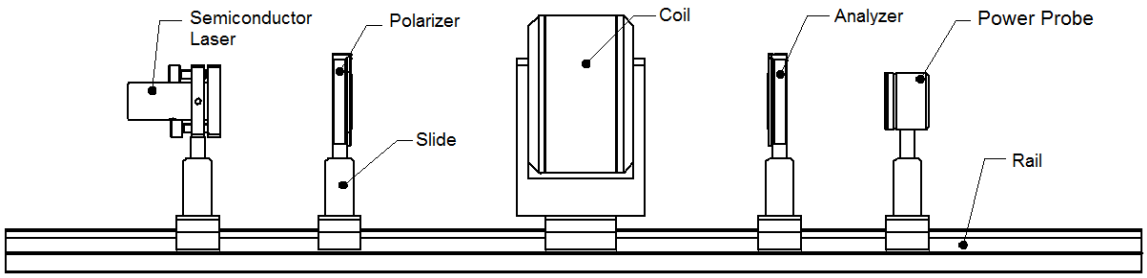

Figure 2.2. Basic polarimetric MOKE using a manually controlled analyzing linear polarizer.

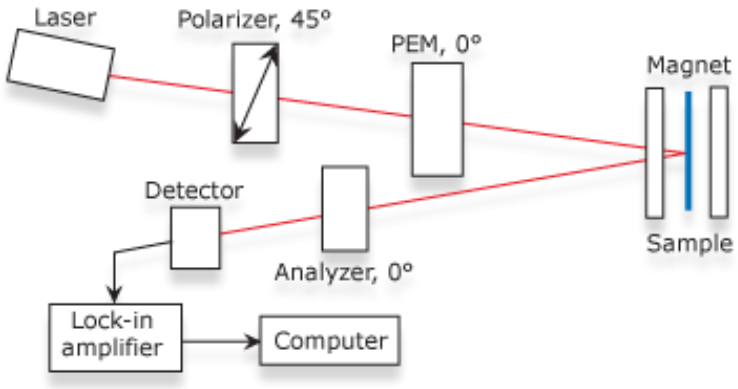

Figure 2.3. Improved MOKE setup employing polarization modulation (photoelastic modulator) and lock-in detection.

our measurements.

It was initially the goal of Aharon Kapitulnik's group at Stanford University to improve upon the DC sensitivities of modern MOKE schemes. The researchers in the Kapitulnik group[95] were interested in using MOKE as a tool to measure spontaneous time-reversal symmetry breaking (TRSB) in unconventional type II superconductors. Since TRSB in condensed matter systems usually (though not always) results in a macroscopic magnetic ordering, their quest was equivalent to measuring very small magnetizations in films at extremely low temperatures. The temperature of their samples cannot be modulated at any frequency that would be useful for lock-in detection, since lock-in detection suffers from "1/f" noise at low frequencies. Since the TRSB state of a material is quasi-static (determined by the temperature of the crystal), all the benefits of AC modulation of the source of the Kerr rotation are impossible to apply. Instead, the Kapitulnik group invented an interferometric approach[88] which, properly implemented, cancels out all experimental effects except for those which violate time-reversal symmetry, i.e., magnetization. This scheme, which is detailed in this Section, is indispensable for measuring quasi-static Kerr Rotation sources. Since the field of spin caloritronics deals exclusively with temperature-dependent magnetizations and spin currents, we realized that the Sagnac interferometer has the potential to make very important contributions to the field.

2.2.1 The Sagnac Interferometer

The construction of the Sagnac interferometer at the University of Utah began in the Spring of 2013, with the very generous help of the experts at the Kapitulnik lab. Most

of the technical details about the construction and operation of the Sagnac interferometer will be left to references 88, 95, and to the excellent PhD dissertation of Dr. Jing Xia[96], which was invaluable during the construction and troubleshooting of our interferometer. A brief overview of the history, theory of operation, construction, and improvements made to the interferometer (namely the scanning microscope extension) will be detailed in this dissertation.

The original Sagnac interferometer, invented in 1912 by French physicist Georges Sagnac[93] and illustrated in Figure 2.4, was intended to detect "the effect of the relative motion of the ether" by studying the phase difference accumulated by beams traversing a loop in opposite directions. One can intuitively imagine that, given the constant speed of light in free space, two light beams traversing a circular path in opposite directions will complete the loop in the same amount of time if the setup is stationary (i.e., in an inertial reference frame). However, if the reference frame is not inertial but is instead rotating at an angular velocity ω, the beam propagating in the direction with opposite sense from ω will complete the loop faster than the other beam. A quick analysis and geometric argument reveals that the faster beam traverses the loop with a time difference $t_1 - t_2 = 8\pi R^2\omega/c^2$ and a phase difference $\Delta\varphi = 8\pi R^2\omega/c\lambda$. Technically, a fully convincing derivation of this result should require a complicated analysis of the propagation of electromagnetic waves in a rotating reference frame within the framework of general relativity, but surprisingly, the resulting expression for the phase shift is identical to this naively derived equation[110].

Georges Sagnac's interferometer was one of the first realizations of a "common path interferometer," which allows the two beams to traverse the exact same spatial path

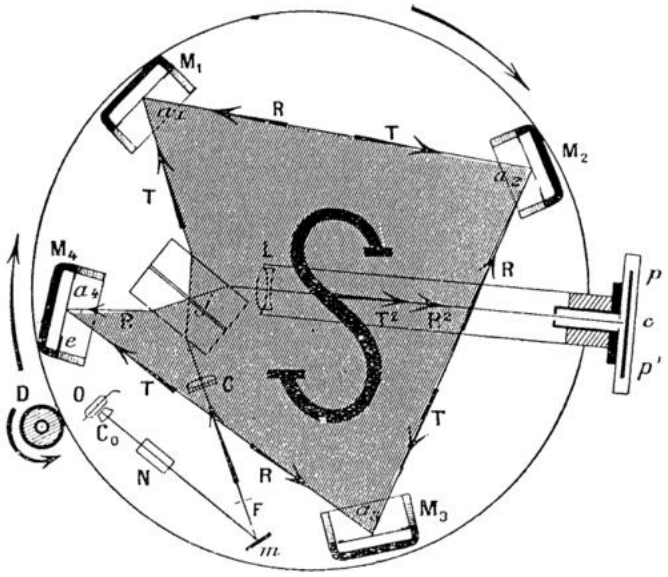

Figure 2.4. Schematic diagram of the original Sagnac interferometer form George Sagnac's 1914 publication. The two counter-propagating paths are labelled "R" and "T," and the area enclosed by the path (which is not actually circular) is shaded. [93]

in opposite directions. This scheme reduces or eliminates drift in the interferometer which would ordinarily occur due to the two beams interacting with slightly different local environments. In contrast, a Michelson-type interferometer is extremely sensitive to drift in the positions of mirrors or beam splitters because only one of the two optical paths is affected if a mirror is shifted, resulting in undesirable lack of stability. The stability of the Sagnac interferometer derives from the fact that both beams are continually overlapping at each point in space, so even time-dependent perturbations that are slow on the time scale of the round-trip-time for the beam to traverse the loop (e.g., temperature drift, mechanical vibrations, etc.) affect both beams equally and result in a net zero phase difference.

Importantly, because the two beams traverse the exact same spatial path in opposite directions, they may be thought of as time-reversed copies of one another. By symmetry, the only physical processes that can possibly result in a phase difference at the detector of the interferometer are those that explicitly break time-reversal symmetry, which is considered as an operator T which takes the variable representing time in the description of the physical system and exchanges it with its negative, $T: t \rightarrow -t$. Other physical observables that are sign-reversed under the T operator include velocity, momentum, magnetization, and electric current. Physical rotation of the Sagnac apparatus accomplishes this breaking of time-reversal symmetry in the sense that, in general relativity, the speed of light is actually *not constant in rotating reference frames*. The clockwise and counterclockwise rotating beams have different speeds in the rotating frame, which breaks the symmetry between the two beams and results in the observed phase shift. Likewise, any effect which breaks time reversal symmetry between the two

beams has the potential to result in an observable phase shift in a Sagnac-type interferometer.

Just like its historical predecessor, the magneto-optic Sagnac interferometer works on the principle of interference between two beams which have acquired a small phase difference due to the breaking of time-reversal symmetry within the sample. In this case, however, the time reversal symmetry breaking (TRSB) occurs because the Lorentz force $\vec{F} = e\vec{v} \times \vec{B}$ on a moving charge carrier is not time-reversal symmetric in a *local* sense, which means that the external field is assumed to be kept constant under the operator T. Under that assumption, we can see that the Lorentz force is reversed by the time reversal operator: $T(\vec{F}) = T(e\vec{v} \times \vec{B}) = e(-\vec{v}) \times \vec{B} = -\vec{F}$. In a truly complete treatment of the larger system, one may consider that Maxwell's laws do not actually break time reversal symmetry because the source of a magnetic field B is also a moving configuration of charges whose velocity is reversed under the T operator, so that the resulting Lorentz force is unchanged due to the sign change of both $\vec{v}$ and $\vec{B}$. However, it is a useful description in optics to consider the local magnetic field to be unchanged by the T operator so that nonreciprocal optical effects such as magnetic circular dichroism can be examined.

One concern about the correct operation of the magneto-optic Sagnac interferometer is the possibility that the instrument might detect other TRSB effects which would not be discernable from Kerr/Faraday rotation, for example the physical rotation of the apparatus (or the earth underneath it) like its historical predecessor. Luckily, the sensitivity to rotation of any Sagnac interferometer is proportional to the area enclosed by the "loop" formed by the beam paths. In the fiber-optic Sagnac

interferometer, the "loop" is formed by the fast and slow axes of a single polarization maintaining (PM) single-mode fiber, so that the area enclosed by the loop is exactly zero and the sensitivity to rotation vanishes.

2.2.2 Theory of Operation

The theory of operation[88,96] behind the magneto-optic Sagnac interferometer lies in detecting a phase shift between the LCP and RCP components of a single linearly polarized beam of light after it has interacted with a sample (either through reflection in the Kerr geometry or through transmission in the Faraday geometry). If the two beams are converted to a shared linear polarization and are incident on a detector, the phase-dependent interference intensity will be:

$$P(\varphi) = {}^{P_0}\!/_2\,(1 + \cos(\varphi)) \tag{2.2}$$

For a small DC phase shift φ, we can expand this expression about $\varphi = 0$:

$$P(\varphi) \approx P_0(1 - {}^{\varphi^2}\!/_2) \tag{2.3}$$

This expression is second-order in φ and therefore has very poor sensitivity so small φ. The breakthrough from the Kapitunlik lab was to realize that a time-dependent phase modulation somewhere in the Sagnac loop could be used to actively bias the instrument and to produce a voltage (from a lock-in amplifier) that is dependent on φ to first order, thereby making the interferometer sensitive to small φ. If we introduce a time-dependent sinusoidal phase modulation $\varphi_m(t) = \varphi_m \sin(\omega t)$, the time-dependent interference intensity becomes:

$$P(\varphi, t) = {}^{P_0}\!/_2\,(1 + \cos(\varphi + \varphi_m \sin(\omega t))) \tag{2.4}$$

Performing a Fourier expansion on this expression about ω, we have:

$$P(t) = P_0[\frac{1}{2} + \frac{J_0(2\varphi_m)}{2} + \sin(\varphi)\, J_1(2\varphi_m)\sin(\omega t) + \cos(\varphi)\, J_2(2\varphi_m)\cos(2\omega t) + \dots] \quad (2.5)$$

Note that the quantity of interest, φ, occurs in the both the first and second harmonic terms over ω. Furthermore, a lock-in amplifier monitoring this time-dependent voltage output from the photodiode that is locked to frequency ω will yield a DC voltage:

$$V_\omega = G\ R\ P_0 \sin(\varphi)\, J_1(2\varphi_m) \quad (2.6)$$

and a lock-in amplifier locked to frequency 2ω will yield a DC voltage:

$$V_{2\omega} = G\ R\ P_0 \cos(\varphi)\, J_2(2\varphi_m) \quad (2.7)$$

where G is the transimpedance gain of the amplifier circuit, R is the responsivity of the photodetector, and P_0 is the power at the detector when $\varphi = \varphi_m = 0$. In principle, these quantities could be measured fairly accurately so that the phase shift φ could be extracted from either V_ω or $V_{2\omega}$ alone, but the stability and accuracy of such a method would be questionable. Instead, we may simultaneously monitor V_ω and $V_{2\omega}$ and take the ratio of the two:

$$\frac{V_\omega}{V_{2\omega}} = \frac{J_1(2\varphi_m)}{J_2(2\varphi_m)} \tan(\varphi) \rightarrow \theta = \frac{1}{2}\varphi = \frac{1}{2}\tan^{-1}\left(\frac{J_2(2\varphi_m)}{J_1(2\varphi_m)}\frac{V_\omega}{V_{2\omega}}\right) \quad (2.8)$$

The modulation depth φ_m is decided by maximizing the ratio $\frac{J_2(2\varphi_m)}{J_1(2\varphi_m)}$ which will maximize our sensitivity to φ. This ratio is maximized for $\varphi_m \approx 0.92$. Almost miraculously, the factors G, R, and P_0 cancel out – they turn out to be unnecessary for extracting φ and do not affect the measurement of φ in this phase-modulated interferometric scheme. This is the principle advantage of using the interferometric approach over other experimental schemes – nearly all time-independent sources of phase

shifts that do not break time-reversal symmetry (e.g., linear birefringence or nonmagnetic circular birefringence in the optical path) are eliminated by use of the common-path interferometer design, and time-dependent fluctuations (e.g., in the laser power output, temperature drift, etc.) are eliminated by actively biasing the interferometer by a time-dependent phase modulation and using the dual lock-in detection scheme. The schamtic diagram for this interferometer, along with an illustration of the time-varying voltage detected by the lock-in amplifier, is shown in Figure 2.5.

We will now examine the design of the interferometer and the realization of this time-dependent phase modulation. As illustrated in Figure 2.5, a coherent broadband light source centered at 1500nm is emitted by a superluminescent light-emitting diode (SLED) and coupled into a single mode (SM), nonpolarization-maintaining fiber. That fiber is first coupled into an inline fiber isolator to prevent backscattered light from re-entering the light source and causing intensity instability. It then enters an inline polarization controller, and then into port 1 of a polarization-maintaining (PM) SM fiber circulator. The polarization controller is adjusted so that the light exiting the controller is entirely coupled into the fast axis (FA) of the circulator. Light exiting port 2 of the circulator is sent through an inline FA-aligned linear polarizer, and then into an inline phase modulator. The phase modulator is composed of a Lithium Niobate ($LiNbO_3$) crystal sandwiched in a parallel-plate capacitor. Due to the lack of inversion symmetry in the $LiNdO_3$ crystal, the electric field supplied by the capacitor induces a birefringence and modifies the refractive index for polarizations oriented along the field direction. The schematic diagram of the Sagnac interferometer is shown below in Figure 2.5. The birefringence in the crystal, defined as $\Delta n = n_{||} - n_{\perp}$ introduces a phase shift

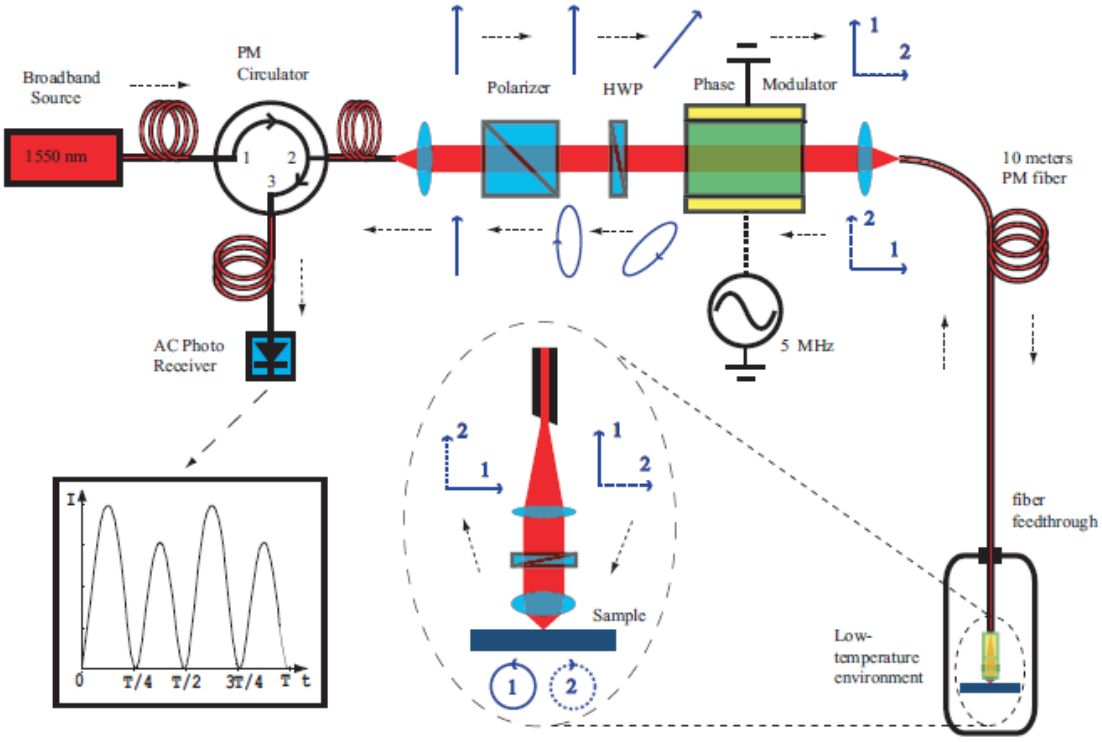

Figure 2.5. Sagnac Interferometer diagram. The light source originates in the upper left at the SLED. It enters port of the circulator and exits port two, where the polarizer/EOM/sample are located. It then returns (after a 90° rotation from the QWP before the sample) into port two before being routed to port 3 at the detector. Inset: time-dependent interference intensity at the lock-in amplifier and/or oscilloscope.[88,96]

$\Delta\varphi_1 = 2\pi\,\Delta n\,L\,/\,\lambda$ between light polarized along the field direction relative to light polarized orthogonal to the field direction. The phase modulator is physically rotated 45° relative to the fast axis of the input fiber so the two beams with phase difference $\Delta\varphi_1$ have approximately equal power. From this point on, the light can be thought of as two non-interacting, completely incoherent beams that propagate in two orthogonal modes of a single PM fiber. The two beams are then launched into the fast and slow axes of a 10m long SM PM fiber that runs to the sample. At the other end of the 10m long fiber, the beam leaves the fiber and is collimated into a 0.5mm diameter free space beam which travels through a quarter wave plate (QWP) whose fast axis is rotated 45° relative to the fast axis of the fiber.

The purpose of this QWP is twofold: first, the eigenmodes of electromagnetic radiation in the sample with magnetic circular birefringence are circular polarizations (denoted LCP and RCP). The two beams should be circularly polarized with opposite handedness (one LCP and one RCP) when they interact with the sample so that the phase difference φ can be accumulated. When they leave the fiber, however, they are each linearly polarized along the axes defined by the fast/slow axes of the fiber. Properly aligned, the QWP converts the two linear polarizations to two circular polarized beams with opposite handedness.

The beams are then allowed to interact with the sample, either by a direct reflection from the sample or by transmission through a sample and reflection from a nonmagnetic mirror behind the sample. If the beams reflect once from a sample, the observable phase difference is simply twice the Kerr rotation angle $\varphi = 2\theta_K$. If the beam transmits through the sample twice, it accumulates twice the Faraday rotation angle that it

would through a single pass and the phase difference is therefore $\varphi = 4\theta_F$.

The beams then pass through the QWP a second time, which converts them both back to a linear polarization, but *with a polarization state 90° rotated from before.* The beam that travelled to the sample on the fast axis (FA) of the 10m long fiber therefore returns on the slow axis (SA), while the beam that travelled to the sample on the SA returns on the FA. Now it is clear why this qualifies as a Sagnac-type interferometer; because each beam travels one leg on the FA and one leg on the SA of the fiber, the only phase difference that they will have accumulated on the trip will be due to time reversal symmetry breaking by magnetic circular birefringence in the sample!

The beams again reach the $LiNbO_3$ phase modulator, and receive a phase shift $\Delta\varphi_2$ which will in general be different from the first phase shift $\Delta\varphi_1$ because a time-varying voltage is delivered to the phase modulator and the speed-of-light delay from the first pass through the phase modulator is $\tau \approx 100ns$ (given two passes through a 10m fiber with refractive index ~1.3). The total phase delay is:

$$\Delta\varphi_1 + \Delta\varphi_2 = 2\pi\, \Delta n_1\, L\, /\, \lambda - 2\pi\, \Delta n_2\, L\, /\, \lambda \tag{2.9}$$

Note the minus sign of the second phase shift, due to the fact that the orientations of the two beams have been rotated 90° from their first pass through the crystal. Note that since both beams have now traversed the same spatial path (in opposite directions) they are again coherent with one another. The beams are then sent through the linear polarizer again, retaining only the FA component of their net polarization, before entering port 2 of the circulator and leaving port 3. They are directed into an AC photodetector, where the time-dependent interference pattern is measured and sent to a lock-in amplifier.

Now we know that the phase modulation should have the form $\varphi(t) =$

$\varphi_m \sin(\omega t)$, but the beams make not one, but two separate passes through the phase modulator for a net phase delay of $\Delta\varphi_1 + \Delta\varphi_2 = \frac{2\pi L}{\lambda}\ (\Delta n_1 - \Delta n_2)$. We can achieve this goal by employing a sinusoidal phase modulation pattern $\Delta n_1 \propto \sin(\omega t)$ and choosing the phase modulation frequency correctly so that $\omega = \pi/\tau$, where τ is the speed of light delay time between the two passes through the phase modulator. The optimal modulation depth is selected by choosing an appropriate electric field so that $|\Delta n_1| = |\Delta n_2| = \lambda\ \varphi_m\ /\ 4\ \pi\ L$. Then the phase modulation pattern is

$$\varphi(t) = \Delta\varphi_1(t) + \Delta\varphi_2(t) = \frac{2\pi L}{\lambda}\ \big(\Delta n_1(t) - \Delta n_2(t)\big) =$$

$$\frac{2\pi L}{\lambda}\ \left(\frac{\lambda\,\varphi_m}{4\pi L}\sin(\omega t) - \frac{\lambda\,\varphi_m}{4\pi L}\sin\big(\omega(t+\tau)\big)\right) = \frac{\varphi_m}{2}(\sin(\omega t) - \sin(\omega t + \omega\tau)) =$$

$$\frac{\varphi_m}{2}(\sin(\omega t) - \sin(\omega t + \pi)) = \varphi_m \sin(\omega t) \qquad (2.10)$$

exactly as desired. The correct operating frequency for the Sagnac interferometer turns out to be between 4.72MHz and 4.88MHz, depending on the experiment and optical path length, which changes by up to 20cm for different experimental geometries.

2.2.3 Components and Construction

The mathematical derivation in which we show that a time-dependent phase modulation allows us to extract the DC LCP-RCP phase shift φ with high sensitivity seems straightforward, but there are many sources of experimental error that can complicate the real experiment. The optical components must be selected carefully so that these sources of error are minimized, and they must also be assembled with care for the system to work. Here, we will briefly discuss the largest potential sources of error in the Sagnac interferometer, and the resolutions to these issues that were incorporated into

the design.

First, we must use a coherent light source in order for the interferometric scheme to work at all, but the temporal coherence length should not be so long that undesired (but unavoidable) reflections from fiber interfaces, optical components, etc., will contribute to the interference pattern at the detector. The temporal coherence length can be thought of as the distance over which there exists some phase correlation between difference parts of the beam from a light source. It can also be thought of as the minimum distance that multiple internal reflections in the Sagnac interferometer need to travel before they reach the detector to ensure that they are completely incoherent at the detector and do not contribute unwanted coherent interference. The coherence length L_c should be significantly longer than the equivalent path length difference introduced by our time-dependent phase modulation $\varphi(t)$, so that the modulation does not cause the two polarizations to become incoherent ($L_c \gg \lambda\varphi_m/2\pi \approx 100nm$). However L_c should be significantly shorter than the physical size of the smallest optical component in the apparatus ($L_c \ll 1mm$) so that multiple reflection do not interfere coherently at the detector. The coherence length is related to the central wavelength λ_c and the spectrum width $\Delta\lambda$ (or the bandwidth Δf) by:

$$L_c = {}^{c}/_{\pi\,\Delta f} \approx {}^{\lambda^2}/_{\Delta\lambda} \tag{2.11}$$

A superluminescent light-emitting diode (SLED) with a center wavelength $\lambda_c = 1550nm$ and a width $\Delta\lambda \approx 75nm$ (purchased from Denselight semiconductors, model DL-CS5077A, Figure 2.6) has a temporal coherence length $L_c \approx 10\mu m$ which falls perfectly within the necessary range. The SLED module is operated with a temperature controlled, stable current power supply (Newport ILX Lightwave LDC 3724C) with

operating temperature fixed at 25°C and driving current between 60mA and 200mA (depending on the scattering/absorption of the sample).

In fact, this was one of the primary motivations for building the instrument to operate at 1550nm. This wavelength is used extensively in the telecommunications industry, making it easy and relatively inexpensive to find high quality and well specified components like the SLED light source. In addition, to the light source, the single-mode polarization maintaining fibers, connectors, polarization controllers, phase modulators, detectors, etc. are all easier to find and purchase at 1550nm than any other wavelength.

The fiber connections are all Ferrule Connected / Angled Physical Contact (FC/APC) couplings in an attempt to reduce backscattering into the light source. APC fiber couplings have significantly lower backscattering amplitudes (nominally less than -65dB back reflection per interface, Figure 2.7) compared to other connector types. In addition to the fiber isolator being the closest component to the light source, the problem of power instability due to backscattering light back into the light source does not appear to be an issue, and the backscattered incoherent light reaching the detector is not noticeable. In addition every fiber interface was inspected with a fiber scope and cleaned until satisfactory coupling (~-3dB insertion loss or ~94% transmission) was achieved.

The inline polarization controller was purchased from Thorlabs (Polarite PLC-900) and a separate 8cm non-jacketed SM non-PM was purchased to use with the fiber controller. The polarization controller has two adjustments that apply either a vertical stress (resulting in a linear birefringence) or a torsional stress (resulting in a circular birefringence) to the fiber inside it. By connecting the output of the polarization controller to the inline linear (fast axis) polarizer and maximizing the transmission

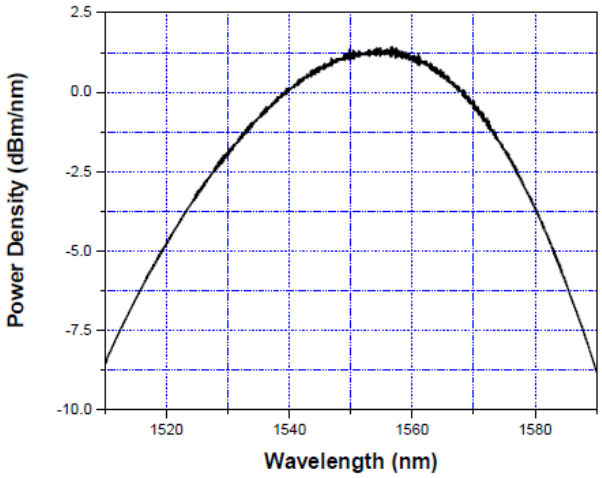

Figure 2.6. Emission spectrum of the 1500nm SLED light source from Denselight semiconductors.

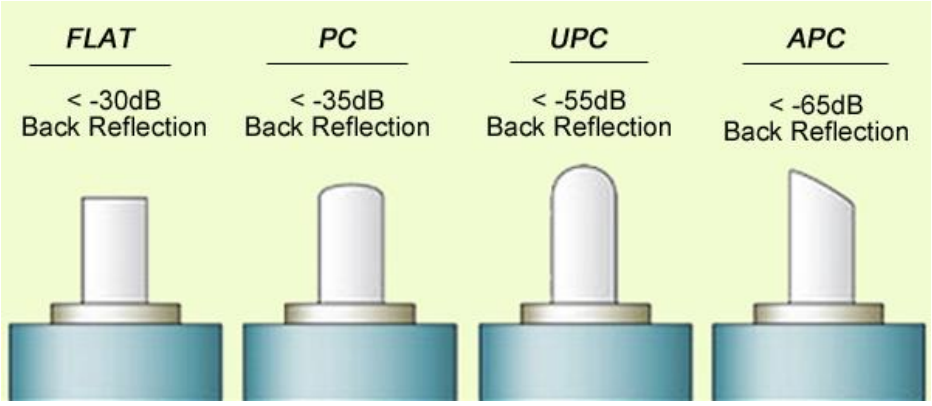

Figure 2.7. Fiber coupling types and their nominal back reflection amplitudes. APC type connectors were chosen for the Sagnac interferometer because the back reflection is minimized.

through the LP, the polarization can be very accurately set to launch into the fast axis of the circulator. The circulator itself was purchased from Thorlabs (model # CIR1550PM-APC) and has an (unfortunately high) insertion loss of $0.9dB$, a directivity of $> 50dB$, and an isolation of $> 40dB$. The PM fibers are all panda-type single mode. The detector is a New Focus model 1811 InGaAs IR photoreceiver, which has a bandwidth of 125MHz and is directly coupled to a FC fiber input. The lock-in amplifier is a Zurich model HF2LI and is capable of measuring up to 50MHz.

2.2.4 Magnet and Cryostat Integration

Performing measurements over a wide range of temperatures is of vital importance in condensed-matter physics. Low temperature measurements are of particular importance in spintronics, where the magnetic and electronic properties of materials and devices are drastically different at very low temperatures compared to room temperature. For temperature control, a Sumitomo Heavy Industries closed-cycle helium compressor/cold head with a minimum temperature of 6K was outfitted with fused silica windows so that optical measurements could be performed with the Sagnac instrument at room temperature, mounted on the optical bench in front of the cryostat. The cryostat first came outfitted with birefringent quartz windows and the Sagnac is ideally immune to linear birefringence, but the nonbirefringent fused silica windows were machined into the shield of the cryostat just in case. A GMW 5501 electromagnet with a maximum field strength of 0.25 Tesla fit around the cryostat to provide a bidirectional magnetic field.

This combination of temperature and bidirectional magnetic field control allows us to perform magnetic characterization of thin films and devices at low temperature.

This scheme was used, for example, to trace the temperature-dependent magnetic hysteresis of a Lanthanum Strontium Manganite (LSMO) thin film, which is a ferromagnetic half-metal with a Curie Temperature of $T_c \approx 320K$ that is particularly useful to the field of spintronics for its high efficiency of electrical spin injection (Figure 2.8).

By having the sample (inside the cryostat), the magnet, and the Sagnac disconnected and free to be moved with respect to one another, there are six possible geometries for a B-field dependent measurement. Those six geometries, illustrated in Figure 2.9, depend on whether the bulk or surface magnetization is to be probed, in which case the measurement should be performed in transmission (Faraday) or reflection (Kerr) geometry, respectively. The magnetic field can be parallel with the laser, perpendicular to the laser, or somewhere in the middle (dubbed the "oblique" geometry). The distinction between these geometries will become significant in Chapter 3 when we discuss the spin Seebeck effect, but for now it should suffice to say that all three are easily accessible with our instrument. The LSMO experiment shown in Figure 2.8 was performed in the transparent (Faraday) oblique geometry.

2.2.5 Alignment and Calibration

Because the alignment of the fast/slow axes of the FC/APC fiber connections are not adjustable (the alignment is already done by matching the keys on the connector ferrules), the only other technically challenging step is to ensure that the QWP fast axis is precisely aligned at 45° relative to the axes of the sample end of the 10m PM fiber, and to ensure that the modulation frequency is exactly $\omega=\pi/\tau$. These steps need to be done only

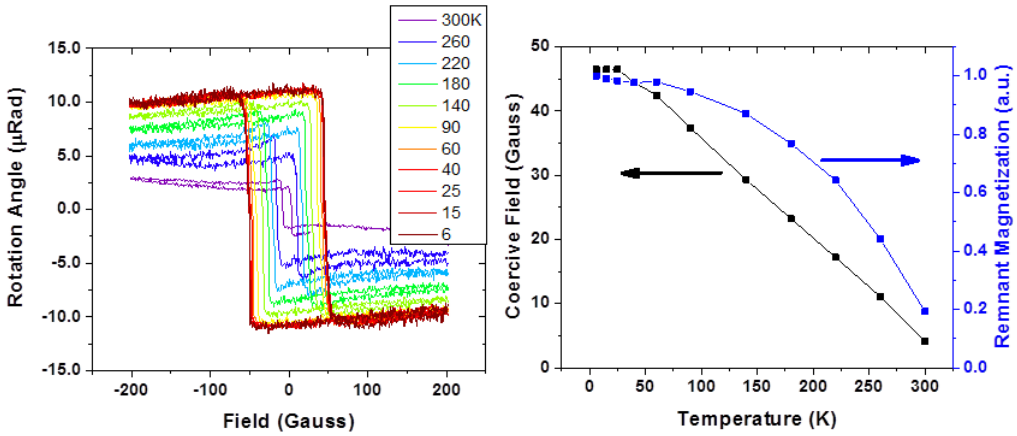

Figure 2.8. Temperature dependence of the magnetic hysteresis of 10nm LSMO on STO from 6K to 300K, and normalized remnant magnetization and coercive field versus temperature.

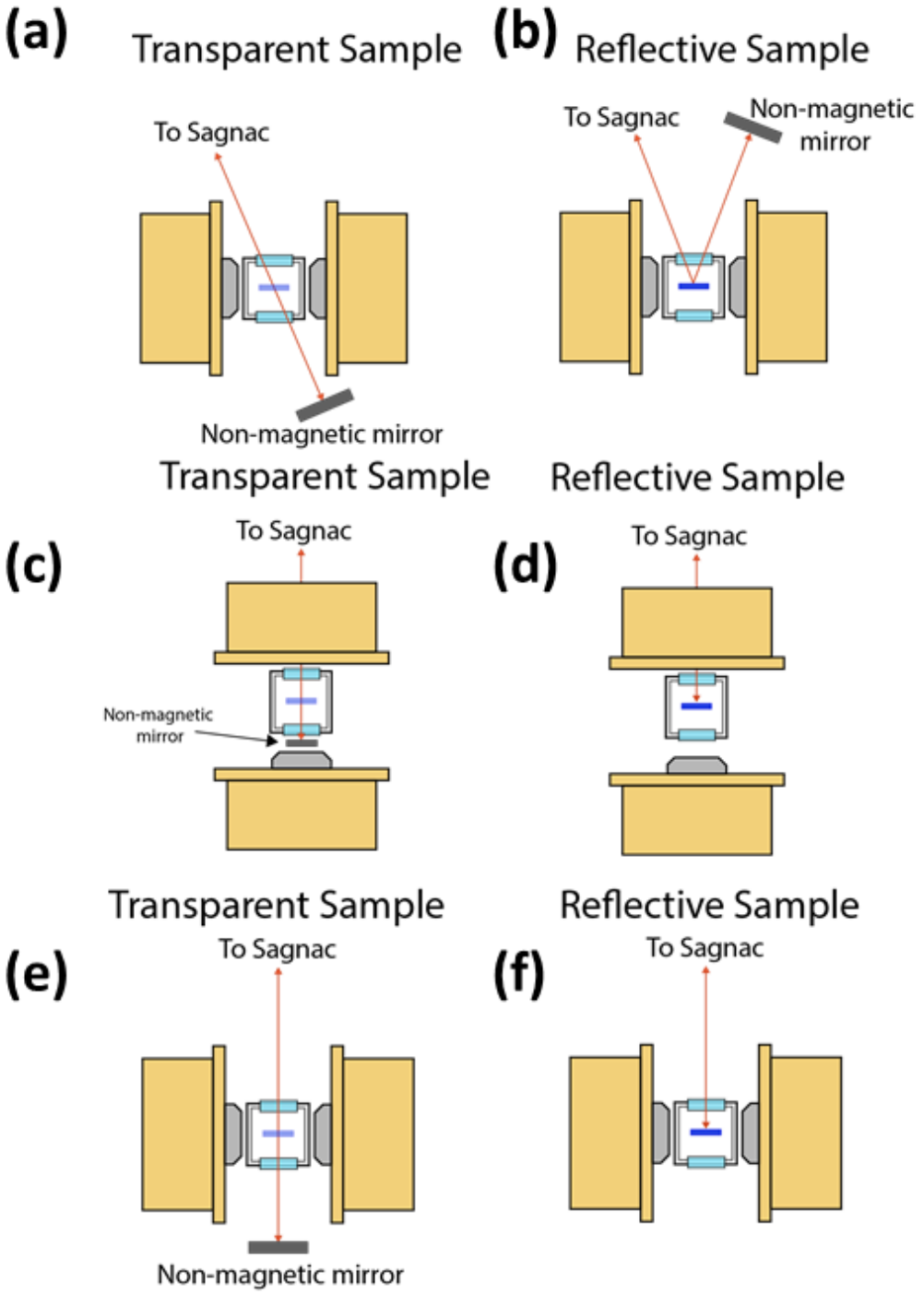

Figure 2.9. Six distinct geometries for B-dependent Sagnac measurements. (a) Oblique field, transmission mode. (b) Oblique field, reflective mode. (c) Parallel field, transmission mode+. (d) Parallel field, refection mode. (e) Perpendicular field, transmission mode (f) Perpendicular field, reflection mode.

once in principle, since the QWP holder and path length may not need to be changed (this was the case in the Kapitulnik lab). However, our Sagnac interferometer faced a unique challenge: over the course of the four years that the interferometer was used in the Vardeny group, it needed to be moved between at least four different labs, sometimes being transferred between labs more than twice per week. In order to avoid completely disassembling and reassembling the entire interferometer each time it was moved, the setup was built on a mobile cart with wheels to while we had glued a small (1×2 feet) optical breadboard. The breadboard served both as a useful surface to bolt down optical components and keep the fibers from moving, and as a metal grounding plane for the detector, phase modulator, and other electronics. The other electronics (lock-in amplifier, computer, laser controller, translation stage controller, power filter, detector power supply) were kept on a 19" electrical rack which also rolled from lab to lab. This moving setup was affectionately known in the lab as the "taco cart."

The complication introduced by this frequent moving of labs is that the path length from the end of the 10m fiber to the sample (or nonmagnetic mirror) would change by several tens of centimeters with each new experiment. Of course, the speed of light delay time τ depends on the Sagnac path length, and the "proper" resonant frequency $\omega = \pi/\tau$ will also change. When operating the Sagnac interferometer in "microscope mode," we have two homebuilt stages (for either short or long working distances) that require the QWP to be re-aligned as well. For this purpose, there are two methods for correctly aligning the QWP and finding the correct modulation frequency, and in the interest of making the lives of future graduate students easier, I will detail both here.

The more accurate (but more difficult) method was realized by Spielman and

involves looking at the spurious signal created by heating up the EOM crystal while the Sagnac is pointed at a nonmagnetic mirror in zero magnetic field (i.e., the real Kerr/Faraday rotation signal is actually zero). Heating the EOM, especially when the phase modulation frequency is not correct, will result in accidental amplitude modulation and a spurious signal at the lock-in amplifier (90° out of phase from the true Kerr signal). This spurious signal will be minimized when the modulation frequency is correct. This method was found to be less effective when using an inline phase modulator rather than a free space modulator, however, due to the smaller amount of free space outside the fiber in the inline configuration, so the second method was usually favored.

The second method requires that the phase modulation voltage source is turned off and the DC output of the Newport 1811 photoreceiver is connected to a voltmeter. The QWP will be correctly aligned relative to the fast/slow axes of the PM fiber, and then the correct phase modulation frequency will then be extracted. With no source of Kerr/Faraday rotation in the beam path (just a nonmagnetic mirror), the interference should be purely constructive when the QWP is correctly aligned and the linear polarizer on port 2 of the circulator should not reduce the intensity at all. While monitoring the voltage from the photodetector, rotate the QWP until the intensity at the detector is maximized. Once the correct QWP angle is found, fix it in place and turn on the phase modulation voltage source. The correct frequency (which is around 4.8MHz for this system) will be found when the first harmonic voltage at the lock-in amplifier is zero and the second harmonic voltage is maximized. The correct modulation depth is found by introducing a large source of Faraday rotation (a GaAs wafer or a Bismuth-doped YIG crystal work excellently) into the beam path and changing the voltage until the first

harmonic is maximized.

The performance of the Sagnac interferometer can be evaluated by three metrics: accuracy, stability, and noise. In that order, each of these has been evaluated to ensure that the Sagnac is working as designed before attempting any real measurements.

According to the design, the magneto-optic Sagnac interferometer should be able to measure Kerr/Faraday rotation angles between 10nRad (limited on the low end by drift in the instrument) to roughly 0.1Rad, where it is limited by "saturation" where the mathematical validity of keeping only the first two terms of the Fourier expansion of the time-dependent interference pattern is no longer valid for large phase shifts. Accuracy measurements should be taken over a wide range in order to verify the validity of the Sagnac measurements of these remarkable seven orders of magnitude. For this purpose, we have measured the Verdet constants (at 1550nm) of several easily accessible materials, which is defined for paramagnetic or diamagnetic materials as the Faraday rotation angle per unit length per magnetic field:

$$\theta_F = V\ B\ L \cos(\vartheta) \tag{2.12}$$

where ϑ is the angle between the light wavevector and the magnetic field direction. For small phase shifts, the Verdet constant of a 0.3mm glass microscope cover slip was measured in fields up to 200 Gauss (maximum Faraday rotation angle of 780nRad) and was found to be $0.37 \pm .03\ Rad/Tm$, which is in excellent agreement with published values of $0.35\ Rad/Tm$. For medium phase shifts, a 0.5mm thick undoped GaAs wafer was measured in fields up to 2kG (maximum Faraday rotation angle of 113mRad) and the Verdet constant was calculated as $33 \pm 1.5\ Rad/Tm$, also in good agreement with the literature value of $35\ Rad/Tm$. A bismuth-doped yttrium iron garnet (BIG) crystal was

purchased from Integrated Photonics with a nominal Faraday rotation angle of 8 degrees (0.14 Rad), which was found to be too large to be measured accurately by the Sagnac but was very useful for correctly phasing the lock-in amplifier.

The stability of the instrument was quantified by measuring the Kerr rotation from a nonmagnetic mirror in magnetic field $B = 0$ for a period of more than 24 h. The data from that experiment is shown below in Figure 2.10, and the maximum long-term drift in the instrument is estimated to be $\pm$20nRad. The drift in the instrument is apparently a periodic behavior with a period of roughly 24 h, which is likely due to thermal expansion/contraction of the fibers and optical components as the temperature in the lab changes from day to night. It is likely possible to reduce this drift further by placing the Sagnac instrument in a temperature-controlled box, but this was deemed unnecessary for two reasons. First, since the smallest significant Kerr signal claimed in any of our publications is >100nRad, a lower bound on drift-induced artefacts of 20nRad is sufficient for our purposes. Second, since consecutive measurements (for example, for the spin Seebeck project) took place over a span of several hours during the daytime (hours one through eight in Figure 2.10), the drift between those experiments is likely less than 5nRad.

The noise levels in the Sagnac interferometer were measured by the same methods introduced by Jing Xia in his excellent PhD dissertation (Stanford University, 2008). The goal of this project is to approach the ultimate noise floor for any optical instrument which is the shot-noise barrier, which can be written as:

$$V_{RMS} = \sqrt{2\, e\, I\, \Delta f} \tag{2.13}$$

where V_{RMS} is the root-mean-square voltage fluctuation, e is the fundamental charge unit,

I is the detector photocurrent, and Δf is the frequency bandwidth of the measuring device. Jing Xia shows that this is equivalent to a Kerr angle shot-noise of:

$$\theta_{Shot\ Noise} = \frac{0.3}{\sqrt{P_{avg}}}(\mu Rad/\sqrt{Hz}) \tag{2.14}$$

where P_{ave} is the time-averaged optical power at the detector in μW. At an average optical power of $10\mu W$ (which is the typical power used during all experiments), the shot-noise Kerr angle noise is $\sim 100\ nRad/\sqrt{Hz}$. Our measured noise levels, taken by measuring a nonmagnetic mirror in zero field with a $1\ Hz$ filter bandwidth at the lock-in amplifier, was typically $190\ nRad/\sqrt{Hz}$. Therefore we can achieve about a factor of two above the theoretical noise floor, which was deemed sufficient for our measurements. The noise floor could be reduced by increasing the average optical power, but the increased laser power will result in undesirable heating of our temperature-sensitive samples, so most measurements in the lab using a detector power of $\sim 10 - 20\ \mu W$ have a noise level of $\sim 150 - 200\ nRad/\sqrt{Hz}$ (Figure 2.11).

2.2.6 Microscope Extension

When the Sagnac interferometer was initially being constructed, the goal was to investigate electrical spin injection into organic semiconductor in spintronic devices. For this purpose, the collimated beam that emerges from the 10m fiber with a width of ~0.5mm did not have sufficient resolution to image such devices with lateral dimensions of ~100μm. It was decided that the best solution to achieve diffraction-limited spatial resolution of ~1μm would be to mount the end of the 10m fiber, along with the QWP and focusing optics, on a scanning 2D stage while keeping the sample stationary in the focal plane of the focusing optics. The reason for the decision to move the end of the

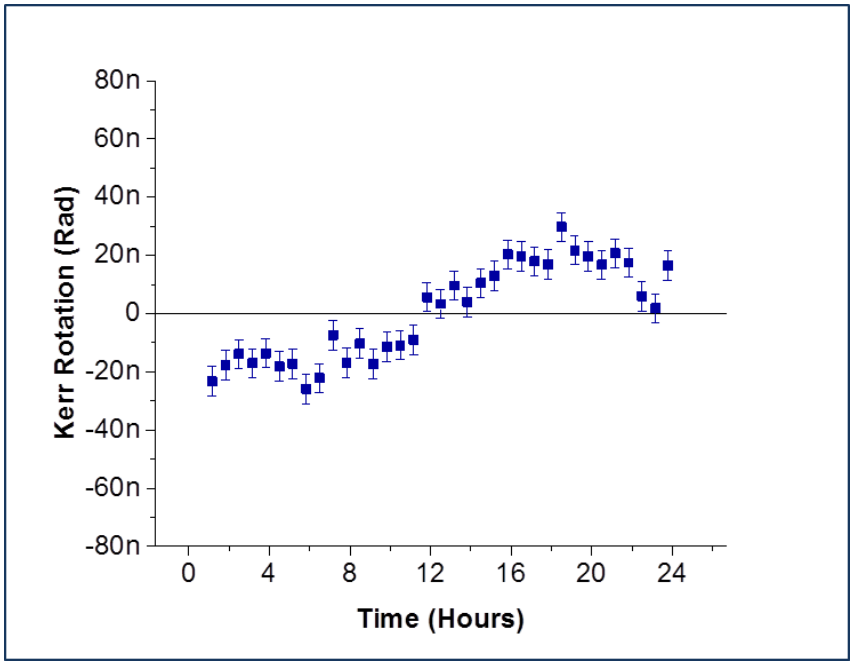

Figure 2.10. Drift in the Sagnac interferometer measured at zero field using a nonmagnetic mirror over a 24 hour period.

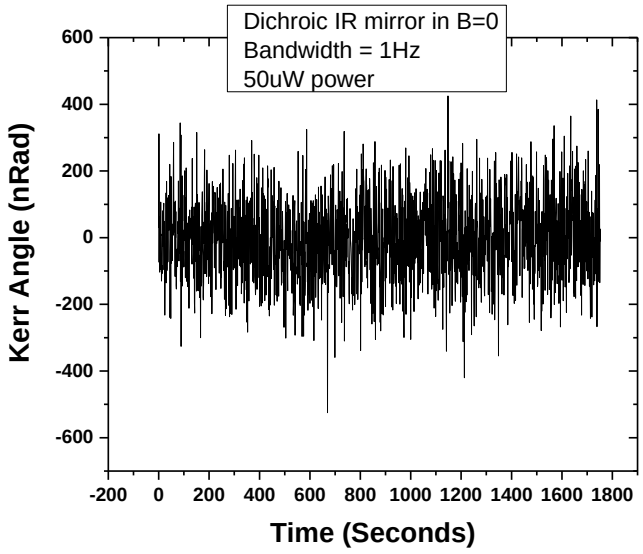

Figure 2.11. Raw data from a 30-min test with a lock-in bandwidth of 1Hz and 50μW optical power at the detector, yielding a Kerr noise of 120 $nRad/\sqrt{Hz}$.

interferometer, rather than the sample itself, was twofold. First, as mentioned earlier in Section 2.2.3, the Sagnac interferometer was regularly moved between about 4 different labs in the physics department. If we were to invest in hardware to physically move the samples, rather than the Sagnac fiber, within the (nonmobile) cryostats, we would have to build four separate setups for each lab.

Instead, if the microscope scanning hardware is permanently attached to the mobile Sagnac, then the same 2D stage can be used equally well anywhere that the Sagnac moves. For this, we purchased two Newport MFA-PPD motorized linear stages and a ESP301-3G motor controller to drive them. The minimum step size for these stages is 100nm with a minimum unidirectional repeatability of 120nm. A 90° bracket and a modified Thorlabs FB-51 fiber bench were machined in our shop to attach the two linear stages together at 90°(for 2D scanning ability) and to mount the fiber collimating lens, QWP, and commercial confocal objective lens (between 10x and 40x magnification) to the stage. Alternately, for microscopy with longer (up to 2 in.) working distances, a Thorlabs GBE20 beam expander as an aspheric lens with a 2" focal length were attached to the scanning stage to allow the beam to be focused onto a sample inside of an optical cryostat (sample at T=4K). This setup is shown in Figure 2.12.

This scheme, in particular using the 40x microscope objective, is sufficient to achieve $< 1\mu m$ spot size, which is estimated by scanning over a "sharp" feature (the edge of a gold film on silicon in Figure 2.13) and fitting the rise in the second harmonic voltage at the lock-in amplifier with an error function. The space in the middle of the stage where the beam is collimated ensures that it passes through the QWP at normal incidence; if it does not, the phase delay caused by the QWP will not be exactly$\lambda/4$.

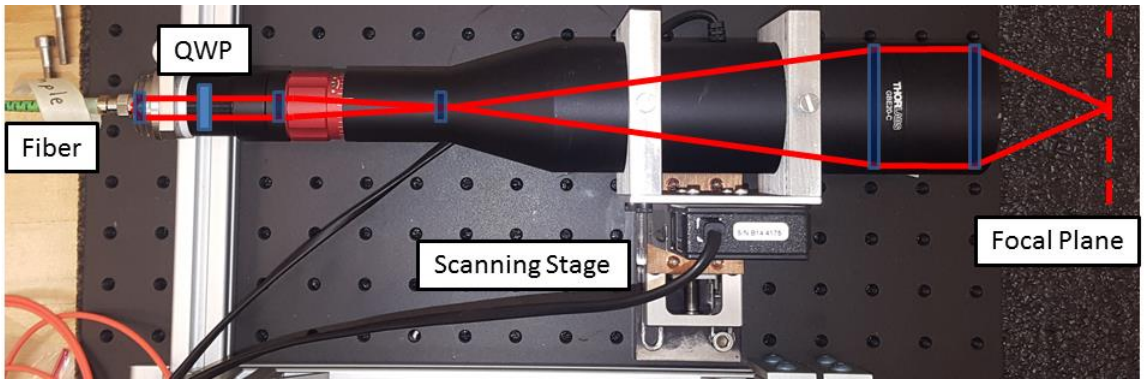

Figure 2.12. Picture of the "long-working distance" homebuilt Sagnac microscope. The Galilean beam expander has a 20x magnification and collimates the beam on its output to roughly 1.5". An aspheric lens is placed at the exit of the beam expander, which is then faced against a cryostat window. When not working on samples at cryogenic temperatures, a simple 10x-40x commercial microscope objective lens was used instead of the beam expander.

A typical Kerr-microscope image is shown below in Figure 2.14. This is an image of two 50nm thick $Ni_{20}Fe_{80}$ strips of dimensions 0.5mm by 5mm on a silicon nitride (SiN) substrate that was used to optically measure the spin Seebeck effect. The films are magnetized out-of-plane toward their hard axis, which requires a field normal to the substrate of 1.5kG. Note that the BK7 glass lens of the microscope objective was inside of the 1.5kG magnetic field due to the short ~1mm working distance. The lens in the objective lends an unavoidable Faraday rotation angle of approximately $200\mu Rad$ as a "background" to the whole image in addition to the Kerr rotation obtained in the reflection from the NiFe or SiN surface, which was manually subtracted before any data analysis was performed.

2.3 Magnetic Field Effect Spectroscopy

The magnetic field effect (MFE) spectroscopies discussed in the introduction are relatively simple to carry out experimentally (compared to high-precision polarimetry using the Sagnac interferometer). However, the MFE experiments took place in four different magnets/cryostat systems depending on the magnetic field range of interest, each with individual engineering concerns and constraints, so a summary will be given in this Chapter. I will also briefly summarize the spectrometers, experimental geometries, excitation lasers, and sample fabrication methods that were used.

In general, when performing spectroscopy in magnetic fields, we must consider the possibility that the result of the experiment depends on the angle between the magnetic field direction and the direction from which the photoluminescence (PL) is collected. There are two possible geometries (shown in Figure 2.15), which are B || k and

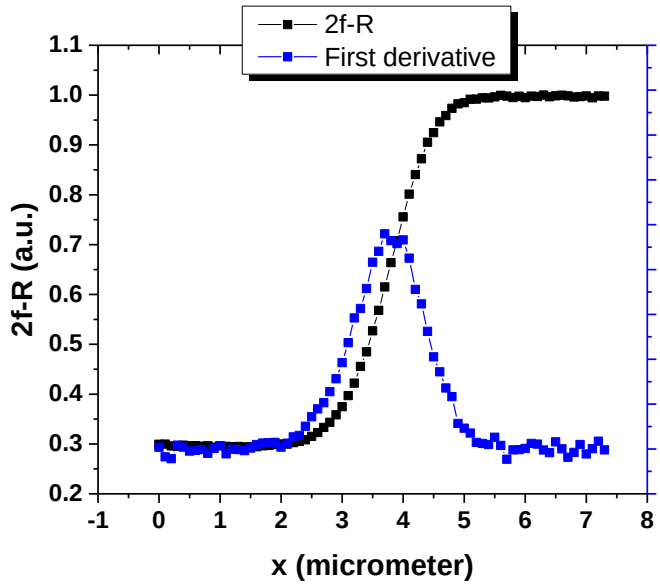

Figure 2.13. Measurement of the spot size of the Sagnac interferometer using a 40x objective, scanning from SiO_2 to Au. Spot size (full width at half max) is less than 2 μm.

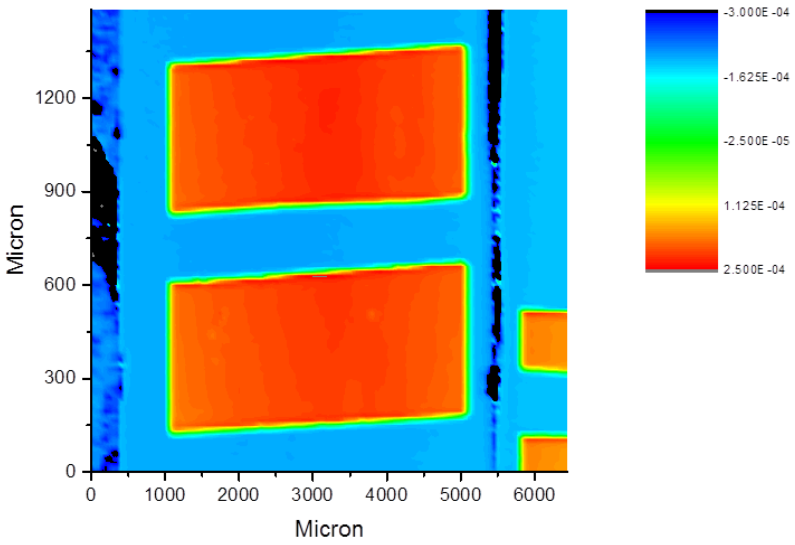

Figure 2.14. Example Kerr image of two $Ni_{20}Fe_{80}$ strips on a silicon nitride substrate.

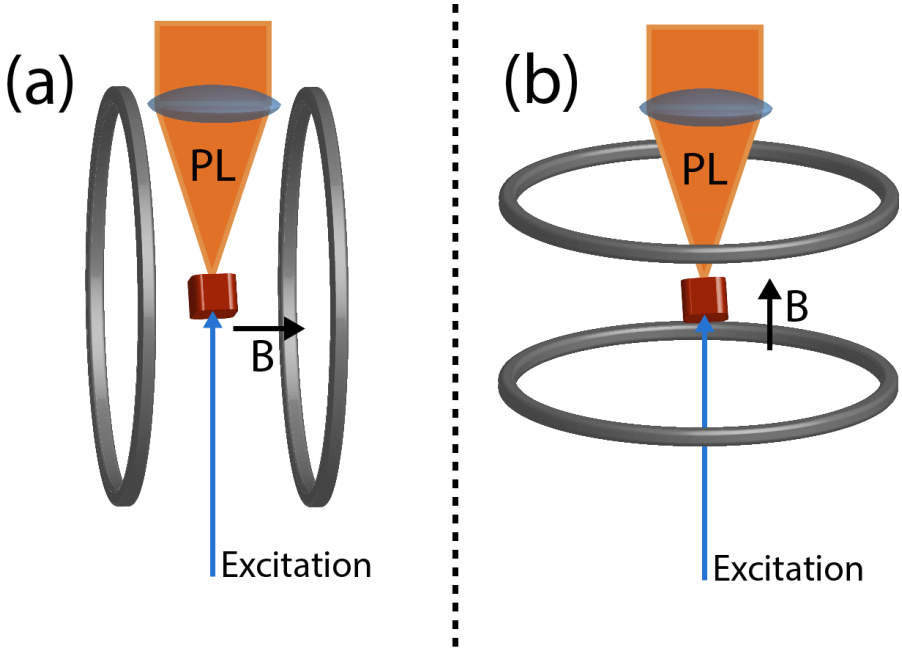

Figure 2.15. (a) MFE spectroscopy in the Voigt configuration with $B \perp k$. (b) MFE spectroscopy in the Faraday configuration with $B \parallel k$.

$B \perp$ k, where k is the wavevector of the collected PL; these are dubbed the "Faraday" and "Voigt" configurations, respectively.

In Chapters 4 and 5, we will see that the angle between B and k is important when the measured quantity is vector-like (e.g., PL polarization in FICPO measurements), but not when the measured quantity is scalar-like (e.g., probabilities or time scales appearing in rate equations). This distinction only needs to be mentioned now in order to specify which configurations are accessible in each magnet system.

For relatively small magnetic fields, a GMW 5501 electromagnetic with a maximum field strength of 0.25 Tesla was placed outside of a closed-cycle helium compressor / cold head from Sumitomo Heavy Industries with a minimum temperature of 6K. The magnet/cryostat was placed on an optical bench. The light source was either a laser diode mounted in a Thorlabs TCLDM9 temperature controlled, stable-current diode controller or a 486nm solid state laser. The linearly polarized above –gap laser excitation was directed onto the sample from the back, and the photoluminescence was collected by a large (2" diameter) lens and focused into a nonmagnetic broadband visible range optical fiber. If polarization sensitive measurements were desired, then the beam was first collimated with a width of approximately 0.5 in. and sent through an aperture, quarter wave plate (to convert circular polarization into linear), and a linear polarizer before focusing into the fiber. The fiber led to an OceanOptics USB4000-VIS-NIR-ES spectrometer whose output was sent to the computer for analysis. This system allows for optical measurements in the Voigt configuration and is equipped for electrical measurement (e.g., magneto-photoconductivity)

For larger magnetic field strengths, a Janis 7THL superconducting magnet and

cryostat was purchased and assembled in the lab in 2013, which has a maximum field of 7.2T and a minimum stable temperature of 3K. Much care was taken to keep all sensitive electronic components (spectrometer, laser diode controller, computer, etc.) far away from the superconducting coil, because the fringe field outside of the magnet could exceed 1 T. The photoluminescence was again collected using a large lens and focused into the nonmagnetic fiber leading to the Ocean Optics spectrometer. This system may be used in either the Faraday or Voigt configurations and is equipped for electrical measurements.

The very high field (up to 32T) measurements were performed at the National High Magnetic Field Laboratory in two different magnet cells, between two trips to Tallahassee, Florida. The first magnet cell was a superconducting magnet with a maximum field of 17.5T and a minimum temperature of 15K. This is where the Faraday configuration measurements were performed, by feeding the excitation light source into a broadband fiber that was lowered into the cryostat, while the PL was collected through a quartz window at the bottom of the system. This system was not equipped for electrical measurements, and could only be used for optical measurements in the Faraday configuration.

The other magnet system at the National High Magnetic Field Lab is the infamous "25 Tesla Florida Split Helix" that is composed of two non-superconducting coils placed end-to-end in a Helmholtz configuration. This giant magnet consumes up to33MW of power with a maximum current of 40 kA. The maximum field in the center of the magnet, where the field is homogeneous and the optical windows allow direct access to the sample, is 25 T. Directly in the middle of each coil (above and below the optical

access windows), the field could reach 32T. Electrical measurements could be performed up to 32T without optical access, but optical measurements were performed only up to 25T in the Voigt configuration. All optical measurements at the NHMFL were analyzed using the Ocean Optics spectrometer.

The a-Si samples were grown on fused silica by Dr Ben Abeles at Exxon using a low temperature plasma-enhanced chemical vapor deposition (PE-CVD) method. For electrical measurements, two 50nm thick gold electrodes were deposited by e-beam physical vapor deposition (PVD) whose pattern was determined by a shadow mask. The measurements were taken using a Keithley sourcemeter (Keithley 236/238/2400).

CHAPTER 3

OPTICALLY DETECTED SPIN SEEBECK EFFECT

3.1 Motivation

The field of spin caloritronics is in many ways limited not by the ingenuity of the scientists working on the subject, but instead by the very limited experimental toolbox that exists to detect and quantify the spin degree of freedom of electrons. To date, nearly all of the experimental literature in the field has made use of nonmagnetic (NM) metallic "spin-detection" strips on top of the ferromagnetic (FM) layer where the spin transport takes place. As discussed briefly in the introduction (Section 1.2), these NM metallic strips are prone to many magneto-thermoelectric artefacts that have often proven difficult, if not impossible, to separate from the "true" signal due to spin accumulation by the spin Seebeck effect.[17-21] Here we will discuss the problem in more depth, along with the resolution brought by optical detection methods.

The first claimed observations of the spin Seebeck effect in 2008[3] initiated great debate on several fronts. First, the question was asked: could the experimental efforts have possibly been undermined by artefacts that had not been accounted for? Second, if the observations and their interpretation as a heat-induced spin accumulation were correct, what was the underlying microscopic mechanism and how could it be improved and/or utilized for real-world applications? Imaginations went wild with possible

applications, ranging from heat sensors to radiation detectors to low-cost, waste-heat thermoelectric generators. Obviously the first step toward realizing functional devices was to agree on the experimental interpretations and to understand (and use that understanding to improve) the responsible microscopic mechanisms.

3.2 Spin Generation and Transport

As discussed in the introduction (Section 1.2), metallic ferromagnets such as NiFe are particularly difficult to design convincing SSE experiments due to the daunting number of magneto-thermoelectric artefacts that will confound the true SSE signal.[17-21] These artefacts range from classical thermoelectric effects like the Seebeck effect, to relativistic corrections to transport like anisotropic magnetoresistance, anomalous Hall effect, and spin Hall effects which all derive in some way from spin-orbit coupling (SOC).[97] Despite these artefacts (that are clear in retrospect but were not obvious at the time), the Saitoh group chose NiFe[3] as their system to probe the SSE because their prediction required the spin current to be carried by conduction electrons in the FM, which insulating ferromagnets lack entirely (by definition). Inspired by the Julliere model of giant magnetoresistance (GMR) in spin valves, their interpretation of the SSE consisted of two parallel spin transport channels with different thermoelectric properties. In the absence of strong electron-electron and electron-phonon interactions, where the "single-particle" description of band-like transport applies, Sir Neville Mott[108] showed that the energy-dependent conductivity $c(E)$ may be written:

$$c(E) = e^2 D(E) g(E) \tag{3.1}$$

where e is the fundamental electronic charge, $D(E)$ is the (energy dependent) diffusion

constant, and $g(E)$ is the density of states (DOS). The bulk conductance may be found by integrating over the energy-dependent conductance with respect to energy. This is known as the Mott formula:[108]

$$\sigma = \int c(E)(\frac{-df(E)}{dE})dE \tag{3.2}$$

where $f(E)$ is the Fermi-Dirac distribution. From the conductance, the Seebeck coefficient may be written:

$$S = \frac{-k_B}{\sigma\, e}\int \frac{E-\mu}{k_B\, T} c(E)(\frac{-df(E)}{dE})dE \tag{3.3.}$$

In a metallic ferromagnet with two distinct DOS for each spin orientation (oriented "up" and "down" with respect to the quantization axis set by the magnetization), we can model charge transport by considering the two spin channels to be simultaneously carrying current independently from one another in the same material. The distinct DOS for the two spins would naturally result in nonidentical Seebeck coefficients according to the Mott formula shown above, and an accumulation of spins of opposite sign would diffuse to opposite sides of the FM strip. This spin accumulation in the FM would then diffuse into the Pt strip, where the SHE would convert the spin current into a detectable charge current. It should also be pointed out that this interpretation would today be categorized as a spin-*dependent* Seebeck effect (S*D*SE),[2] since it is nothing more than a manifestation of the single-particle effects for two distinct spin channels and does not rely on any collective delocalized excitations (e.g., magnons, phonons).

Theorists were quick to point out several problems with this interpretation. First, the two independent spin channels may be thought of as noninteracting only on time scales less than the spin-flip scattering time T_1 which will transfer carriers from one spin

channel to the other, which is typically on the order of 1 ps. This time scale imposes a length scale L_s by the diffusion relationship $L_s = \sqrt{D\,T_1}$ where D is the electron diffusion constant. The material-dependent L_s is then dubbed the spin diffusion length, and is on the order of $10nm$ in NiFe. Therefore the SDSE-induced spin accumulation would be expected to exist only on the edges of the strip, disappearing on the length scale L_s from the edge as the two spin transport channels become "scrambled." In order to manifest over a length scale of several millimeters, it was thought that quasiparticles with a much longer mean free path such as magnons or phonons would need to contribute to the effect.

Moreover, it was observed that a small scratch in the middle of the FM film, which we would naively expect to "block" the spin current from passing between the two sides of the scratch just as it blocks charge current, left the observed SSE signal unchanged. This was interpreted in one of two ways, depending on who you asked; it was either conclusive evidence that the whole body of experimental work claiming to show the SSE in metallic structures was in fact composed of thermoelectric and magneto-thermoelectric artefacts with nothing to do with spin transport, or it was evidence that the phonon heat current in the substrate (which could bridge the gap in the film) played a crucial role in generation of spin currents. As it turns out, both sides were partially correct.

The first step toward conclusively rejecting these artefacts and confirming the true existence of the SSE came in 2010, again from the Saitoh group,[8] where Uchida *et al.* used the insulating ferromagnet Yttrium Iron Garnet (YIG) as the spin-generation layer. A voltage that was consistent with the SSE was observed in the adjacent Pt strips, just like the experiments with NiFe. However, the Seebeck/Nersnt/AHE/AMR artefacts[18]

should not manifest in YIG because it is an electrical insulator. Although Pt does have possess a nonzero Hall coefficient (like all metals), it is orders of magnitude smaller than the AHE coefficient in FM metals like NiFe and is not sufficient to explain the observed magnitude of SSE voltage. Besides, the conversion from magnon spin currents in YIG to electron spin currents in adjacent metals is routinely demonstrated using a technique called spin pumping,[46] so the theoretical interpretation that relies on magnon heat currents creating conduction electron spin currents leaves little room for doubt.

The theoretical interpretation of the SSE in insulating ferromagnets can be described by three interacting thermodynamic reservoirs, namely the magnon, phonon, and electron systems at the YIG/Pt interface. This mechanism fundamentally relies on energy transfer between the phonon and magnon systems in the FM insulator, which is converted to a spin polarization in the adjacent metal and is dubbed the "phonon-magnon drag" mechanism.[7,24-28] At the edge of the sample, where the substrate makes contact with some sort of heater in order to establish the temperature gradient, phonons are first exchanged at the heater/substrate interface. Because the substrate is nonconducting and nonmagnetic, the heat current is carried by phonons alone and only a phonon temperature can be defined inside the substrate. The phonon heat current is carried across substrate/film interface into the insulating FM film, where the local phonon temperature is raised above the local magnon temperature (see Figure 3.1). The phonon temperature is assumed to be continuous across the interface whereas the magnon temperature is necessarily only well-defined within the FM layer. Due to the local temperature difference $T_{phonon} - T_{magnon} > 0$, energy is transferred from the phonon system to the magnon system.

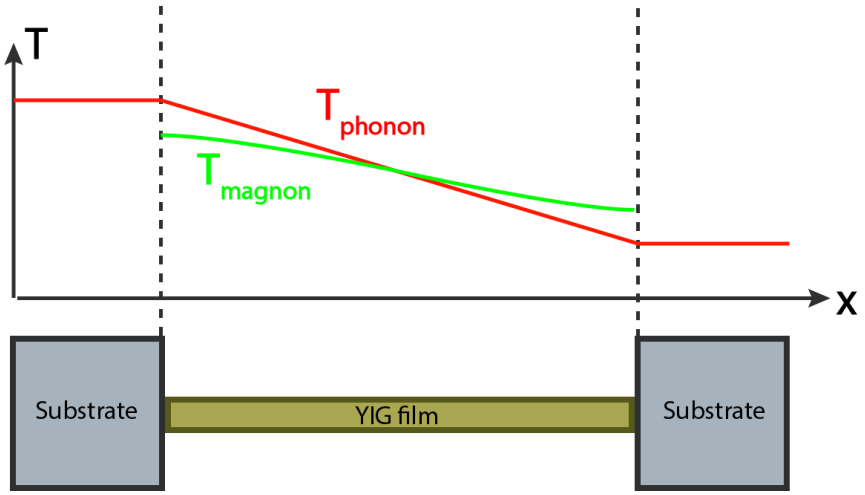

Figure 3.1. Illustration of the continuous phonon temperature across the substrate/film interfaces and the nonzero difference between the magnon and phonon temperatures due to the finite magnon-phonon interaction strength.

Magnons are thought of as spin-carrying quasiparticles which are described by their momentum k, their group velocity $d\omega(k)/dk$, and the spin angular momentum that they carry, which is always opposite from the local magnetization vector $\vec{M}$. This spin direction can be intuitively understood by remembering that a magnon is a local travelling reduction in magnetization, so its spin sense should be in the direction $-\vec{M}$ which reduces the average magnetization. Like any other particle, they diffuse from areas of high temperature to low temperature in order to come to thermodynamic equilibrium. Therefore, there is both a heat current (carried by phonons and magnons) in the $+x$ direction and a spin current (carried only by magnons) in the $+x$ direction. Although not in thermal equilibrium, this static picture will persist as long as heat is continuously delivered from the $-x$ side and absorbed at the $+x$ side. Note that this picture so far includes only the YIG film and the substrate, typically gallium gadolinium garnet (GGG), with no mention yet of the electrons in the spin detection layer.

Now we consider the effect of adding the Pt spin-detection strip to the surface of the YIG film. The phonon temperature is once again continuous across the YIG/Pt interface, and there is compelling reason to think that the electronic temperature closely follows the phonon temperature due to the frequent electron-lattice scattering in Pt. However, because of the mismatch between the YIG magnon temperature and the Pt conduction electron temperature, energy is transferred at the interface from magnons to electrons or vice versa, depending on the sign of $T_{magnon} - T_{electron}$. With this transfer of energy there is also a transfer of angular momentum (due to conservation laws), and the angular momentum direction of the magnon is always fixed in the $-\vec{M}$ direction. The electron ensemble therefore receives a constant influx of angular momentum from

magnon-electron interfacial scattering, and a spin accumulation $\mu_{\uparrow} - \mu_{\downarrow} \neq 0$ is formed at the interface. This spin accumulation then diffuses away from the interface and is converted to a detectable charge current by the ISHE. Note that because this model fundamentally relies of a description of collective magnon and phonon interactions, it is termed the "spin Seebeck effect" by the standard modern terminology.

This model based on non-equal temperatures and energy transfer between magnon/phonon/electron ensembles is well-accepted by the spin caloritronics community[24-28] in the context of insulating ferromagnets,[8-14] where the risk of magneto-thermoelectric artefacts is much lower. In reality, the picture is little more complicated because of the recent understanding of the "proximity induced ferromagnetism" (PIF) effect, where the first few atomic layers of the Pt film undergo a transition to a ferromagnetic phase due to the interface exchange interaction with the ferromagnetic YIG. This raises the possibility that the AMR/AHE/ANE effects that only manifest in a metallic FM do, in fact, appear in this system due to the several-angstrom-thick FM Pt layer. However, the robustness of the SSE signal when Pt is replaced by other metals with strong SOC (but without the PIF effect) such as tungsten serves to alleviate these concerns.

This SSE mechanism that fundamentally relies of collective excitations (rather than single-particle effects) might, in principle, apply to metallic FM systems as well. We know that magnons exist in NiFe alloys because we can directly excite them using ferromagnetic resonance (FMR) or probe their energy and momentum by Brillouin light scattering (BLS). At this point, the spin caloritronics field is simply unable to perform the experiments in metallic FM systems to conclusively prove the existence of the SSE or

SDSE using the conventional ISHE spin detection scheme. To solve this dilemma, we will take inspiration from previous studies that have investigated spin accumulation in metals and semiconductors using the magneto-optic Kerr effect (MOKE) and try to apply it to look into the SSE in NiFe.

3.2.1 MOKE and Spin Accumulation

Many groups have successfully applied the idea of using MOKE to detect imbalances in spin populations for many years before we applied it to the look into the spin Seebeck effect. One of the most beautiful applications of MOKE-detected spin accumulation occurred in 2004 when David Awchalom's group used a homebuilt Kerr microscope to unambiguously detect the spin accumulation due to the spin Hall effect (SHE) in gallium arsenide.[29-30] The spatial resolution of ~1μm allowed Kato *et al.* to locate the spin accumulation only on the edges of the GaAs strip and show that it was consistent with the SHE in sign and location, as well as magnetic field and strain dependence. Scott Crooker's group at Los Alamos National Lab is famous for using time-resolved Faraday/Kerr rotation to watch the precession and decay of optically pumped spins in semiconductors and even "spin noise" from unpolarized ensembles of electrons.[102] David Cahill has advanced the field of spin caloritronics by using time-resolved MOKE to watch the dynamic evolution of the longitudinal spin Seebeck effect in YIG/metal bilayers.[31] Cahill's group has also used time-resolved MOKE to study to growth and decay of spin accumulation in metals caused by ultrafast demagnetization in an adjacent FM, which is very similar in spirit to the spin Seebeck effect.[2] We note that another type of spin-related Seebeck effect, namely the longitudinal spin-dependent

Seebeck effect (SDSE)[[2],[33]] has been reported using time-resolved MOKE in the picosecond time domain in a nanoscale sample size.[[34],[35]]

One common trait of the experiments just mentioned is that they make use of either time-resolved MOKE to study the transient dynamics of systems on very short time scales, or they periodically modulate the source of the spin accumulation to gain the advantages of lock-in detection in their optical setup. The transverse spin Seebeck effect (TSSE) is stubbornly inaccessible to both of those techniques, because the quasi-static temperature gradients exist over a length scale of several millimeters, which is not possible to modulate at any frequency that would allow for meaningful noise rejection using time-resolved or lock-in detection schemes. Instead, we have borrowed the idea of an interferometric MOKE detection scheme with extremely low drift (<10nRad) over the time scales of minutes to hours necessary to create such large-scale temperature gradients. Moreover, the idea of applying MOKE to study the TSSE is especially appealing because previous studies (using electric ISHE detection) could only probe the geometry where the magnetization lies in the plane of the film due to the inherent directionality of the ISHE voltage. With optical detection, the in-plane magnetization or out-of-plane magnetizations can both be probed.

The mathematical/physical justification for the use of MOKE to study spin accumulation originates from the off-diagonal elements of the conductivity/dielectric tensor. If the dielectric tensor has off-diagonal elements and satisfies the relation $\varepsilon_{ij} = -\varepsilon_{ji}$, then we can diagonalize ε_{ij} to find the eigenmodes of electromagnetic radiation that will propagate in the material. Assuming an isotropic material so that $\varepsilon_{xx} = \varepsilon_{yy} = \varepsilon_{zz}$ and magnetic field and/or magnetization in the z direction:

$$\varepsilon_{ij} = 1 - \frac{4\pi i\sigma_{ij}}{\omega} = \begin{bmatrix} \varepsilon_{xx} & \varepsilon_{xy} & 0 \\ \varepsilon_{yx} & \varepsilon_{yy} & 0 \\ 0 & 0 & \varepsilon_{zz} \end{bmatrix} \tag{3.4}$$

This may be diagonalized with the choice of basis corresponding to light travelling in the z direction with left circular polarization, right circular polarization, and a z-polarized non-TEM wave:

$$E_L = \frac{1}{\sqrt{2}} \begin{bmatrix} 1 \\ i \\ 0 \end{bmatrix}$$

$$E_R = \frac{1}{\sqrt{2}} \begin{bmatrix} 1 \\ -i \\ 0 \end{bmatrix}$$

$$E_Z = \begin{bmatrix} 0 \\ 0 \\ 1 \end{bmatrix}$$

The corresponding refractive indices for left and right circular polarizations are $n_L = \sqrt{\varepsilon_L} = \sqrt{\varepsilon_{xx} + i\varepsilon_{xy}}$ and $n_R = \sqrt{\varepsilon_R} = \sqrt{\varepsilon_{xx} - i\varepsilon_{xy}}$. The circular birefringence $\Delta n = n_L - n_R$ may then be written in terms of the conductivity tensor:

$$\Delta n = \sqrt{1 + i - \frac{4\pi}{\omega}(i\sigma_{xx} + \sigma_{xy})} - \sqrt{1 - i - \frac{4\pi}{\omega}(i\sigma_{xx} - \sigma_{xy})} \tag{3.5}$$

The reflection coefficients (going from air to metal where are approximate $n_{air} = 1$) for left/right circular polarizations are complex-valued, indicating that some phase is obtained in the reflection that will differ for the two polarizations (for normal incidence):

$$R_{L,R} = \left(\frac{1 - n_{L,R}}{1 + n_{L,R}}\right)^2 = |R|e^{i\varphi_{L,R}} \tag{3.6}$$

After much algebra (which will be left to reference 31), we find the Kerr rotation angle $\theta_K = \frac{1}{2}(\varphi_L - \varphi_R)$ can be written simply as:

$$\theta_K = \frac{\sigma_{xy}}{\sigma_{xx}\sqrt{1+\frac{i}{\omega\varepsilon_0}\sigma_{xx}}} \tag{3.7}$$

Now, in principle, we need only to calculate the conductivity tensor for a given material (and the change induced by an imbalance in the spin populations), and we will know how the MOKE signal will respond to thermally-driven spin accumulation. The mathematical framework for Kerr rotation in ferromagnets was first rigorously treated by Argyres,[32] who used perturbation theory to calculate the influence of SOC on the electronic wavefunction in FM metals. He found that the off-diagonal conductivity tensor elements are proportional to:

$$\sigma_{xy} \propto \int_V dk = \frac{(no.of\ unpaired\ electrons)}{(unit\ volume)} = M_s \frac{2(2\pi)^3}{g\mu_B} \tag{3.8}$$

Here, I am adopting Argyres' notation where $\int_V dk$ indicates an integral over all states that are occupied by *non-spin-paired electrons* per unit volume. Since the magnetization is simply the density of uncompensated magnetic dipoles (i.e., unpaired electron spins) multiplied by some constant, the conductivity tensor element σ_{xy} is proportional to the saturation magnetization M_s. Furthermore, an additional accumulation of spin (due to the SSE or some other reason) will change the value of the integral $\int_V dk$ and the resulting Kerr rotation angle.

3.3 Heating Stage and Optical Alignment

With our Sagnac interferometer capable of measuring the Kerr rotation angle with a noise level of $\sim 200 nRad/\sqrt{Hz}$ and a drift of about 10nRad, we should have the ability to measure slow changes in spin accumulation due to the transverse spin Seebeck effect (TSSE). We begin by designing an experimental setup where we can continuously

monitor the (spatially dependent) magnetization while adjusting the temperature gradient across the NiFe film. The best solution, after some trial and error, was to deposit our NiFe films on a 5mmx5mm substrate by e-beam physical vapor deposition (PVD) and to glue that substrate to two copper blocks (separation between the blocks was ~4.5mm) with a thermally conductive paste (GE-varnish). Each of the copper blocks was equipped with a heating element (up to 50W) and each heater could be separately controlled by a Keithley 2400 sourcemeter. To measure the temperatures of the two blocks, T_1 and T_2, and the actual temperature gradient of the NiFe film, ∇T, it was found to be insufficient to simply attach a thermocouple to each block. Instead, to measure the physically important quantity ∇T with maximum sensitivity, we used a FLIR thermal imaging camera (FLIR model T420) with a temperature resolution of <45mK and a spatial resolution (with the appropriate lens) of ~50μm. This way we can measure the temperatures of the two blocks (which have been coated with an insulating material due to copper's poor intrinsic emissivity making it unsuitable to measure with our FLIR camera) and the spatially resolved temperature of the substrate. The measurements of these temperatures for three different substrates are shown in Figure 3.2

There is an inherent danger when performing microscopy in variable temperature environments due to thermal expansion of the sample, stage, or optical components possibly distorting the image. We can make an order-of-magnitude estimate of the maximum movement of the sample by the dimensions of the heating stage, which is approximately 1cm. The linear thermal expansion coefficient of copper is ~10^{-5} K^{-1}, and the temperature range explored in our experiments is on the order of 1K. Therefore the sample can be expected to expand/move when the stage is heated on the order of

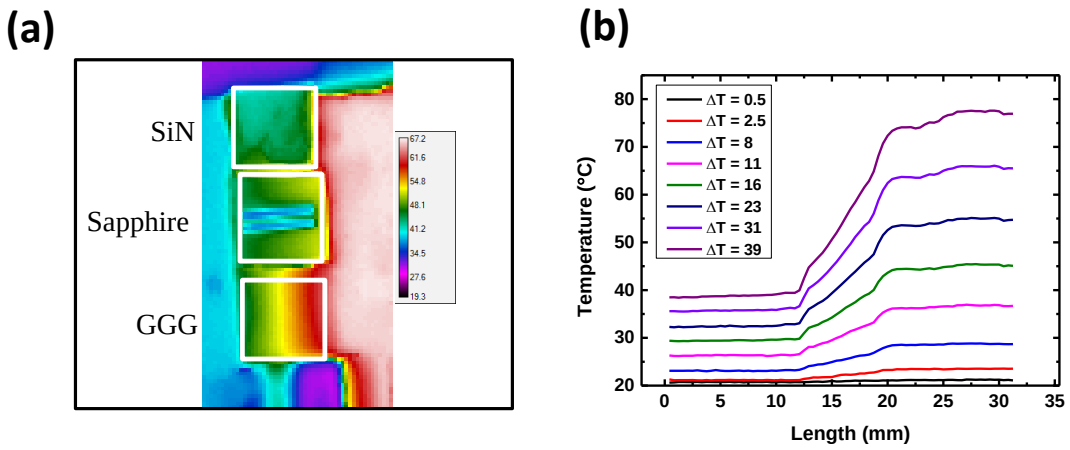

Figure 3.2. (a) The image of actual temperature profile on three substrates, recorded by the FLIR thermal IR camera (FLIR model T420). Each substrate is sketched by a white square. (b) The obtained temperature gradient on the clean GGG substrate, as a function of the difference ΔT between the hot and cold end of the copper blocks.

$1K * 10^{-5}\, K^{-1} * 1cm = 100nm$. The resolution of the Sagnac microscope is, at best, 1μm (longer working distances and correspondingly larger resolution was often used). The depth of field, which can be thought of as the acceptable "error" around the focal plane that will not affect the resulting image, is on the order of several μm and will similarly be unaffected by a drift in position of 100nm. Our use of the variable heating stage with the Sagnac microscope should be justified, although temperature changes of $\sim 10K$ or greater should be approached carefully because the thermal expansion will approach the μm range and possibly interfere with the optical setup.

As mentioned in the introduction, the MOKE technique can be sensitive to either in-plane or out-of-plane magnetization, depending of the geometry of the optical setup. We will adopt the standard terminology that the field of MOKE researchers has established in this dissertation. If the MOKE beam reflects from the sample with normal incidence (Figure 3.3 (a)), the geometry is dubbed "Polar MOKE" and is sensitive to the out-of-plane magnetization component only. If the MOKE beam is not normal to the plane of the film and the magnetization vector lies in the plane defined by the incident and reflected MOKE beam, then the geometry is dubbed the "Longitudinal MOKE" and is sensitive to *both the in-plane and the out-of-plane components* of the magnetization. In practice, the Longitudinal MOKE (L-MOKE) geometry is used with an in-plane applied field so that the out-of-plane component of M is zero and we can consider the measurement to effectively sense the (in-plane) magnitude of M. Likewise, the Polar MOKE (P-MOKE) geometry is used with an applied out-of-plane field, so that the magnetization is saturated out-of-plane and so the measurement senses the total (out-of-plane) magnitude of M.

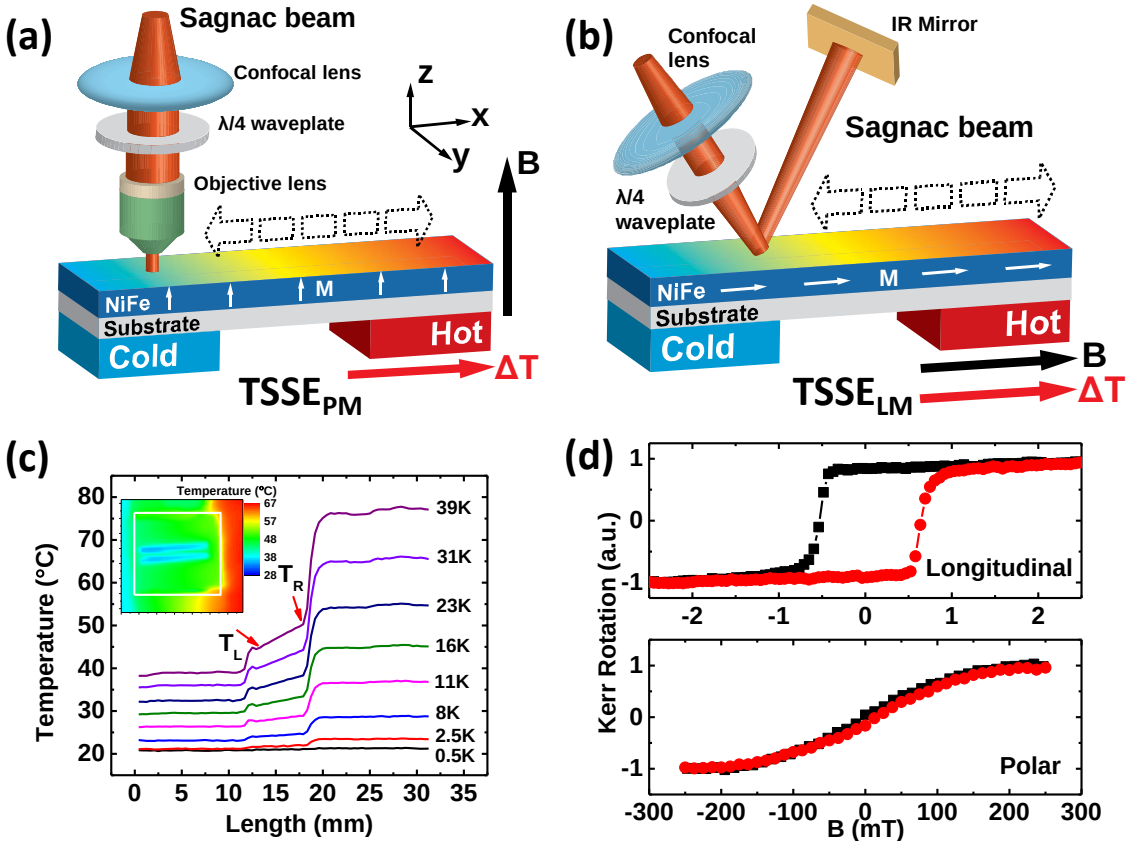

Figure 3.3. (a) and (b) Schematic illustration of the Sagnac set-up for $TSSE_{PM}$ ("polar") and $TSSE_{LM}$ ("longitudinal") measurement, respectively. (c) The obtained temperature profiles in NiFe/sapphire as a function of ΔT (denoted on the right). The inset shows an image of the actual temperature profile. The substrate with NiFe films (blue strips) on top is sketched by a white square. (d) M-H loops of a NiFe/sapphire measured in longitudinal and polar MOKE configurations.

It must be pointed out here that there is some conflict in the standard language of the MOKE and spin caloritronics fields, which has historically not been problematic because the fields have not overlapped often. In particular, the use of the term "longitudinal" appears in both fields with distinct definitions. In the spin caloritronics field, the longitudinal geometry means that the heat current and spin current are parallel, whereas the MOKE community uses the term "longitudinal" to mean that the MOKE beam reflects from the sample with some oblique (non-normal) angle. To reduce the possible confusion, we specify that we are not interested (yet) in the Longitudinal spin Seebeck effect (LSSE), which has in fact already been explored by time-resolved MOKE by the Cahill group. All of our measurements take place in the transverse spin Seebeck effect (TSSE) geometry, but the optical measurements may be either Polar MOKE or Longitudinal MOKE. From this point on, we refer to the transverse spin Seebeck effect detected by Polar MOKE (Figure 3.3 - (a)) to be $TSSE_{PM}$ and the Longitudinal spin Seebeck effect detected by Longitudinal MOKE (Figure 3.3 - (b)) the $TSSE_{LM}$. We hope that the language that we adopt is clear enough that this potential confusion is minimized.

At the risk of further complicating the already crowded landscape of terminology, we should fully address all of the possible conflicts between the MOKE field and the spin caloritronics field to minimize the possible confusion between the two. There also exists a transverse MOKE (T-MOKE) which is not used at all in our experiments and is wholly unrelated to the TSSE. The reason that we never apply the T-MOKE geometry in our experiments is because the T-MOKE is phenomenalogically similar to linear birefringence and the Sagnac interferometer, in its current form, is insensitive to it. The T-MOKE geometry results in a Kerr *Ellipticity* rather than a Kerr rotation angle because

the phase difference occurs between the *s* and *p* polarizations, where the *p* component (parallel to M) is phase shifted with respect to the *s* component (perpendicular to M), as illustrated in Figure 3.4. Because the Sagnac interferometer is sensitive only to circular birefringence, it is not possible to measure in the T-MOKE geometry, but it has been addressed here to clarify any possible confusion resulting from "duplicate" terminology between the two fields.

The magnetization of the 50nm NiFe film is strongly anisotropic with easy axis in-plane. In Figure 3.3 (d) we show the M-H behavior detected by Sagnac MOKE at room temperature with either an in-plane or out-of-plane applied field. For an in-plane applied field, the coercive field H_c is about 6mT with saturation of M occurring at 10mT. For an out-of-plane applied field, the coercive field H_c is not well defined because the magnetization reverts to the easy axis (in-plane) when the field is removed, but the saturation is seen to occur around 150-200mT. We want to perform our SSE measurement under saturation conditions so that there is no ambiguity about the direction of M, but it was not possible to find an electromagnet that suited our needs. Specifically, we would need a magnet that is capable of sustaining a 200mT magnetic field for duration of many hours with a desired stability of 10^{-5} or better, and it must not have a high-magnetic-susceptibility core (see Figure 2.9 (d) for illustration of this requirement) so that it can accommodate the Sagnac microscope in Polar MOKE geometry. We realized that a high-strength permanent Neodymium magnet with a field close to the surface of 150mT would work, because it can be incorporated into the heating stage and allow room for the Sagnac to operate in either Polar or Longitudinal mode. For this reason, all magnetic fields in our measurements were fixed at ~150mT and were supplied

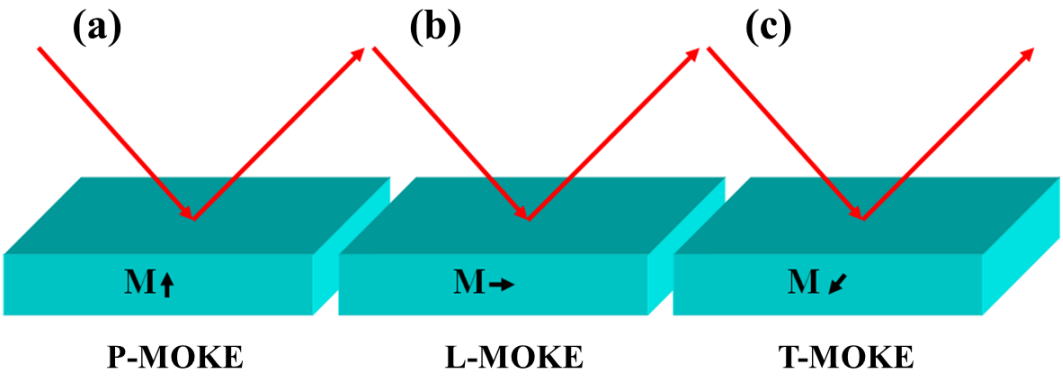

Figure 3.4. Distinction between the Polar MOKE (P-MOKE), Longitudinal MOKE (L-MOKE), and transverse MOKE (T-MOKE).

by small (9mm) permanent magnets. The additional advantage of these magnets is their high Tc of ~ 600K, which means that a small change in temperature (although they are insulated from the heating stage as well as possible) will have a negligible effect on the magnetization of the permanent magnet and, as a result, the magnetic field on our samples.

3.4 The A-B Method

We have shown that the Sagnac interferometer, equipped with a XY translation stage and objective lens, is capable of generating spatially resolved 2D images of the Kerr rotation over the surface of our films. However, because the interferometer is inherently "single-pixel," and these images must be measured by a raster-scanning method rather than taking the entire image at the same time like a digital camera. Each pixel has some minimum time necessary to measure it, due to the finite movement speed of the XY stage and the finite bandwidth of the lock-in amplification scheme. For our measurements, each pixel was allowed to average for anywhere between 0.4 and 4 h, depending on the desired compromise between Kerr angle accuracy, spatial resolution, and measurement time. Because our instrument is not capable of measuring a "live feed" of the spatially-resolved Kerr rotation, we have devised a method dubbed that "A-B method" to see the change in magnetization (and spin accumulation) due to changes in temperature.

The time needed for the heating stage to come to thermal steady-state after the heating current is applied was measured by the FLIR thermal camera to be <15 min. To visualize the spatial distribution of spin accumulation, we first scan the NiFe film at room

temperature in the absence of any temperature gradient and label this scan "A." Then a heating current is applied to the stage and at least 15 min. are allowed to pass before the second scan is started to be sure that the temperatures of the two blocks and the substrate/film are in steady-state. We then perform another scan over the same area and with the same specifications as the first scan (averaging time, spatial resolution, etc.) on the NiFe film and label this image "B." By performing a pixel-by-pixel subtraction of image "A" from image "B," we obtain exactly the quantity that we are interested in: the change in Kerr angle (or magnetization) brought about by the creation of the temperature gradient in the film.

3.5 Optically Detected Spin Seebeck Effect

Unfortunately, it is very difficult to visually determine subtle differences in plotted values using a 2D color plot like the A-B image shown in Figure 3.5. Because the temperature gradient is parallel to the x axis in the above plot and the spatial spin distribution is assumed to depend only on the x coordinate (according to previous SSE studies), we instead take an average over the Kerr angle values of each column and plot that y-averaged value of the A-B Kerr angle versus x. When we apply a small temperature gradient (~0.1-0.3K/mm) and plot the change in magnetization as a function of x, something surprising appears: on the "cold" side of the NiFe film, which remains at room temperature (to within a few mK), the magnetization increases! An increase in magnetization is typically associated with a *decrease* in temperature, according to common mathematical treatments of the theory of magnetization like Bloch's law.

Bloch's law holds general true for most magnetic materials, and states that the

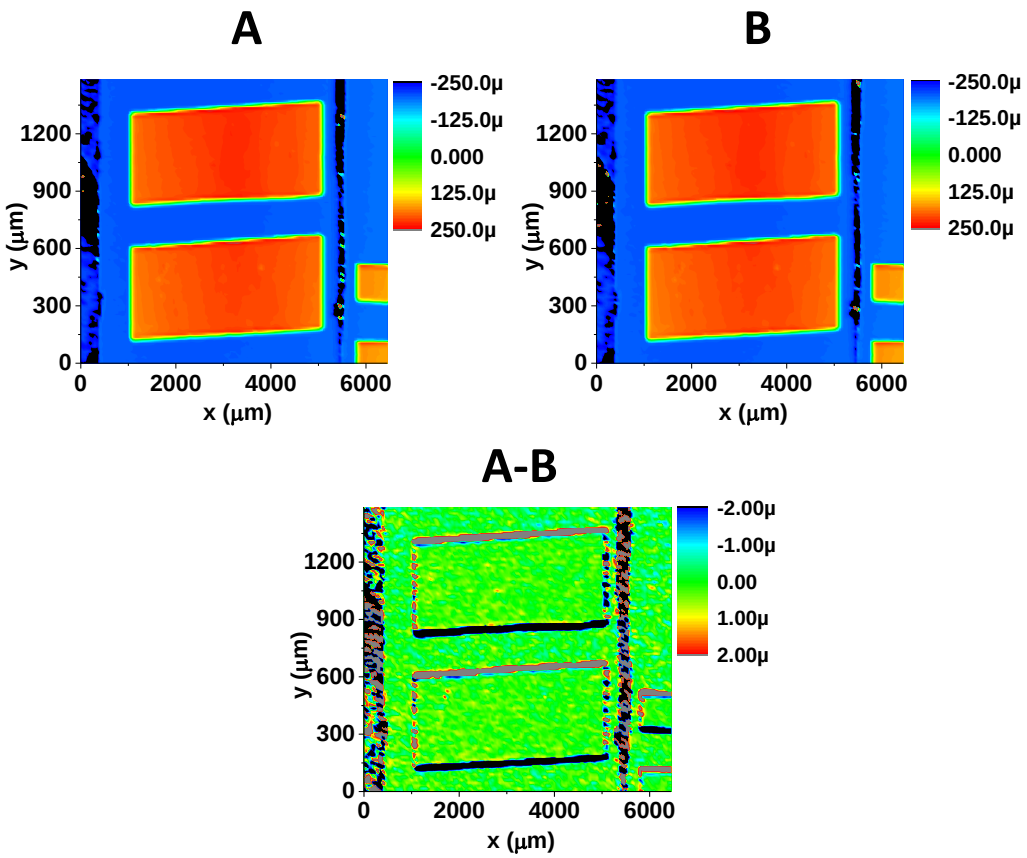

Figure 3.5. Demonstration of the "A-B" method on two adjacent NiFe films on sapphire substrate. Both scans were taken at room temperature, so the resulting "A-B" image yields a null result with noise-limited resolution that depends on the image scanning time but is fundamentally limited by the long-term drift in the instrument to ~20nRad.

magnetization should decrease with temperature as $(T/T_c)^{3/2}$, where T_c is the Curie temperature, above which the ferromagnetic phase disappears and the materials becomes paramagnetic:

$$M(T) = M(0)(1 - (T/T_c)^{3/2}) \tag{3.9}$$

For example, a close inspection of the LSMO sample (discussed in the introduction - Figure 2.8) that was measured from the temperature range from 6K to 300K displays a very close adherence to Bloch's law. For a material to *increase* in magnetization when the temperature is increased is extremely unusual.

Furthermore, the increase in temperature (measured by the FLIR camera) on the room-temperature side of the sample is on the order of a few mK, so existing theories – where the magnetization is explicitly a function of T alone – are not equipped to explain such a phenomenon. However, the theory behind the spin Seebeck effect describes a magnetization that is not only a function of the local temperature T, but also the temperature *gradient* ∇T, which influences the magnetization indirectly through an accumulation of spin-polarized conduction electrons. In addition, precious SSE studies have shown that the magnetization is *position-dependent* as well. In other words, Bloch's law must be expanded upon so that the position-dependent magnetization M is now written as some function $M(T, \vec{r}, \mathrm{dT/dx})$. Figure 3.6 demonstrates the spatially resolved magnetization after applying a temperature gradient to the sample.

It is important to note that our optical approach has one clear disadvantage when compared to electrical detection schemes: while the ISHE voltage form the Pt spin detection strips is a function only of the spin current through the Pt. The actual value (and

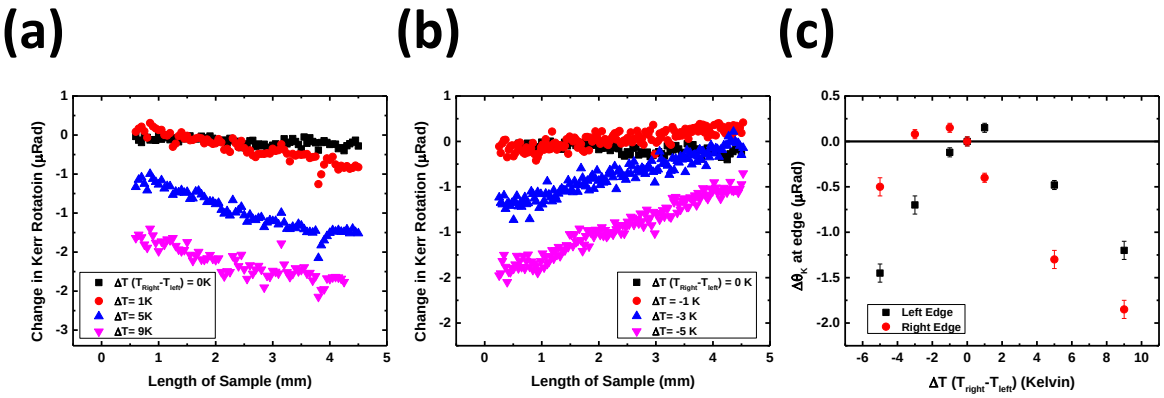

Figure 3.6. Dependence of the TSSE-related MOKE angle on the heating power measured in a NiFe film deposited on GGG substrate. (a) The film is heated only from the right side, with $\Delta T = T_{Right} - T_{Left}$ ranging from 0 to 9 Kelvin. (b) Film heated from the left, with ΔT ranging from -5 to 0 Kelvin. (c) Kerr rotation angle measured at the left (black) or right (red) edge of the NiFe strip. With ΔT larger than ~3K, the regular heating effect on the film's magnetization dominates the signal and the magnetization is observed as monotonically decrease. For sufficiently small temperature gradients, the increase in Kerr rotation angle due to the TSSE is clearly visible.

any changes) of the magnetization do not affect the spin current as long as they are not accompanied by a difference in spin chemical potential. The MOKE detection, on the other hand, measures something proportional to the total magnetization of the material, which is affected by spin accumulation but also is reduced by homogeneous heating. In Figure 3.6, it is clear that the minor increase in magnetization at modest temperature changes (<3K) is overwhelmed by the "regular" decrease in magnetization as we heat the sample further. Unfortunately, we are therefore limited to small changes in temperature around room temperature to unambiguously identify the spin accumulation signature.

The anomalous increase in magnetization on the room temperature side of the FM strip can be explained as a signature of spin accumulation due to the spin Seebeck effect only if we can first confirm that NiFe films do not actually increase in magnetization in response to a *uniform* temperature increase. Materials that behave in this way are uncommon, but not unheard of. Furthermore, although we have designed the experiment to utilize an in-plane temperature gradient, it is possible that an unintentional out-of-plane thermal gradient exists due to heat loss at the surface of the film (either from radiation of convection through the surround atmosphere). The possibility of this artefact has been thoroughly discussed in the SSE literature,[17-21] and computational simulations provide convincing evidence that many of the alleged reports of the TSSE in the literature are actually the result of the *longitudinal* SSE with an unintentional out-of-plane thermal gradient. If the anomalous increase in Kerr rotation on the cold end of the strip is due to either uniform heating *or* an out-of-plane thermal gradient, then it should manifest when we heat both the left and right sides of the substrate equally (from the bottom of the substrate) and observe the Kerr rotation from the NiFe film on top. If the magnetization

of the NiFe film is observed to decrease monotonically (Figure 3.7) when the substrate is heated *without the in-plane gradient*, then both of these potential artefacts can be dismissed with just one experiment.

Indeed, when the heat is supplied uniformly to the entire substrate so that the film is heated uniformly (or possibly with a small out-of-plane gradient due to heat loss at the surface), no increase in Kerr rotation is observed in the same temperature range. The magnetization decreases monotonically with increasing temperature, as expected from the conventional understanding of ferromagnetism. For added confidence in this claim, the temperature-dependent magnetization of the NiFe films was measured by Superconducting Quantum Interference Device (SQUID) magnetometry with both an in-plane and out-of-plane film, and the same conclusion was reached.

It has been proposed in the SSE literature that the source of the unintentional out-of-plane temperature gradient[18] that causes the LSSE to manifest is, in fact, due to the presence of the metallic ISHE spin detection strips and electrical contact wires soldered or wire-bonded to those strips. Because the thermal conductivity of Platinum is very high (on the order of 70 W m^{-1} K^{-1} at room temperature), the platinum strips that are deposited on the FM film in electrically detected SSE experiments act at large heat sinks and draw heat away from the interface (possibly through the contact wires as well). The interfacial heat current activates the phonon-magnon drag mechanism and creates a spin current that is parallel with the out-of-plane heat current, which constitutes the Longitudinal SSE, regardless of whether the experimenters attempt to provide an in-plane gradient or not[17-21]. Our optical measurement is therefore very powerful for an unanticipated reason: the lack of heat-sinking electrical pads on the FM film allow the desired temperature profile

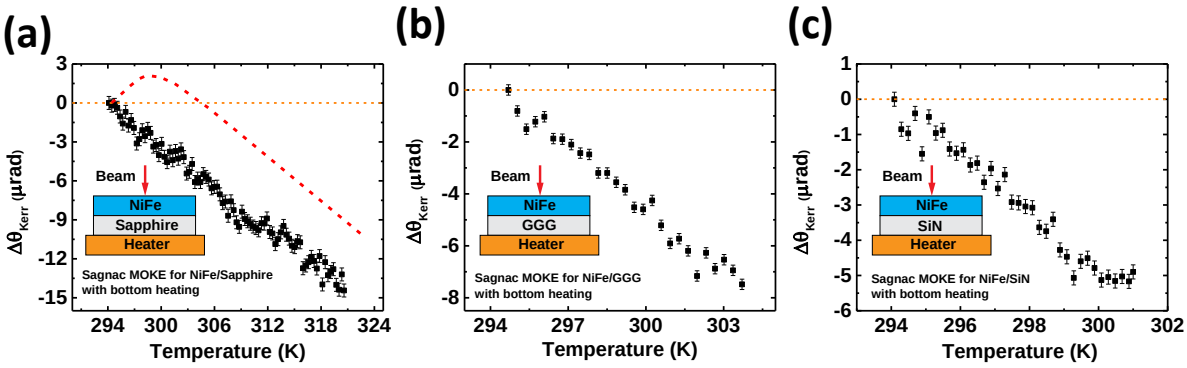

Figure 3.7. Sagnac MOKE measurements on the top surface of a NiFe film on three different substrates (same samples that were used in our reported work) with uniform heating from the bottom. The dashed line in panel (a) shows the expected response if perpendicular thermal gradient would exist.

to be minimally perturbed so that the response to a truly in-plane gradient may be explored. Additionally, our NiFe films are all prepared with a thin (20nm) SiO_2 barrier to prevent the formation of oxide layers as they are measured in the open air. The thermally insulating properties of SiO_2, make it a perfect choice to reduce the heat current at the NiFe/SiO_2 interface. An interesting future direction for this type of experiment would be to perform these experiments under vacuum so that even the effect of heat loss from the surface of the FM film (or the SiO_2 layer) to the surrounding air may be eliminated.

The spin-dependent Seebeck effect is not expected to manifest on length scales larger than the spin diffusion length, so an explanation in terms of the single-particle DOS and Seebeck coefficients (similar to that of the seminal 2008 spin Seebeck paper from the Saitoh group) is not likely to be physically accurate here. Instead, we assume that some interplay between long-range excitations, namely magnons and phonons, is responsible for the observed electron spin accumulation. This is the prevailing explanation for the SSE in magnetic insulators (dubbed the phonon-magnon drag model). Up until now, it has been extremely difficult to quantitatively test the predictions of the phonon-magnon drag model in metallic FM systems due to the overwhelming number of magneto-thermoelectric artefacts that one encounters. The phonon-magnon drag model depends critically on the density of phonons in the substrate and the interaction cross section for phonons to transfer energy to (or receive energy from) the magnon reservoir in the FM film. If the substrate is exchanged for a different material with different phonon characteristics, we should be able to tune the exchange of energy between the phonon/magnon systems and see a resulting change in the magnetization dynamics. To avoid complicating the experiment too much, we stick to the same magnetic system

($Ni_{81}Fe_{19}$) that was grown under the same conditions with the same thickness of SiO_2 capping layer for all of the experiments described in this Chapter. Three different substrates were tested in this way, chosen to have thermal conductivities, and therefore phonon densities, varying over a wide range. Those substrates are GGG (thermal conductivity $\sigma = 7.5\ W\ m^{-1}\ K^{-1}$), sapphire ($\sigma = 27\ W\ m^{-1}\ K^{-1}$), and silicon with a silicon nitride capping layer ($\sigma_{Si} = 135\ W\ m^{-1}\ K^{-1},\ \sigma_{SiN} = 135\ W\ m^{-1}\ K^{-1}$). The change in thermal conductivity has another interesting impact on the transfer of heat between the substrate and the FM film: the acoustic impedance mismatch (or Kapitza resistance)[4] is determined by the available phonon states on either side of the interface, and a large mismatch in phonon frequencies and/or velocities will result in a reflection of phonons (and reduced interfacial thermal conductivity) at the "barrier" formed by the substrate/NiFe interface.

The SSE-induced spin accumulation was measured on all three substrates in both the in-plane magnetization ($TSSE_{LM}$) and the out-of-plane magnetization ($TSSE_{PM}$) configurations. The results are shown in Figure 3.8. Immediately, two interesting observations can be made: there is not only a substantial difference in the magnitude of the increased magnetization on the room temperature side of the film as the substrate is changed, but also for all three substrates, there is a large anisotropy in the effect with the direction of magnetization.

Note that the temperature gradient values were chosen specifically so that the "regular" monotonic decrease in magnetization on the hot side of the strip could be observed at the same time as the "anomalous" increase in magnetization on the cold side of the strip. All six measurements were also taken at higher values of ΔT=T_Hot-T_Cold,

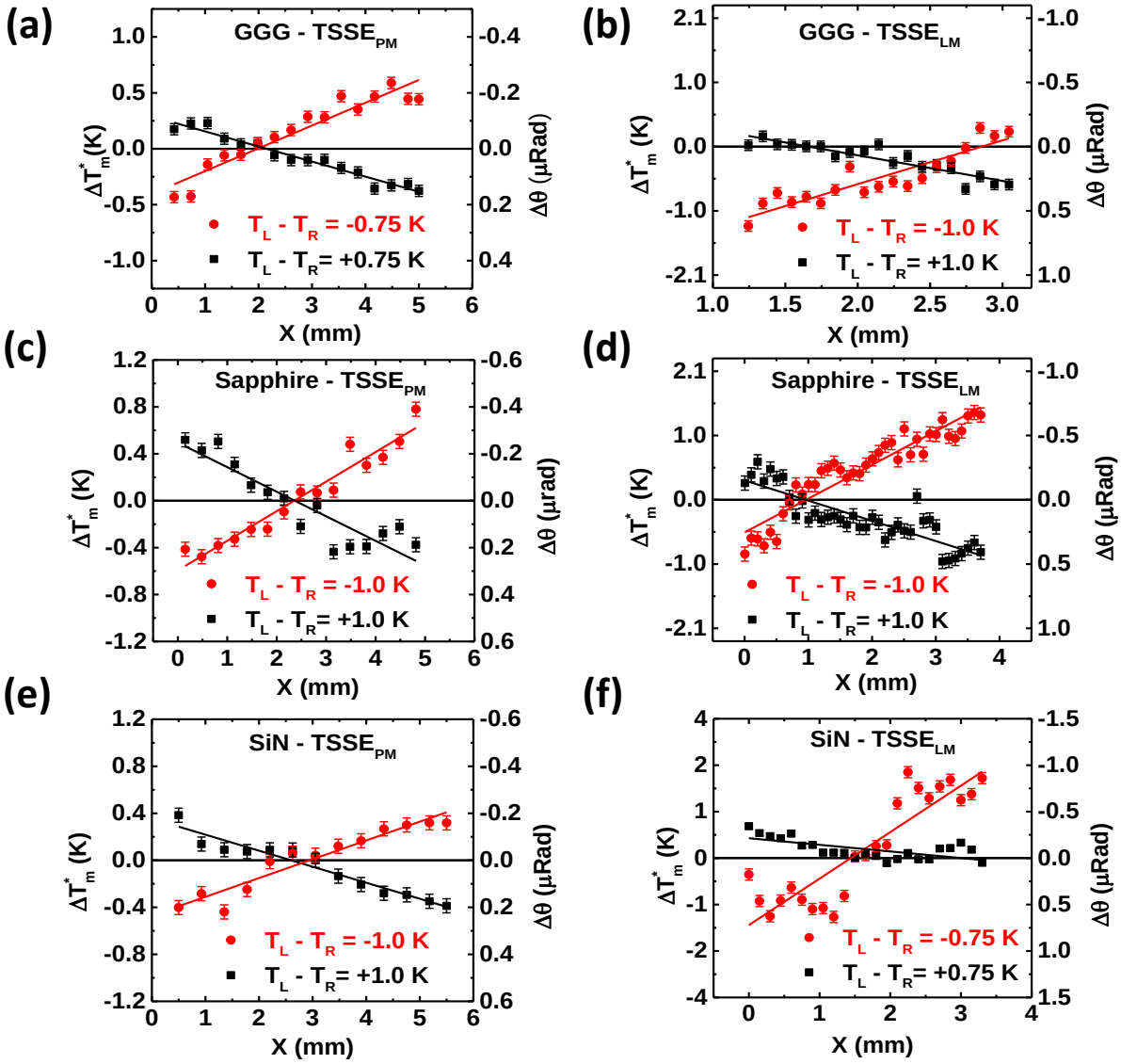

Figure 3.8. The profile of the TSSE-related Kerr angle, $\Delta\theta(x)$ (right y-axis) and the corresponding profile of $\underline{T_m^*}(x)$ (left y-axis) measured in NiFe strips on three different substrates GGG (a-b), sapphire (c-d), and SiN (e-f), in both '$TSSE_{PM}$' and '$TSSE_{LM}$' configurations having different ΔT (=T_L-T_R) as denoted.

but the results are identical to those in Figure 3.6; at higher heating powers, the regular monotonic magnetization decrease overwhelms the small spin accumulation and Bloch's law becomes a good approximation for the M(T) dependence of the film.

The most straightforward way to mathematically describe the magnetization profile is to assume a term that depends only on the local lattice temperature T (per Bloch's law) and also the difference between the local phonon and magnon temperatures, T_p and T_m, respectively. The change in Kerr rotation after heating, $\Delta\theta(x)$, is written:

$$\Delta\theta(x) = \theta(x)\text{-}\theta_0(x) = -K_T\left(T_P(x)\text{-}T_0\right) + G_{KS}(T_p(x)\text{-}T_m(x)) \qquad (3.10)$$

Here, K_T is the coefficient that relates the regular monotonic decrease in magnetization in the presence of uniform heating to the local phonon/magnon temperatures, which are assumed to be equal without a thermal gradient. The other coefficient, G_{KS}, includes a number of independent factors such as the Kapitza mismatch[4] at the substrate/film interface, the cross section for phonon-magnon energy transfer, and the strength of the mechanism (which is not currently well understood), which dictates the conversion between nonequilibrium magnons and the resulting spin accumulation. We conclude that it is not possible to measure each of these factors independently with any satisfactory precision, so we take only the phenomenological factor G_{KS} to represent the combined influence of them all. However, by changing the substrate, we affect only the factors which are relevant to the substrate phonons and the impedance mismatch at the substrate/film interface, so there is some tunability in G_{KS} that future experimentalists may explore.

The coefficient K_T, which relates the regular decrease in magnetization to the local temperature (in equilibrium), is straightforward to measure. For each of our three

substrates and in each of the two configurations (for a total of six measurements), we may simply plot the measured Kerr rotation value with the temperature of the film, as measured by FLIR camera. The substrate is heated uniformly to eliminate the effect of the SSE (which manifests only the $\nabla T \neq 0$). Figure 3.9 shows the results of these six experiments, while Table 3.1 lists the resulting K_T coefficients. Because the films are all identical (only the substrates differ), the values of K_T are all in the range of $\sim 500 \pm 100\, nRad/K$. In addition, due to the uncertainty in measuring the true local phonon/magnon temperatures, we assume that $T_p(x) - T_m(x) \propto dT_P/dx$, which is consistent with the accepted phonon-magnon-drag model. We therefore define the TSSE coefficient S_K (also listed in Table 3.1) as:

$$G_{KS}(T_p(x) - T_m(x)) \equiv S_K \, {dT_P}/{dx} \tag{3.11}$$

The coefficient S_K is estimated simply from the rise in Kerr Rotation on the side of the strip that remains at room temperature, so that the effect from the Bloch-like $M(T)$ term vanishes there.

3.5.1 Anisotropy and Substrate Dependence of TSSE Coefficient

As mentioned earlier, the dependence of the TSSE coefficient S_K naturally has some dependence on the thermal conductivity of the substrate due to the inherent importance of the phonon-magnon interaction at the interface. To further quantify the impact that the phonon-magnon interface interaction has on the magnon properties, we can probe the magnon population directly in an energy-resolved manner using Brillouin Light Scattering (BLS) spectroscopy[22-23]. BLS spectroscopy is a highly sensitive method for measuring Stokes (or anti-Stokes) shifted photons that have inelastically

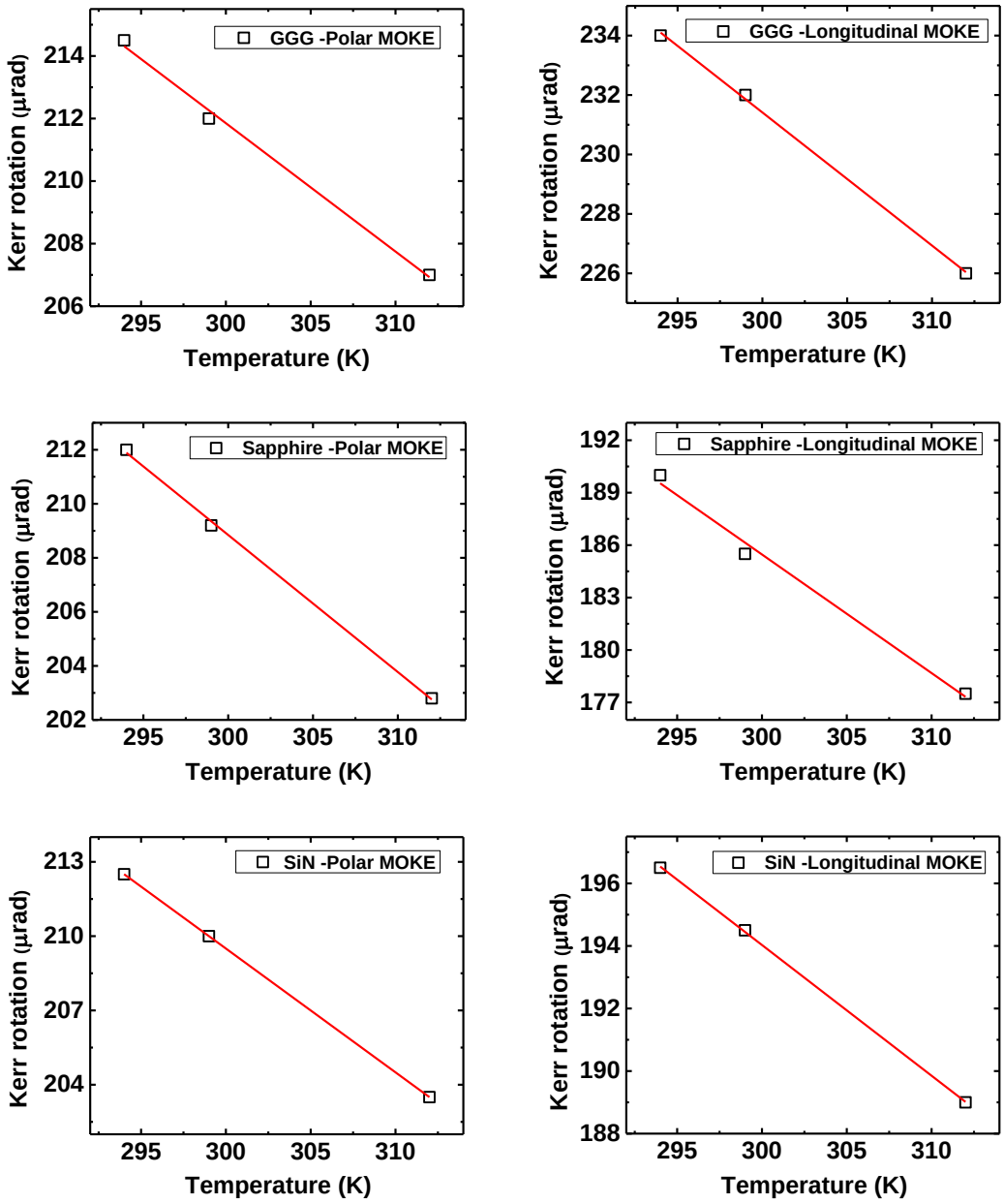

Figure 3.9. Uniformly heated NiFe film deposited on three different substrates that show temperature dependence of MOKE rotation angle for (a-c) polar MOKE, and (d-f) longitudinal MOKE. Each measurement was fitted with a relation that is linear in T, $\theta_K(T) = \theta_K(300) - K_T(300 + T)$, which is a valid approximation near RT. The fitted linear coefficients, K_T for each substrate are listed in Table 3.1.

Table 3.1: The obtained optical SSE coefficients $TSSE_{PM}$ (S_K^P) and $TSSE_{LM}$ (S_K^L), Kerr rotation sensitivities (Kerr vs. T), BLS magnon frequencies in two configurations, and thermal conductivities for GGG, sapphire, and SiN substrates.

	NiFe on GGG	**On Sapphire**	**On SiN**
$TSSE_{PM}$ (nRad·K^{-1}·mm^{-1})	90 ± 20	190 ± 30	290 ± 25
$TSSE_{LM}$ (nRad·K^{-1}·mm^{-1})	1,080 ± 90	970 ± 65	490 ± 95
PM-Kerr vs T (nRad·K^{-1})	-410 ± 50	-510 ± 50	-500± 50
LM-Kerr vs T (nRad·K^{-1})	-450± 50	-680 ± 50	-420 ± 50
BLS frequency (PM) (GHz)	4.6, 13.2	4.0, 16.2	4.9
BLS frequency (LM) (GHz)	10.2	10.7, 20.2	10.5
Substrate $\sigma_{thermal}$(W·m^{-1}·K^{-1})	7.5[40]	25[41]	135 for Si[38]; 2 to 5 for SiN[39]

scattered from with a magnon in the FM film. This allows for a direct probe of the magnon frequencies (which are typically in the regime of 1-10GHz for low-energy magnons) and the variation of those frequencies with temperature, magnetic fields, etc. This technique has, in fact, been used previously to attempt to study the spin Seebeck effect using purely optical means by measuring the magnon and phonon temperatures independently by their Stokes-shift frequencies and intensities. Unfortunately, the temperature resolution by the BLS method is on the order of several Kelvin (for both magnons and phonons)[22-23], which was found to be insufficient to detect a nonzero $T_p(x) - T_m(x)$ over the length of the film. We can, however, detect a clear difference in the magnon frequencies when the substrate is changed from GGG, sapphire, or SiN on Si, in both the in-plane and the out-of-plane magnetization geometries (Figure 3.10).

This shift in magnon frequencies is likely to be at least partially responsible for the observed difference in S_K, since a change in the magnon energy eigenstates will result in different occupation numbers in thermal equilibrium (according to Bose-Einstein statistics). The underlying microscopic mechanism responsible for the shifts in magnon frequencies as the substrate is changed lies in the microscopic details of the substrate/film interface. If the interface is smooth and hard, meaning that there is little thermal diffusion of the NiFe film into the substrate as it is deposited, then the magnetization is effectively pinned at the interface and the available magnon modes become quantized in the Fabry-Perot cavity created by the top and bottom of the FN film. On the other hand, if the interface quality is poor, the surface roughness of the interface results in poor Fabry-Perot mode quantization and scattering of magnons at the interface.

The anisotropy of S_K with respect to the magnetization direction (in-plane or

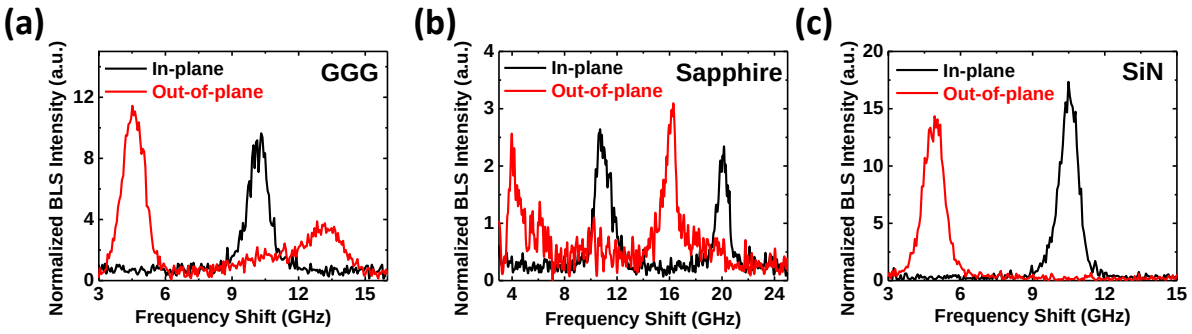

Figure 3.10. Brillouin light scattering (BLS) spectra of NiFe film deposited on (a) GGG, (b) sapphire, and (c) Silicon Nitride, measured at a fix magnetic field B=1.5 kG. The center frequencies of each BLS-detected magnon peak are listed in Table 3.1. The magnonic origin of the obtained bands was verified by applying different magnetic fields; magnon frequencies blue-shift with B, whereas phonon frequencies do not.

out-of-plane) likely originates from the anisotropy in the magnon group velocity. For low- energy magnons in a cubic crystal lattice (NiFe have an FCC structure), the magnon dispersion relation E vs. k can be approximated as a quadratic function, with two free parameters specifying the group velocity parallel with and perpendicular to the magnetization vector.

$$E(\vec{k}) = E_0 + A\,k_{||}^2 + Bk_{\perp}^2 \tag{3.12}$$

where A and B are constants with units of $eV * nm$, $k_{||}$ is the component of the magnon wavevector parallel with the magnetization vector $\vec{M}$, and $k_{\perp}$ component of the magnon wavevector perpendicular to the magnetization vector $\vec{M}$. If $A \neq B$, we would expect that the magnon thermal conductivity (and likely the magnon-electron interaction cross section) are also anisotropic with respect to $\vec{M}$.

3.5.2 SSE versus SDSE and Transverse versus Longitudinal SSE

I have claimed up until now that the effect that we observe is the transverse spin Seebeck effect (TSSE). In principle, a similar signal might be observed if the underlying mechanism were the spin-dependent Seebeck effect (SDSE) or if an unintentional out-of-plane thermal gradient existed, which would raise the possibility of the longitudinal spin Seebeck effect (LSSE)[17-21]. Here we hope to provide convincing control experiments that show that the observed phenomenon demonstrates a spin current that is perpendicular to the in-plane heat current (justifying the "transverse" terminology)[2] and that the underlying physical mechanism crucially depends on the interaction of long-range, many-particle excitations, constituting the SSE label (as opposed to the SDSE label) by Bauer's definition scheme.

The SSE versus SDSE debate is the most straightforward to answer, so I will begin by discussing it. If the observed spin accumulation depended only on the spin-dependent single-particle density of states (DOS) of the NiFe film, which is not impacted by the substrate under the FM film, there we would observe the same value of S_K regardless of the substrate. What we actually observe is a definite dependence of S_K on the choice of substrate, with a clear trend in the relationship between S_K and the thermal conductivity of the substrate. Furthermore, the macroscopic length scale over which the effects manifests is in stark contrast with theoretical estimates of the length scale over which the SDSE should work, namely the spin diffusion length, which is only ~10nm in NiFe.

Distinguishing between the TSSE and the LSSE is more subtle, since we are incapable of gathering information about the spin accumulation in the bulk of the NiFe film. The MOKE laser only penetrates a distance (and is sensitive to spin accumulation) into the metallic film determined by the film's conductivity at the laser frequency. This distance L_{opt}, known as the optical penetration depth, is approximately 15nm in NiFe. If we are correct in our assignment as the TSSE and the spin current is perpendicular to the in-plane thermal gradient, then the sign of the spin accumulation on the top and bottom of the film should be different and should decay into the bulk of the film with a characteristic length scale λ_s, the spin diffusion length (~10nm). If the spin current in parallel with the in-plane thermal gradient (constituting the LSSE), then the spin accumulation will be a function of x only and not z, the depth into the film. We can test our assignment by making another sample where the film thickness d is less than L_{opt} (but not necessarily λ_s). With a film this thin (Figure 3.11), the Sagnac MOKE laser is

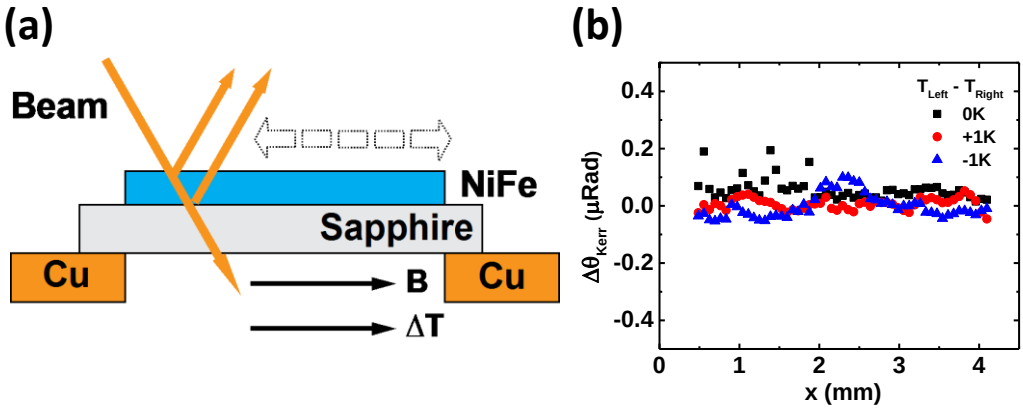

Figure 3.11. (a) Schematic illustration of the NiFe film in $TSSE_{LM}$ configuration (in-plane thermal gradient and in-plane magnetic field with the longitudinal MOKE detection). The thickness of NiFe film is 5 nm which is transparent to the Sagnac beam (λ:1550 nm). Therefore, the MOKE collects signals from the both top and bottom interface of NiFe film. (b) δθ(x) when applying an in-plane magnetic field of 1.5 KG. The null response indicates the cancelled out spin accumulation from two interfaces, providing a direct evidence for TSSE.

effectively sensitive to the magnetization throughout the entire thickness. If the sign of the change in magnetization is opposite on the top/bottom of the film, the MOKE signal from the anomalous increase in magnetization will disappear because the contribution from the top and bottom of the film add destructively to cancel each other out.

As an additional "sanity-check" control experiment, is it important that we confirm that the anomalous rise in Kerr rotation at the cold end of the FM strip is not due to long-term drift in some other influential quantity, for example the temperature in the laboratory in which the experiment takes place. It is conceivable, however unlikely, that the similar time of day which the experiments were all performed (say the late afternoon) was associated with a drop in temperature due to the ambient conditions outside the building. If the lab temperature drop between the "A" scan and the "B" scan that are essential to our "A-B" method, then the magnetization will naturally appear to rise because the sample will have come to thermal equilibrium with the new (lower) room temperature and the equilibrium magnetization will rise correspondingly. In Figure 3.12, we show that the characteristic time for the anomalous increase in magnetization to appear (after turning on the heater in the sample holder) is about 15 min. – exactly the same as the time needed for the heating stage to arrive at steady state conditions. This ensures that the measured signal is, in fact, due to the thermal gradient purposefully introduced, and not a slow (and possibly periodic) drift in the Sagnac instrument or the temperature of the room.

A highly desirable extension of our experiment would be to directly measure the local magnon and phonon temperatures, just like the micro-BLS experiment attempted in references 22-23. The phonon-magnon-drag mechanism, which is largely accepted by the

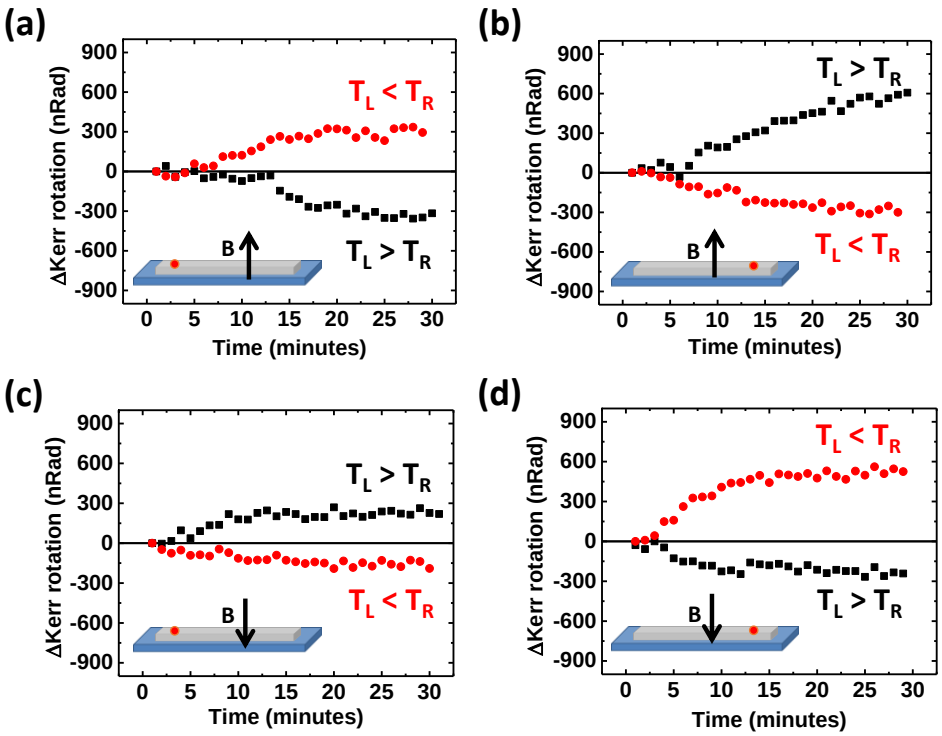

Figure 3.12. Time evolution of the TSSE-related Kerr rotation angle in a NiFe strip deposited on GGG substrate subjected to a temperature gradient of 0.2K/mm. The insets show schematically the measurement geometry where the position of the Sagnac laser spot (red circle) and orientation of the magnetic field vector (black arrow) are denoted.

spin caloritronics community, implies that the local phonon temperature T_p is greater (less) than the local magnon temperature T_m on the hot (cold) end of the FM strip. In principle, we can take the $\theta_{Kerr}\ vs. T$ calibration from Figure 3.4 and naively identify any measured Kerr rotation angle with a magnetization temperature which we denote as T_m^*. We attempted that process and the result is shown in Figure 3.13.

The result of this process shows a surprising conclusion: the "magnetization temperature" T_m^*, which was naively extracted from the local Kerr rotation, is not equal to the local phonon temperature (as expected) but in the exact opposite way from that which is predicted by the phonon-magnon-drag model. Rather than concluding that the phonon-magnon-drag model is invalid, we instead must conclude that the "temperature" is actually not well defined (the meaning of such a statement is more accurately defined in Section 1.2.2). Because the SSE takes place under inherently nonequilibrium conditions, and in fact we expect that the magnon temperature is not equal to the electronic temperature(s), we are not justified in taking the $\theta_{Kerr}\ vs. T$ calibration from Figure 3.9 (which was taken under conditions of thermal equilibrium) and identifying a temperature with any value of θ_{Kerr}. We can reasonably infer that the Kerr angle θ_{Kerr} is actually more sensitive to subtle changes in the conduction electron system than changes in the magnon population. This makes sense intuitively, because θ_{Kerr} is determined by the off-diagonal elements of the conductivity tensor, and the conductivity is almost entirely determined by the characteristics of the electronic population at or near the Fermi level. A small difference in chemical potential between the two electron reservoirs ("spin up" and "spin down") will naturally lead to a large change in Kerr angle, dubbed $\Delta\theta(x)$ in our treatment above.

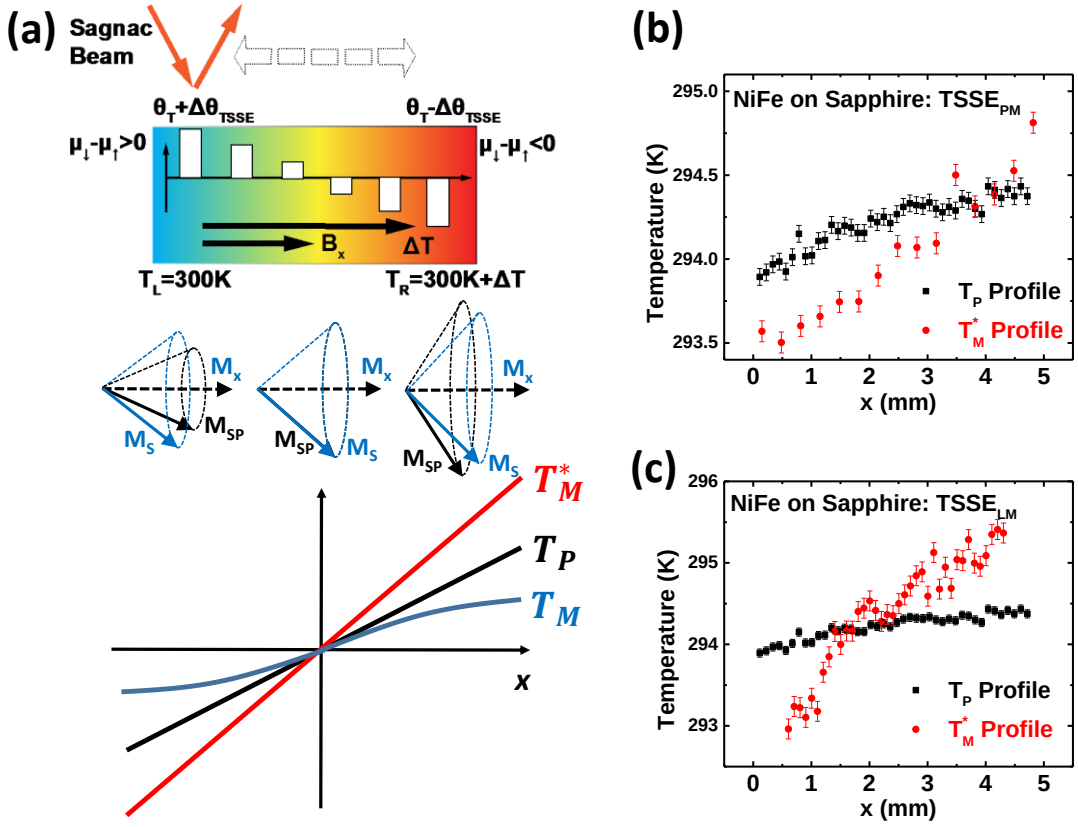

Figure 3.13. (a) *Top panel*: Illustration of opposite spin accumulation ($\mu_\uparrow$-$\mu_\downarrow$) that is formed at each end of a NiFe strip when ΔT is applied in the $\boldsymbol{x}$ direction. *Middle panel*: the cone precession angle of the magnetization vector as a function of $\boldsymbol{x}$ formed upon the temperature gradient, where M_{SP} (black arrows) and M_S (blue arrows) represent the equilibrium magnetization at T_P and the actual nonequilibrium magnetization at T_m. *Bottom panel*: the three temperature profiles (not to scale) in a heated FM metal film; T_P, T_m and $\boldsymbol{T^*_M}$. (b) and (c) The obtained T_P and T_m^* profile (as denoted) measured in NiFe/sapphire structure by thermal camera and MOKE, respectively in the $TSSE_{PM}$ and $TSSE_{LM}$ configuration.

3.5.3 Future Directions

One of the main reasons that the metallic ferromagnet NiFe was chosen as a testing ground for our new SSE optical detection scheme was the fact that NiFe is inaccessible to conventional electrical detection schemes. This made it an appealing system for its novelty and unexplored physics, but there is no reason that our Sagnac MOKE scheme could not be applied to magnetic insulators as well. An interesting avenue for further research (which is being pursued by Prof. Sun at North Carolina State University) would be to use the combination of the Sagnac microscope and FLIR thermal camera to measure the actual difference in phonon and magnon temperatures in the magnetic insulator YIG. Due to the lack of conduction electrons in YIG that are available to be spin-polarized, the local Kerr rotation angle is actually in one-to-one correspondence with the local magnon temperature T_m. A rough estimate of the power of such a method (based on the ~10nRad drift in the Sagnac MOKE instrument and the Kerr rotation response of YIG) yields a magnon temperature sensitivity for the Sagnac microscope of 50mK, which is a drastic improvement over schemes such as micro-BLS which has a temperature resolution of ~1K[22-23]. The best resolution of the phonon temperature T_p that can be attained from a thermal imaging camera is on the order of 10mK. This ability to precisely measure $\Delta T \equiv T_p - T_m$ might prove enough to validate one of the key assumptions of the phonon-magnon drag model or to put excellent constraints on the magnon-phonon interaction strength. With an optically transparent (i.e., electrically insulating) ferromagnet, the resolution of the Sagnac MOKE microscope can be improved further by using an arbitrarily thick sample and operating the instrument in transmission (Faraday rotation) mode, thereby enhancing the background angle

$\theta_{Faraday}$ and therefore improving the important quantity $\Delta\theta/\theta = \Delta M/M$.

Also on the "to-do list" is the task of returning to the experimental goal for which the Sagnac interferometer was built at the University of Utah in the first place – to investigate the *injection* of spin-polarized electrons from one material to another. This is, after all, a critical step in the eventual goal of designing functional spintronic devices that likely will require spin transport across interfaces and heterojunctions composed of two different materials. This might be accomplished by electrical spin injection (e.g., spin valve geometry) or by ferromagnetic resonance driven spin-pumping. In either case, the Sagnac interferometer should prove a powerful tool for probing spin transport and accumulation in a noncontact and minimally invasive manner.

CHAPTER 4

MAGNETIC FIELD EFFECTS STUDIES OF HYDROGENATED AMORPHOUS SILICON

4.1 Microscopic Prerequisites for Magnetic Field Effects

As discussed in the introduction, the existence of spin-dependent recombination and dissociation processes in semiconductors opens up the possibility to study those processes by magnetic field effect spectroscopy. The observation of large magnetic field effects in amorphous hydrogenated silicon (a-Si:H) is therefore a powerful window into the microscopic dynamics governing charge separation, dissociation, transport, and recombination. For our purposes, we will generally define the magnetic field effect (MFE) on a measurable quantity X, dubbed "MX(B)" for magneto-X being a function of the applied magnetic field B, as

$$MX(B) \equiv \frac{X(B)-X(0)}{X(0)} \tag{4.1}$$

The quantity X, in practice, might be the conductivity, absorption, photo/electro-luminescence efficiency, luminescence polarization, or more. It can even encompass mechanical effects such as magnetostriction, although such effects are not treated in this dissertation and are not expected to manifest outside of ferromagnetic materials. First, it is both natural and necessary to ask the question, "Why should a magnetic field affect the quantity X?" In order to answer that question, let us first discuss the prerequisite factors

that determine whether (and to what extent) an arbitrary measurable quantity X could, in principle, be a function of the local magnetic field strength. We will first group the wide selection of magnetic field effects written about in the literature[56,62,65,81,89,104] into three categories, depending on the number of charge carriers participating in the process. Those three categories are dubbed single-particle, two-particle, or many ($\geq$ 3)-particle effects. Let us first make an overview of these three categories and make some useful generalizations about each type of magnetic field effects – that will be useful when we are tasked with assigning physical mechanisms to the observed magnetic field responses of a-Si:H.

4.1.1 Single-Particle Magnetic Field Effects

Single-particle effects are, almost without exception,[61] independent of the spin of the charge carrier involved. The first single-particle MFE that was historically discovered was the Hall effect, where the classical action of the Lorentz force on a moving charge carrier deflects its path and changes the bulk conductivity tensor. Within the limitations of the Drude model, we can derive the conductivity tensor $\hat{\sigma}$ for a magnetic field B in the z direction and an electric field in the x direction, written in the basis (x, y, z):

$$\hat{\sigma} = \sigma_0 \begin{bmatrix} \frac{1}{1+(\mu B)^2} & \frac{-(\mu B)^2}{1+(\mu B)^2} & 0 \\ \frac{(\mu B)^2}{1+(\mu B)^2} & \frac{1}{1+(\mu B)^2} & 0 \\ 0 & 0 & 1 \end{bmatrix} \tag{4.2}$$

Here, the carrier mobility is μ, the magnetic field is B, and the DC conductivity at $B = 0$ is σ_0. For a material with multiple types of charge carriers (e.g., electrons and holes), the total conductivity tensor is simply the sum of the conductivity for each charge carrier. Note that the Hall effect does not depend on the intrinsic magnetic moment (spin) of the

charge carrier, but instead depends only on its mobility. It is also straightforward to confirm that an observed magneto-conductance, MC(B), by measuring the anisotropy of MC(B) with respect to B. The experiment can be performed in the Hall geometry and the ratio between the off-diagonal element σ_{xy} to the diagonal element σ_{xx} can be measured. If that ratio $\sigma_{xy}/\sigma_{xx} = (\mu B)^2$, then the Hall effect is responsible. This also forms the basis for a common technique for measuring the unknown mobilities of samples.

Other than the Hall effect, there exist other, more exotic single-particle effects on the transport properties of semiconductors. We focus only on semiconductors not only because we are interested in the specific material system a-Si:H, but because charge transport is ferromagnets is extremely complicated due to the effects of spin-orbit coupling and strong exchange interaction. In amorphous carbon films, weak localization[87] (a fundamentally quantum effect related to wavefunction self-interference), wavefunction shrinkage,[89] and grain boundary scattering[87] have been known to result in magneto-conductivity. These effects also do not depend on the spin of the charge carriers, and are likely to manifest in a-Si:H due to the similarities in the microscopic landscapes between amorphous silicon and carbon.

Physical observables that depend on single-particle effects are predominantly limited to transport measurements rather than optical measurements, because recombination is inherently a two-particle process (requiring one electron and one hole). However, that does not mean that single-particle effects do not manifest in optical measurements (e.g., photoluminescence), nor does it mean that transport measurements will exclusively measure single-particle magnetic field effects. To see why, we realize that recombination is a multistep process, where the first step necessarily involves two

carriers finding one another from wherever their starting locations are, whether those be electrodes injecting current into a device or photogenerated carriers that have dissociated from their geminate partners. The intensity of inherently multiparticle phenomena like photoluminescence therefore might be decreased (increased) if, due solely to single-particle magnetic field effects, the carriers take more (less) time to find one another because the mobility is reduced (increased). Through this second-order process, the magneto-photoluminescence (MPL) can in principle be affected by the Drude model, weak localization, etc. However, the magnitude of such an effect is generally extremely small due to the second-order nature of the indirect effect.

Similarly, transport measurements are affected by changes in recombination rates as well as the MFE on the carrier mobility. Consider the following toy model to see why: let us start with the paired rate equations for the concentration of electrons and holes in the presence of (optical) generation and both monomolecular and bimolecular recombination. n and p are the densities of electrons and holes, respectively, G is the carrier generation rate (proportional to the incident photon flux), A_n and A_p are the monomolecular recombination rate constants for electrons and holes, and B is the bimolecular recombination rate:

$$\frac{dn}{dt} = G - A_n n(t) - Bn(t)p(t) \tag{4.3}$$

$$\frac{dp}{dt} = G - A_p p(t) - Bn(t)p(t) \tag{4.4}$$

The steady-state solution assuming an intrinsic semiconductor ($n(t) = p(t)$) requires that the monomolecular recombination rates are equal ($A_n = A_p \equiv A$). The steady-states electron and holes concentrations are written:

$$\frac{dn}{dt} = \frac{dp}{dt} = 0 \rightarrow n_{ss} = p_{ss} = \frac{-A+\sqrt{A^2+4BG}}{2B} \quad (4.5)$$

Note that the steady state carrier densities are related not only to the generation rate G, but also to the recombination rate constants A and B. The Drude-like DC conductivity is:

$$\sigma_0 = \frac{ne^2\tau_s}{m_e^*} + \frac{pe^2\tau_p}{m_p^*} \quad (4.6)$$

where τ_s and τ_p are the momentum relaxation times for electrons and holes respectively, while m_e^* and m_p^* are the electron and hole effective masses. Even by this simple Drude-like toy model, it is clear that a B-induced change in the recombination probabilities (A and B) will affect the conductivity σ_0 indirectly by changing the steady state carrier densities. For this reason, we must be careful when assigning MFE mechanisms based on transport or on optical measurements alone, but instead we must measure both and make a thoughtful comparison in order to shed light on the underlying B-dependent mechanisms.

4.1.2 Two-Particle Magnetic Field Effects

The majority of magnetic field effects in amorphous/organic semiconductors fall under the umbrella of spin-dependent two-particle mechanisms.[104] As discussed in detail in the introduction (Section 1.3), the basis for this fact lies in the fact that disorder in the microscopic structure of amorphous systems results in localization of energy eigenstates. That localization implies large coulomb interaction strengths between nearby charge carriers due to the reduced screening, large binding energy of excitons or bound electron-hole pairs, and large exchange interaction strength. The exchange interaction in particular

leads to strongly spin-dependent recombination and dissociation probabilities that depend on the mutual spin orientation between the bound electron and hole. For two spin-1/2 carriers, the "singlet" state ($|S, m_s> = |0,0>$) is many orders of magnitude more likely to undergo radiative recombination compared to the three "triplet" states ($|S, m_s> = |1,-1>, |1,0>, |1,1>$) due to conservation of angular momentum. To this effect, two-particle MFE mechanisms generally result in B-dependent intersystem crossing (ISC) between the singlet and triplet manifolds, which results in B-dependent time-averaged recombination and dissociation rates.

The quantum mechanical combined singlet/triplet basis is only valid if the interaction between spins is sufficiently large that the combined spin $S = s_1 + s_2$ can be treated as a good quantum number. Several experimental verifications of this fact have been published in the literature. First, Rabi oscillations[63] can be performed in EPR experiments that directly measure the spin of the object being probed. Indeed, something with spin equal to 1 is measured in Rabi oscillation measurements, which is interpreted as the triplet state of a strongly exchange-coupled e-h pair. In addition, photo-induced absorption detected magnetic resonance (PADMR)[70] has observed a "g=4" line at half the magnetic field value from the g=2 magnetic resonance. This is also interpreted as two spin-1/2 carriers (each with g-factor close to 2) whose spins are interacting strongly enough to behave like a single triplet exciton with S=1. The same situation is well-known in organics, there the strongly excitonic nature of bound polaron-pairs leads to exchange interaction energies of more than 100meV, providing excellent justification to use the combined singlet/triplet basis.

Two distinct mechanisms for ISC will be discussed in detail here, namely the

"delta-g" mechanism[105] and the "hyperfine spin mixing"[104,106] mechanism. Those two mechanisms are found to be sufficient to explain nearly all of the magnetic field effects in a-Si:H (with the exception of some very large-field effect which will be discussed toward the end of this Chapter). The field of organic semiconductors is extremely familiar with spin-dependent two-particle MFE mechanisms,[104] and the theoretical treatment is primarily borrowed from the literature relating to amorphous semiconducting polymers and small molecules, which are very similar in their microscopic landscapes to amorphous silicon.[72]

The "delta-g" mechanism is deeply connected with the concept the Lande g-factor, which can be understood as part of the conversion factor between the angular momentum of an electron with both spin and orbital angular momentum and its magnetic moment, given by $\mu = \frac{ge}{2m}J$, where $J = S + L$ is the total angular momentum. A free electron in a vacuum (with no orbital quantum number L) is characterized by a g-factor of approximately 2.003, where the small deviation from exactly $g = 2$ comes from corrections from quantum electrodynamics. In an atom, molecule, or semiconductor, the electron is also characterized by an orbital quantum number L and a magnetic dipole moment associated with that orbital motion, which adds to the magnetic moment from the intrinsic spin angular momentum. In the absence of strong spin-orbit coupling (SOC), the electron spin S is a good quantum number and the effective g-factor is close to that of a free electron. Amorphous silicon is composed of very light elements (predominantly Si^{28} and H^{1}) that lack strong SOC, which scales roughly proportionally to the atomic number Z^4, so we would expect the g-factor to be approximately 2. In fact, magnetic resonance experiments have identified the g-factor of electrons in conduction band tail states at $g =$

2.012 and valence band tail states of 2.004, yielding a difference broadly distributed around $\Delta g \approx 0.008$.[58] The small Δg (relative to semiconductors with large SOC where Δg can exceed 2) is expected from the small SOC in a-Si:H.

The otherwise degenerate spin eigenstates (spin "up" and spin "down") in an isolated electron or hole in a magnetic field B will be split in energy by the Zeeman interaction with an energy difference $\Delta E = g\mu_B B/\hbar$. Classically, we can picture the spin precessing due to the torque on the dipole moment with a frequency known as the Larmour frequency $\omega = g\mu_B B$. The splitting in g-factors Δg for a bound electron-hole pair lead to a splitting in the associated Zeeman frequencies of the separate electron and hole $\Delta\omega = (\Delta g)\mu_B B$. This causes the e-h pair to oscillate between the S and T_0 manifolds with the frequency $\Delta\omega$. Because the probability for the e-h pair to recombine or dissociate is strongly dependent on the spin manifold (singlet or triplet) in which it resides, the resulting time-averaged rates are dependent on the magnetic field. The lineshape of the MX(B) curve is Lorentzian with a width that, remarkably, depends only on Δg and the average e-h pair interaction time τ. The MX(B) function may be written:

$$MX(B) = \frac{A}{1+\left(\frac{2\,\mu_B\,\Delta g\,\tau\,B}{\hbar}\right)^2} \tag{4.7}$$

The dependence on the e-h pair lifetime τ allows for a useful probe to determine whether the Δg is actually the mechanism underlying an observed MFE, since τ can be changed with temperature or by adding/removing defects (e.g., by annealing the sample). Like many MFE mechanisms, the resulting lineshape is Lorentzian, but in a real amorphous material, there is a *distribution* of lifetimes $f_1(\tau)$ and a *distribution* of g-factor differences $f_2(\Delta g)$, so the resulting MFE lineshape will be broadened into a distorted Lorentzian.

The other MFE mechanism that is found to be relevant to a-Si:H is the hyperfine spin mixing mechanism. In atomic physics, the hyperfine interaction is the name given to the term in the Hamiltonian that couples the electron magnetic moment (of both orbital L and spin S origin) to the nuclear magnetic moment I. In order to have the hyperfine effect manifest in a system, the nuclear spin must be nonzero. Most naturally occurring silicon (95%) is either the isotope Si^{28} (92%) or Si^{30} (3%) which both have $I = 0$, and therefore are not capable of generating spin mixing through the hyperfine interaction. However, 5% of naturally occurring silicon is of the isotope Si^{29}, which has $I = 1/2$ and demonstrates hyperfine coupling. In addition, in hydrogenated amorphous silicon, roughly 10% (atomic fraction) is composed of hydrogen, which also has $I = 1/2$. The interaction between spin-1/2 charge carriers and the random effective magnetic field created by these Si^{29} and H^1 nuclei may result in spin mixing between the S and T_0 manifolds of the e-h pairs.

The hyperfine[104,106] spin mixing process can be visualized in the following way: a localized electron or hole in the a-Si:H lattice with a reasonable localization radius of ~3nm overlaps with somewhere between 10 and 100 nuclei with nonzero magnetic moments. The term in the Hamiltonian representing the energy of those interactions has the form:

$$H_{hf} = \sum_i a_i \vec{S} \circ \vec{I_i} \tag{4.8}$$

where $\vec{S}$ is the electron spin, $\vec{I_i}$ is the nuclear spin of the ith nucleus that the electron interacts with. The coefficient a_i is the hyperfine coupling strength between the spin-1/2 carrier and the ith nucleus, whose magnitude depends on the average carrier-nucleus separation (magnetic dipole-dipole interaction) and also the Fermi contact integral which

is proportional to the squared modulus $|\psi(r_i)|^2$ of the carrier wavefunction at the site of the nucleus r_i. For this reason, the localization radius of the carrier wavefunction determines the hyperfine coupling strength with nuclei in its immediate environment. The hyperfine spin-mixing mechanism is allowed because the electron and hole spins, S_e and S_h, do not overlap exactly in space but instead occupy different local environments dictated by different ensembles of nuclear spins. The effective magnetic field due to the hyperfine interaction with randomly oriented nuclear on each spin may be considered B_e and B_h respectively. The effective magnetic fields are considered isotropic (due to the negligible polarization of nuclear spins at any reasonably accessible temperature and magnetic field) and Gaussian, with mean squares:

$$< B_{eff}^2 > = \sum_i I_i(1 + I_i)a_i^2 \tag{4.9}$$

The spin-mixing then occurs by two distinct channels. First, a carrier undergoing hopping transport between localized states with different random hyperfine fields can be considered to be immersed in a stochastic time-dependent magnetic field.[106] The carrier spin will precess around each random magnetic field B_{eff} at its Larmour frequency $\omega = g\mu_B B_{eff}$ at each site until it hops again. Second, each of the two carriers in a closely-bound, exchange-coupled e-h pair will be exposed to different local environments due to imperfect wavefunction overlap, and the e-h pair will stochastically switch between the singlet and triplet pair manifold as each pair precesses around its local hyperfine field. However, if an external magnetic field is applied to the e-h pair whose magnitude is far larger than the random hyperfine field, the quantization/precession axis changes to that of the large external field and the hyperfine spin mixing processes is turned off. Therefore we would expect that the MFE resulting from hyperfine spin mixing will saturate when

the external magnetic field on the order of the hyperfine field, which can be estimated from linewidth splitting/broadening in magnetic resonance experiments.

The hyperfine spin mixing mechanism is well-known in the field of organic electronics,[104] where the small localization radius of polaronic charge carriers and the high density of nuclei with nonzero spin (mainly H^1) result in consistent hyperfine-related magnetic field effects. The characteristic linewidth of this type of MFE in organics is surprisingly independent of the exact molecular/chemical structure of the compound and it found to be in the range of 5-10mT. The hyperfine coupling constants determined by magnetic resonance experiments for the same materials generally predict smaller hyperfine fields, on the order of 2mT. It is surprising at first that the linewidth of the hyperfine-induced MFE is much larger than the effective hyperfine field B_{hf}, but it is generally agreed that this is the result of extra spin mixing originating from a multiple-hopping process before exchange-coupled e-h pair (or exciton) formation occurs.[72]

Another two-particle MFE process that is known to occur in organic semiconductors is dubbed the bipolaron model. This occurs when two charge carriers of like charge find it energetically favorable to occupy the same site in the organic lattice due to the strong polaronic effect. In other words, the deformation of the local environment because of Coulomb interaction between the charge carrier and the surrounding molecular structure creates an “energy well” for a second carrier. If that well is sufficiently deep, it can overcome the Coulomb repulsion between the two carriers, resulting is a doubly charged localized state. This state, being composed of two spin-1/2 carriers, also can be described by the quantum description consisting of a single total spin quantum number which may be in either the singlet or triplet manifold, and results in

spin-dependent (and magnetic field dependent) dissociation rates. However, the silicon-based lattice in a-Si:H is very “stiff” compared to the can der Waals forces that act between, for example, adjacent organic polymer chains in an polymer based semiconductor. The stiff covalent bonds of the silicon lattice do not distort strongly in the presence of a charged localized state, and therefore are not well described by polaron-like carriers. Since the polaronic “energy well” is small compared to the regular Coulomb repulsion between carriers of like charge, the bipolaron model is not thought to be relevant to amorphous silicon.[82]

4.1.3 Many-Particle Magnetic Field Effects

There are several MFE mechanisms in the literature of organic electronics that require three or more charge carriers, including triplet-triplet annihilation and trion (the three-particle state composed of an exciton and an extra charge carrier) formation. These mechanisms require very high concentrations of carriers and correspondingly small monomolecular and/or bimolecular recombination rates, as discussed above is Section 4.1.2. Because the nonradiative (monomolecular) recombination rate is so fast in amorphous silicon, the carrier concentration never reaches a threshold where many-particle effects become influential. This rate can be inferred either from the very low photoluminescence quantum efficiency (<1% at 10K) or by direct PL lifetime measurements, which show nearly complete decay of the PL within 1ns. For this reason, we can safely disregard MFE mechanisms that require three or more particles to function in a-Si:H.

4.2 Magneto-Photoconductivity

Photoconductivity (PC) in a-Si:H is best observed at or near room temperature due to the thermally activated variable range hopping (VRH) process that underlies charge transport[51,74]. The probability of hopping from a site with energy E_i to a site with energy E_f depends exponentially on the energy difference $\Delta E \equiv E_f - E_i$ as well as the thermal energy $k_B T$. The hopping rate, γ, may be written as

$$\gamma \propto \exp\left(\frac{\Delta r}{r_i} - \frac{\Delta E}{k_B T}\right) \tag{4.10}$$

where Δr is the separation distance between the two localized states involved, and r_i is the localization radius. In other words, in amorphous systems, the localized states are randomly distributed in both space and energy[74]. If the rate-limiting factor is not the spatial proximity of available states to tunnel into but instead the energy separation between nearby states ΔE, then the VRH formula should apply. For this reason, the PC is not observable below about 120K in our measurements – of course it is not a coincidence that photoluminescence (PL) appears only below about 120K. Figure 4.1 shows the typical device structure that was used to for PC measurements. Figure 4.2 shows a typical temperature dependence of the photoluminescence and photoconductivity in an a-Si:H device.

To achieve the field range (20 T) and resolution (<0.1mT at low fields) shown in this work, the experiments were conducted in three separate magnets with maximum fields of 0.24T, 7T, and 25T. The experimental details about these three magnets are found in Section 2.3. The same 40mW 486nm (above gap) laser excitation was used for all three experiments. In MPC, we observe three distinct magnetic field effects spanning the entire range from 1mT to more than 10Tm plotted in log scale in Figure 4.3.

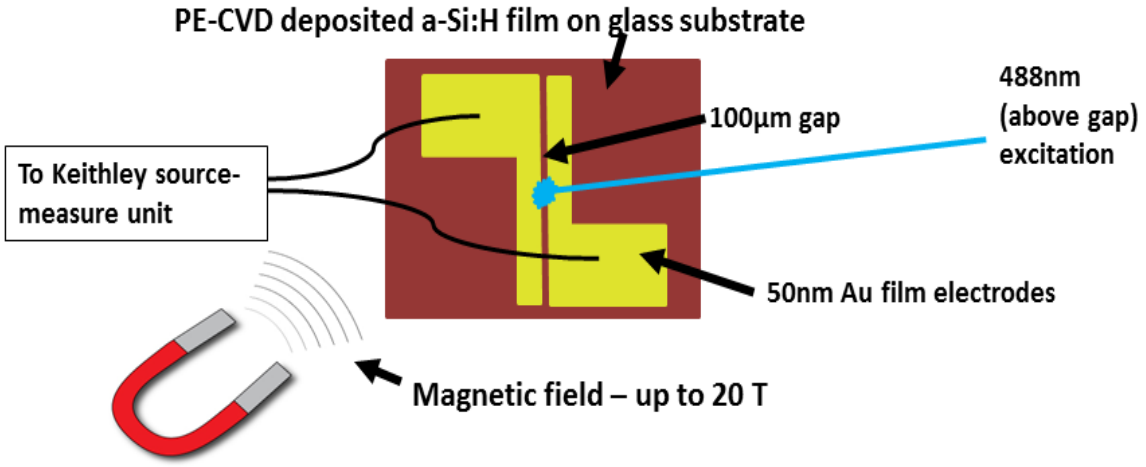

Figure 4.1. Device structure used to measure MPC in a-Si:H films. Connections to the gold electrodes were made by indium soldering. The directional dependence of the magnetic field was measured in both the $B \,||\, E$ and the $B \perp E$ geometry, and the resulting MFE was found to be unchanged

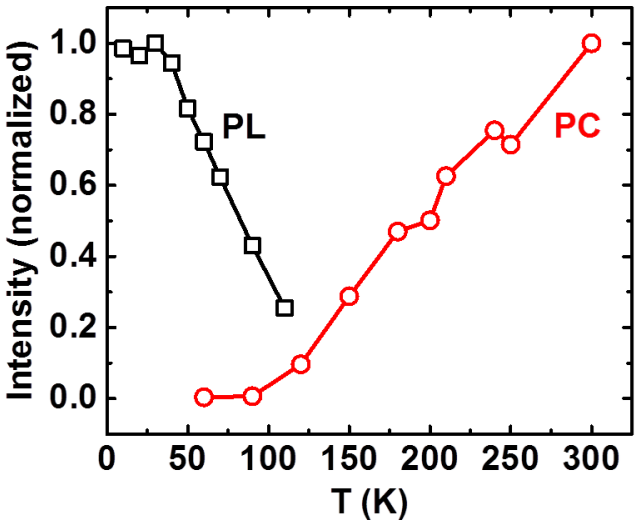

Figure 4.2. Temperature dependence of photoluminescence (PL) and photoconductivity (PC). Because PC relies on thermally-activated hopping between localized sites, it diminishes rapidly above room temperature. Likewise, PL is nearly undetectable above 120K because carriers can diffuse more easily at higher temperatures, eventually recombining nonradiatively through a low-energy defect or trap state.

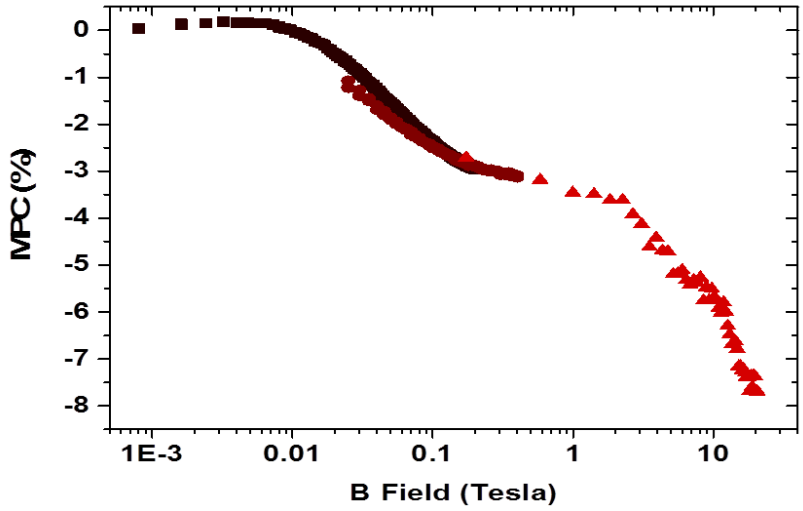

Figure 4.3. The entirety of the observed MPC effects plotted on a log scale.

For ease of discussion, let us start by labelling the three MPC features. The narrowest feature (~1mT width, Figure 4.4 (a)) will be referred to as the "small" feature, while the next narrowest (~100mT, Figure 4.4 (b)) will be referred to as the "large" feature. The feature shown in Figure 4.4 (c) that does not saturate by 20T will be referred to as the "ultra large" MFE. We will first identify the small MFE feature.

From magnetic resonance studies in a-Si:H, it is known that the hyperfine coupling constants (or equivalent hyperfine fields) have magnitudes that vary depending on the local environment and wavefunction localization of the carrier. Depending on the magnetic resonance technique employed, one can measure different subsets of the total electron population in an a-Si:H sample. Inductively detected ESR[77], for example, can be used to probe the unpaired electrons in dangling bond configurations. One finds that the effective hyperfine field of a dangling bond electron has a magnitude of about 2.5mT, counting the isotropic (Fermi contact) contribution and averaging over the anisotropic (dipole-dipole) contribution. Carriers that undergo radiative recombination (yielding detectable PL) can be studied by optically detected magnetic resonance (ODMR) which yields a hyperfine coupling strength of about 7mT[85,86,91].

Higher energy carriers, with energies near or above the mobility edge, can be selectively probed using electrically detected magnetic resonance (EDMR) or photoconductivity detected magnetic resonance (PCDMR). Because the carrier wavefunction extent is expected to rise monotonically with increasing carrier energy, the effective hyperfine fields are expected to be much smaller owing to the larger number of nuclear spin that are being "averaged over" by the larger carrier wavefunction. Those techniques generally have trouble resolving the small hyperfine splitting of the EDMR resonances due to the inhomogeneous broadening of all

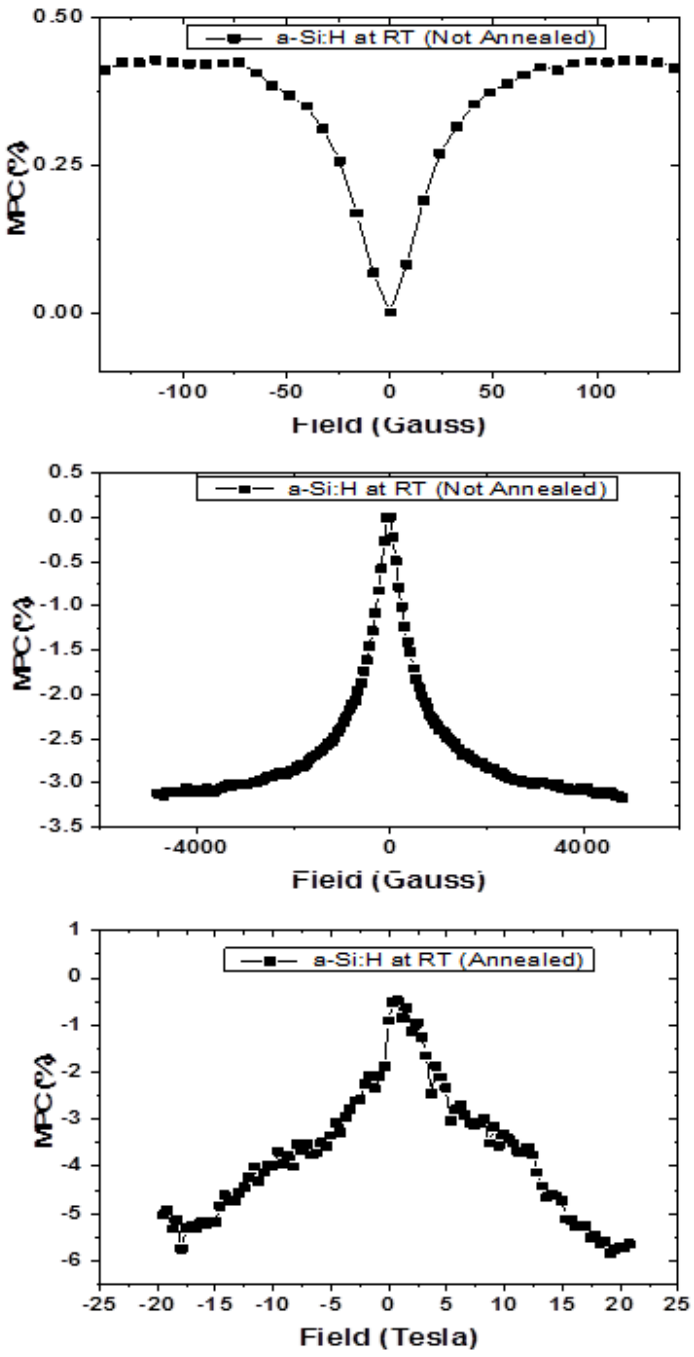

Figure 4.4. Three distinct MPC effects plotted in linear scale. We will refer to them as "small," "medium," and "large" MPC effects for ease of discussion.

resonances in amorphous materials such as a-Si:H, but estimates of the hyperfine coupling strength vary from 0.1-1mT.

Our MPC results show a small MFE with a linewidth of 1.8 (±0.2) mT at room temperature. The thermalization of hot carriers into the band tails and subsequent nonradiative recombination is known to be mediated by dangling bonds, so it seems reasonable to assume that the spin-dependent interaction between mobile carriers and dangling bonds is responsible for the observed small MFE. Our samples were initially grown with very high quality and a correspondingly low density of dangling bonds, but the well-known creation of dangling bonds by light illumination (known as the Staebler–Wronski effect)[107] means that the samples, after hours of intense laser illumination, may have a fairly high density of dangling bonds. These dangling bonds are known to be reversible by annealing, so we followed a recipe found in the literature and annealed half of a previously measured a-Si:H film (the other half was left unannealed) for one hour at 120°C. The observed reduction in the small MPC amplitude, shown in Figure 4.5, is consistent with our expectation that the underlying mechanism relies on nonradiative recombination of mobile carriers mediated by dangling bonds.

The next MPC feature in size is dubbed the large MFE and has a linewidth that is approximately 65 (±13) mT. We assign this to the delta-g mechanism owing to spin-dependent recombination between carriers in the conduction band tail (BT) and valence BT states. The g-factors of carriers in BT states can be directly probed by EDMR studies, and is known to be broadly distributed around 2.012 for the conduction band tail and 2.004 for the valence band tail. The resulting $\Delta g \approx 0.008$[58], along with the linewidth B_0 of the MFE, allows us to make use of the known relationship [105] between Δg, B_0, and

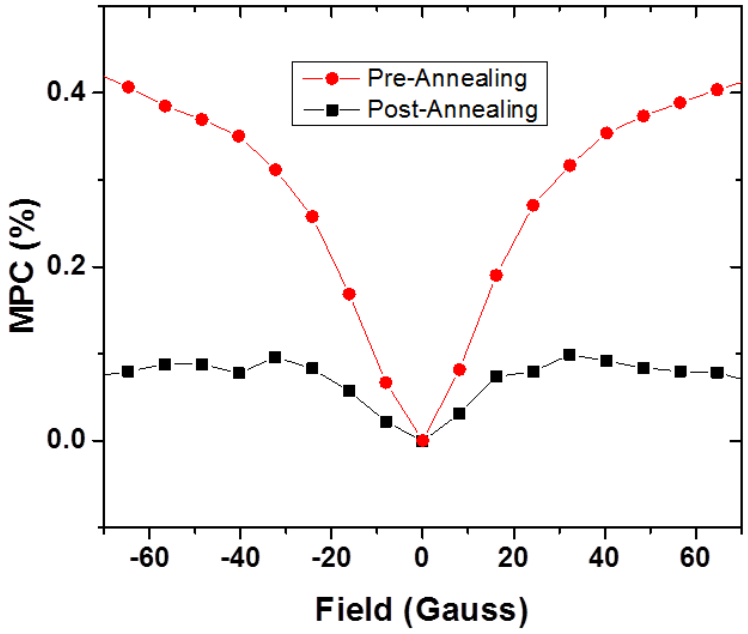

Figure 4.5. Small MPC effect before and after annealing at 120°C for one hour under high vacuum ($< 10^{-6}$ Torr). The linewidth is unchanged from 1.8mT (within experimental error) but the amplitude is reduced after annealing, reflecting the lower density of dangling bond defects.

the carrier pair lifetime τ:

$$B_0 = \hbar \,/\, (2\,\mu_B\,\Delta g\,\tau) \tag{4.11}$$

Through this relationship, we extract an interaction time $\tau \approx 10ns$. This turns out to be a reasonable estimate for the time that a charge carrier undergoing VHR-type transport will sit on an individual site before hopping to another localized state.[72] To complete this picture, we imagine that one localized electron in the conduction BT is close enough in space to a localized hole in the valence BT that there is a nonzero probability for the pair to recombine. That recombination rate will be dependent on the total spin of the e-h pair (singlet or triplet). However, if the recombination does not proceed quickly enough, one of the carriers can hop away to another site and continue to participate in electrical conduction. Through this process, the delta-g spin-mixing mechanism will result in an observable MPC. Because recombination occurs either through band-to-band transitions (whose magnetic field dependence is described by the delta-g mechanism) or mediated through dangling bonds (whose magnetic field dependence is described by hyperfine interaction between charge carriers and dangling bonds), we expect some competition[59] between the two recombination rates. In other words, if one pathway is reduced (e.g., by annealing the sample and decreasing the DB density), then the other would reasonably be expected to increase. If the relative rate of one pathway increases, then the amplitude of its associated MFE should increase. We can then test our assignment by annealing the sample and measuring the large MFE again. After annealing, the ratio between the two recombination pathways is adjusted in favor of band-to-band transitions and the ratio of (delta-g MFE amplitude)/(hyperfine MFE amplitude) is increased (shown in Figure 4.6). This supports our assignment of the two MFE to two competing recombination pathways,

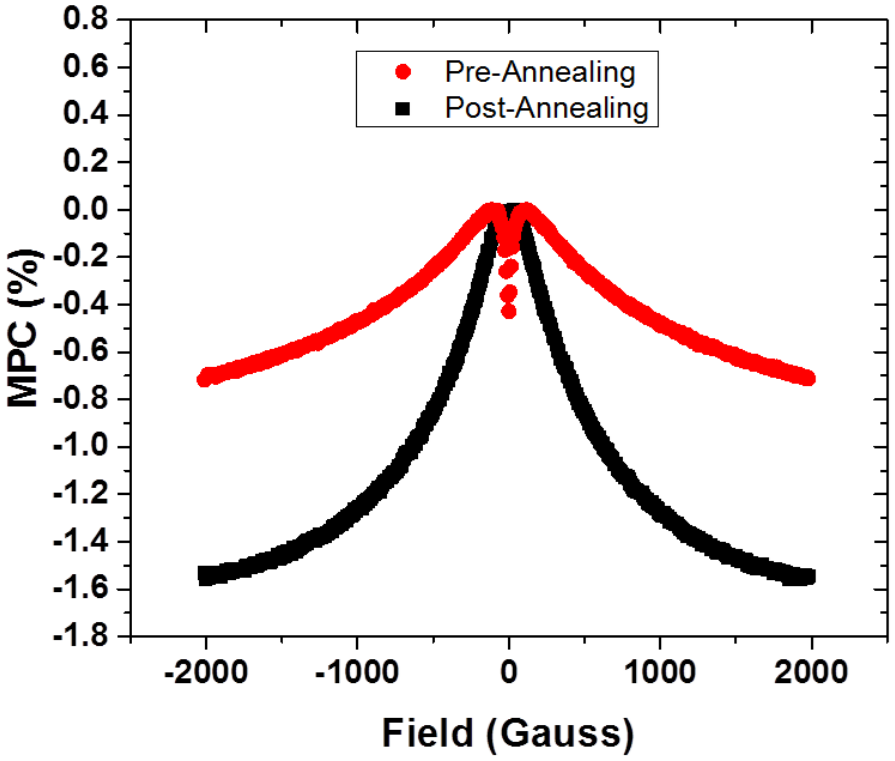

Figure 4.6. MPC up to 2kG before and after annealing. Note the drastic decrease in the amplitude of the small (hyperfine) MFE and the enhancement of the amplitude of the large (delta-g) MFE. This clearly illustrates the competition between the two recombination pathways (DB assisted for hyperfine mechanism, or band-to-band for delta-g mechanism) and the relative change after annealing.

with the added bonus of allowing us to measure the on-site time ($\tau \approx 10ns$) that a carrier spends in one localized state before hopping to another. Note that this time does not drastically after annealing, where $\tau_{unannealed} \approx 10ns$ and $\tau_{annealed} \approx 13ns$.

The large MFE, now known to originate from the delta-g mechanism,[105] was also studied as a function of temperature, laser excitation intensity, and electric field. Those experiments are summarized in Figure 4.7. The important findings of those measurements are that the MFE linewidth associated with the delta-g mechanism (and the resulting e-h pair lifetime τ) are not dramatically affected by the excitation power or the applied electric field. If it were observed that the MPC amplitude or linewidth had a dependence on the excitation intensity, it would imply that multiparticle processes are taking place, which luckily is not the case here. In fact, the amplitude of MPC saturates at roughly 1mW and stays at ~2% up to at least 25mW (Figure 4.7).

At very large magnetic fields, an "ultra large" MFE is observed in the MPC that does not saturate up to 20T (Figure 4.4 (c)). In the literature of magnetic field effects in amorphous systems, it is found that there are many mechanisms may be responsible for such a large feature, including the classical Drude model, weak localization[87] or anti-localization, and grain boundary scattering[87]. These mechanisms can, in principle, be experimentally separated by their functional dependence on temperature, magnetic field direction, sample quality (i.e., annealing), and illumination energy and intensity. Unfortunately, due to our limited time of access to such a large magnet at the National High Magnetic Field Laboratory, such experiments will have to wait. Our current body of experimental work is not sufficient to conclusively identify a mechanism underlying the ultra-large magnetic field effect.

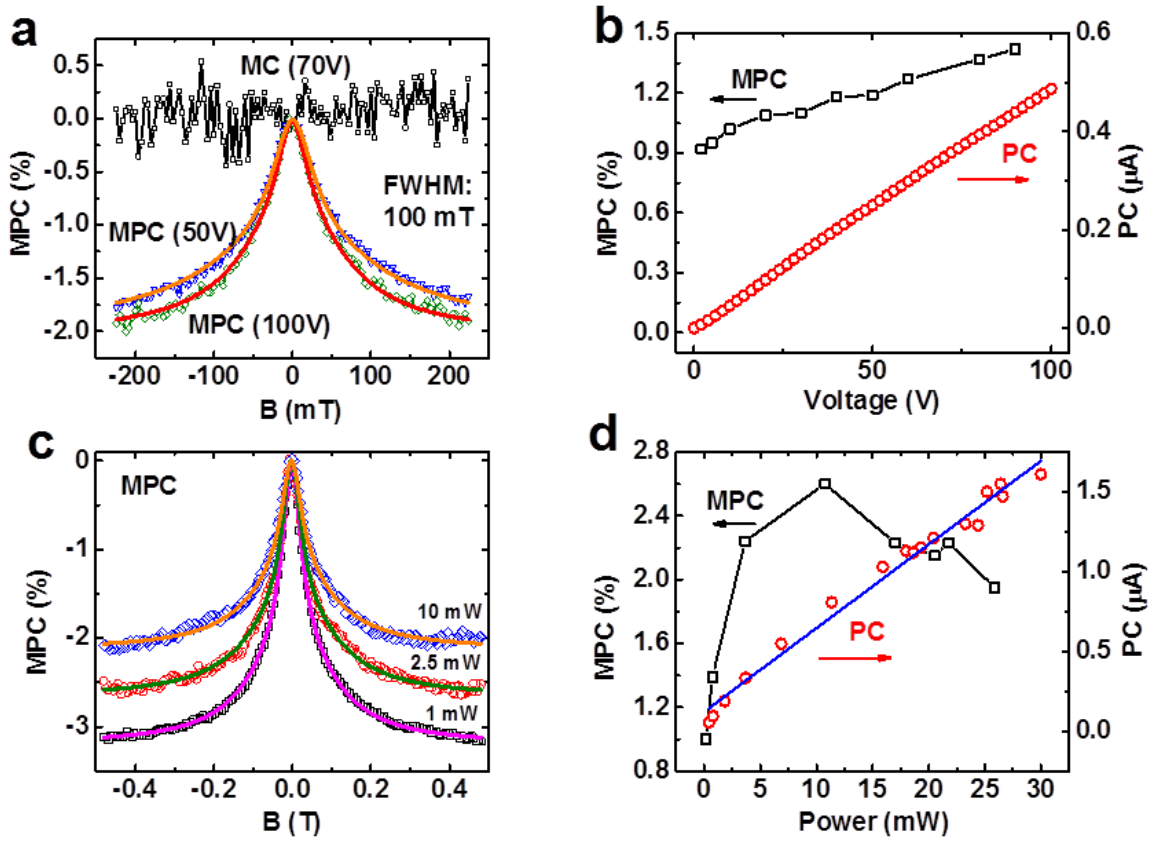

Figure 4.7. (a) comparison between magneto-conductivity (MC) and magneto-photoconductivity (MPC) demonstrating that the higher energy photoexcited carriers are necessary to observe the magnetic field effect. The applied voltage does not affect the MFE noticeably. (b) PC and MPC versus applied voltage. PC is approximately linear, as expected, but the MPC shows little voltage dependence. (c) Power dependence on the lineshape of MPC. (d) MPC and PC versus incident optical power. PC is approximately linear with incident power, while MPC saturates at low power (~1mW) and decreases slightly at higher power, likely due to heating effects.

4.3 Magneto-Photoluminescence

The spectrum and dynamics of the photoluminescence of a-Si:H, even without investigating magnetic field effects, is extremely interesting. The spectrum is characterized by two broad emission peaks, consisting of a high-energy PL band centered at ~1.4 eV, and another low-energy band centered at ~0.8eV.[76,77] The lower energy band originates from deep trap states in the band tails and has as extremely long lifetime in excess of 1ms.[55] Since the dynamics of the low-energy band are dominated by self-trapping and tunneling behavior of localized carriers deep in the band tails and defect states,[76] we do not expect a large or accessible magnetic field effect to manifest there. For example, if the delta-g mechanism was influential in the spin-dependent recombination process of carriers who remain in deep trap states for 1ms, the expected linewidth of the resulting MFE would be on the order of 1μT. This is far below our experimental resolution. Even for other MFE mechanisms that do not rely on the e-h pair lifetime, a radiative lifetime of 1ms is many orders above the relevant spin-spin (T_1) or spin-lattice (T_2) relaxation times, so coherent spin-mixing is not important on such long time scales. Therefore we will focus on the higher-energy band (which has the added bonus of being accessible to high-sensitivity silicon-based CCD spectrometers) which has a fast radiative lifetime below 1ns.

The large linewidth (~0.4eV) of the PL and redshift (~0.5eV) from the absorption edge (shown in Figure 4.8) is indicative of the width of the band tails, which decay exponentially into the gap with a characteristic energy decay length which can be estimated as 0.2-0.3eV.

When the a-Si:H sample is cooled to 7K (so that PL can be observed) and placed

in a magnetic field, two features emerge in the magneto-photoluminescence spectrum, which are labelled the "small" feature and the "large" feature for ease of discussion (Figure 4.9). The assignment of underlying physical mechanisms to each feature will be done after the features are investigated further.

The large PL linewidth also allows us a useful experimental tool to probe radiative transitions between trapped e-h pairs as a function of their energy. This is useful because recombination lifetimes, e-h pair exchange integrals, localization lengths, and other physically meaningful quantities are expected to be energy-dependent since the wavefunction localization length increases monotonically as the electron or hole energy approaches its respective mobility edge. We will somewhat arbitrarily define four "Sections" of the total PL spectrum, labelled PL1 through PL4, whose energy windows are defined in Figure 4.10. This will allow us to measure the behavior (temperature dependence, magnetic field dependence, etc.) of recombining e-h pairs as a function of their energy, which should allow us to extract useful information about the microscope physics of the system.

We will first discuss the small MPL feature, which we assign to the hyperfine interaction between localized carrier wavefunctions and the surrounding Si^{29} and H^{1} nuclei. The hyperfine interaction strength a_i is a function of the wavefunction localization radius due to the Fermi contact integral term (also called the isotropic hyperfine term), which can be written in a fairly compact equation that takes into account the magnetic dipole moment strength of the electron and the nucleus (and their relative orientation), as well as the amplitude of the electronic wavefunction at the location of the nucleus:

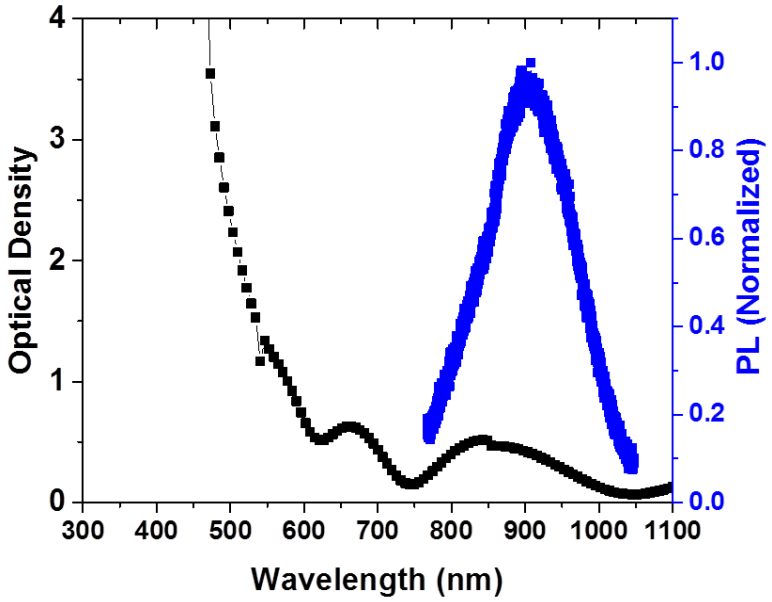

Figure 4.8. Optical absorption (taken at room temperature) and PL (taken at 10K) from a ~3μm thick a-Si:H film on glass. The large redshift of the PL compared to the absorption edge is due to fast (picosecond time scale) thermalization of hot carrier from the mobility edge to the band tails before recombination occurs.

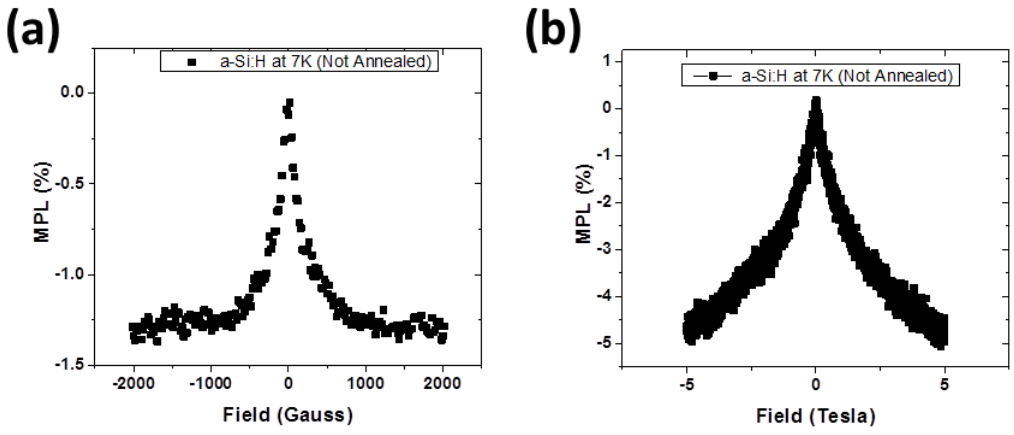

Figure 4.9. (a) The "small" MPL feature with a linewidth of ~10mT. (b) The "large" MPL feature with a linewidth of ~2T.

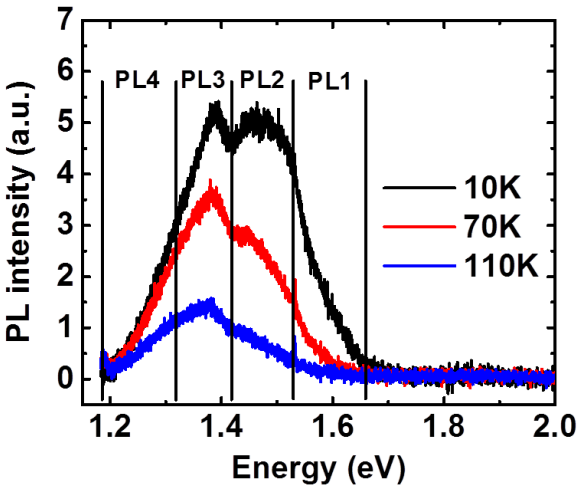

Figure 4.10. Photoluminescence spectrum of a-Si:H as a function of temperature. Note that the intensity decays greatly by 110K and the spectrum average redshifts. This redshift is due to the diffusion constant increasing with temperature, which allows carriers to diffuse to lower-energy localized states before undergoing radiative recombination.

$$A_i = -\frac{2}{3}\mu_0 < \mu_n \circ \mu_e > |\psi(r_i)|^2 \quad (4.12)$$

where μ_n and μ_e are the nuclear and electronic magnetic moments respectively, and $|\psi(0)|^2$ is the squared modulus of the electron wavefunction at the site of the nucleus. The effective hyperfine field is expected to be larger for low-energy, tightly localized carriers that undergo radiative recombination (and are detected as PL) compared to higher energy carriers that participate in hopping transport closer to the mobility edge.

The weak energy dependence (Figure 4.11) and the very non-Lorentzian lineshape of the small MPL feature are consistent with the expectation that hyperfine interactions between trapped carriers in BT states and surrounding nuclei are responsible for the effect. The ideally Lorentzian lineshape that can be derived from the hyperfine spin mixing model is broadened and distorted by inhomogenous disorder inside the material, resulting is the observed MPL function which can be well-fit by a sum of several Lorentzian functions. The interpretation is that the widely varied local environments or trapped electrons result in a distribution of hyperfine interactions strengths varied between ~3mT and ~25mT. Hyperfine constants on the order of 25mT have been observed in a-Si:H films with phosphorous dopants, but are surprisingly large to appear in (nominally) undoped films. It is unclear what local environments lead to such large hyperfine coupling strengths.

Next, we examine the large MPL feature, which we assign to the delta-g spin mixing mechanism. Unlike the hyperfine mechanism, the delta-g mechanism should be a relatively strong function of temperature and energy owing to the functional dependence of the delta-g linewidth on τ, the e-h pair interaction time[105]. Since the wavefunction localization radius decreases monotonically as the carrier energy approaches the center of

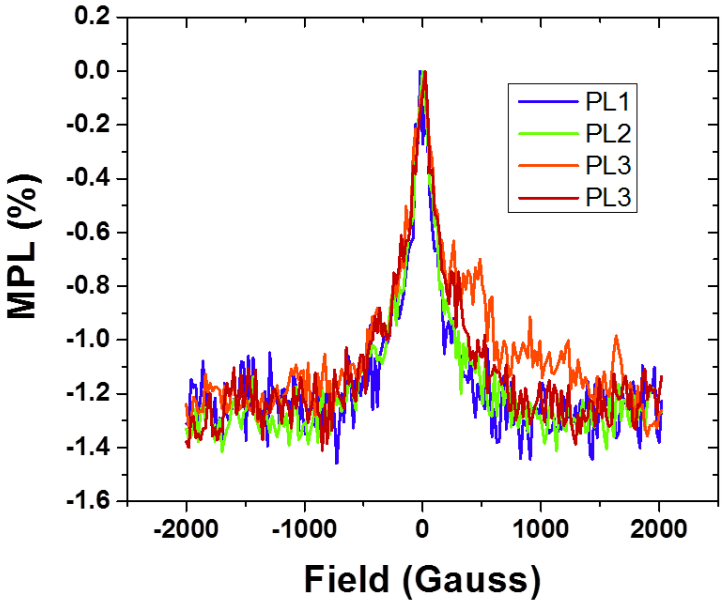

Figure 4.11. Energy-resolved MPL spectrum at 7K plotted up to 200mT. The linewidth of the small MPL feature (15±T) is not dependent on PL energy (within error bars). The MFE is highly non-Lorentzian due to inhomogeneous broadening from disorder in a-Si:H.

the gap, we would expect that at a fixed temperature, the lower-energy radiation (originating from recombination between pairs of carriers with average energy closer to mid-gap) might have a longer average τ because recombination is governed by tunneling between adjacent localized states. A smaller localization radius (assuming a nearly constant average separation between nearby states) should lead to a smaller tunneling probability and a longer pair lifetime τ. Indeed, when we resolve the linewidth of the MPL feature by PL energy, we see a non-constant linewidth with the expected energy dependence (Figure 4.12).

Again using the known relationship $B_0 = \hbar / (2\,\mu_B\,\Delta g\,\tau)$, we can extract the average carrier pair interaction lifetime τ as a function of energy, which is found to vary from 0.15ns (for higher energy PL) to 0.35ns (for lower energy PL). The energy-resolved interaction times are plotted in Figure 4.13. This is entirely consistent with time-resolved experimental works in the literature where the bulk of the PL is found to decay with a lifetime of less than 1ns.[90] It must be mentioned that much longer-lived PL lifetimes can be observed in time-resolved spectroscopy, which is not due to the intrinsic pair lifetime but instead to the process of dissociation of geminate e-h pairs, followed by a relatively long diffusion process before ultimately recombining with another carrier as a non-geminate pair.[82] The very long lifetime observed in those measurements[75] is representative of the longer hopping-based charge transport process, and it is therefore difficult to discern information about recombination dynamics as a result.

It is not surprising that the total integrated MPL appears highly non-Lorentzian due to the distribution in lifetimes, but even for a fixed PL energy (smaller window of e-h pair lifetimes), the MPL feature appears as a broadened Lorentzian. This is because

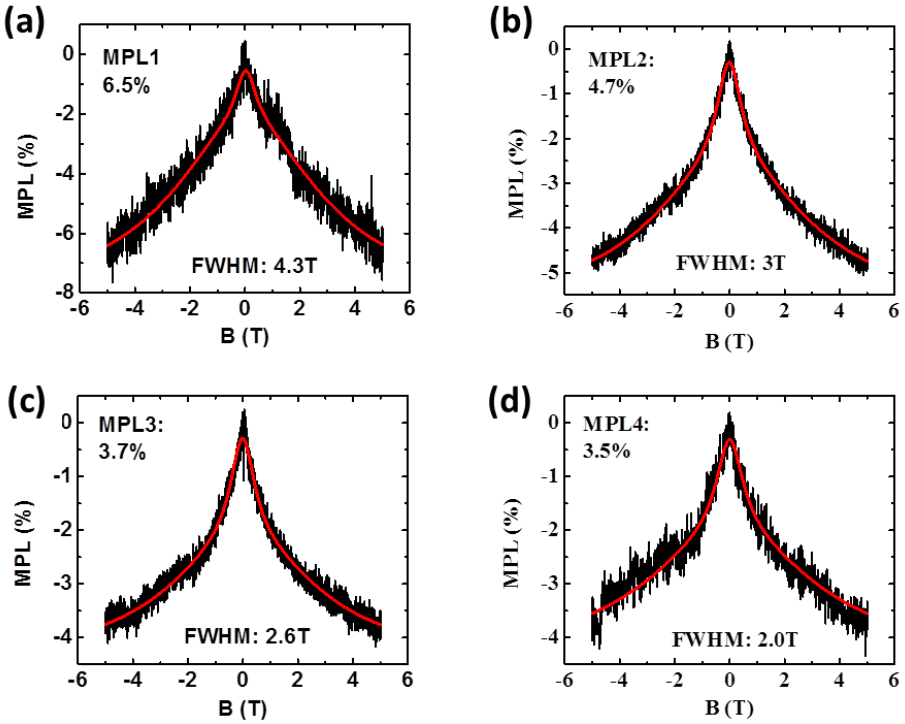

Figure 4.12. An energy-resolved look at the large MPL feature. The linewidth of the MFE, identified as the delta-g mechanism, increases with energy from 2.0T to 4.3T as the PL energy varies from 1.1eV to 1.6eV.

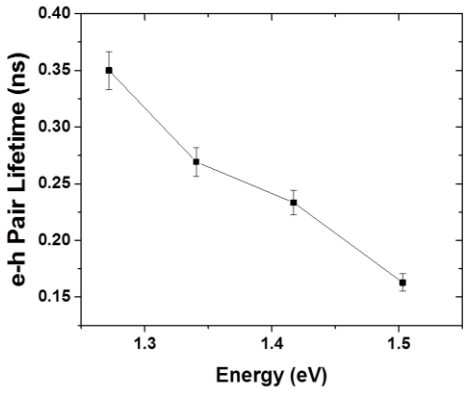

Figure 4.13. Average electron-hole pair lifetime, τ, as a function of PL energy. The lower (higher) energy states in the conduction (valence) band tail have a smaller localization radius, which leads to a longer lifetime for tunneling-based radiative recombination as well as lower energy PL.

the g-factors (and therefore Δg) for both electrons and holesare extremely anisotropic with respect to their local environments and shouldn't be described by a single g-factor but instead a g-tensor, which is averaged overall possible orientations as the sample has no preferred crystallographic orientation. In addition, each entry in the g-tensor has some distribution due to inhomogeneity in local bonding angles and distances – an effect known as g-strain. The broadening in g-factors leads to a corresponding uncertainty in the extracted e-h pair lifetimes (or more accurately, a broad distribution is actual lifetimes), which makes the actual error bars difficult to estimate accurately.

4.4 Conclusions and Future Directions

We have shown that the wide variety of magnetic field effects that manifest in amorphous silicon can be explained using only two underlying physical mechanisms, namely the hyperfine interaction between photogenerated charge carriers and the surrounding nuclei with nonzero magnetic moment, and the "delta-g" mechanism which fundamentally originates from spin-orbit coupling which changes the effective g-factors of electrons and holes and promotes intersystem crossing between spin states in the presence of a magnetic field[105]. There is just one unresolved mystery in the magneto-photocurrent of a-Si:H, and that is the "ultra-large" MFE that does not saturate up to 20T. We suspect that it originates from either Hall magnetoresistance or weak localization[87], but our existing body of experimental evidence is not sufficient to conclusively identify it due to the experimental difficulty and cost associated with experiments in extremely large magnetic fields. An interesting direction to pursue in this research field would be to explore the dependence of the ultra-large MFE on the angle between the magnetic and

electric fields – this should be sufficient to confirm or deny whether the observed effect is simple Hall effect (which should be an odd function of B when B⊥E) or weak localization.

Perhaps the most immediately interesting research direction to pursue would be to fabricate working, relatively high efficiency a-Si:H solar cells and see how our MPC results translate to a real device, whose internal structure is much more complicated. The devices that were fabricated for the electrical experiments undertaken in this Chapter were composed of a thin film of a-Si:H with gold electrodes deposited on top. It is conceivable that the observed MPC effects only exist at the interface[73] between the a-Si:H and the gold electrodes or has some critical dependence on metal interdiffusion into the amorphous material. Since the goal of this research was, in some sense, to understand the physics necessary to optimize real-world a-Si:H devices, it would likely be extremely rewarding to fabricate high-efficiency PV cells and see how well our understanding of the structure and physics of a-Si:H translate.

CHAPTER 5

CONCLUSIONS

5.1 New Insight on the Spin Seebeck Effect

By investigating the spin Seebeck effect (SSE) by optical methods instead of the conventional electrical methods, we have eliminated many of the key artefacts involved with the experiment and conclusively shown that the SSE does exist in to prototypical metallic ferromagnetic system, $Ni_{81}Fe_{19}$. In addition, we have observed a substrate dependence of the magnitude of the heat-induced spin accumulation (indicated the crucial role that phonon-magnon interaction plays in the SSE) and a never-before-seen SSE anisotropy when the magnetization is in-plane versus out-of-plane. The out-of-plane magnetization is not accessible to conventional electrically-detected schemes, so our optical detection scheme is in fact the only method for quantifying it.

Our novel experimental scheme for purely optical detection of the spin Seebeck effect has solved one outstanding question in the field of spin caloritronics, but in many ways the underlying dilemma still persists. That real dilemma is not simply the question, "Does the SSE exist in metallic ferromagnets," but instead asks how we can use the SSE to generate useful spin currents for the next generation of nanoscale electronic devices. Most researchers in the field were already convinced that the SSE did exist in metallic systems (the true magnitude of the effect was under debate), but the experimental tools to

detect and quantify it did not exist before our work. Now that we have established that the SSE exists in NiFe and we have some estimates about its magnitude, anisotropy, and microscopic origins, the outstanding question is to understand how we can take advantage of that knowledge toward useful engineering applications. To this end, our optical detection scheme is not the final step, since a functional next-generation machine (say a spintronic computer) might have a number of functional nanoscale spintronic elements on the order of 10^9, which is roughly the number of electrical transistors on a modern CPU. Eventually, the spintronics community will have to invent a robust, artefact-free electrical detection scheme because a spintronic computer cannot have 10^9 tiny Sagnac interferometers measuring the spin accumulation at each spin-transistor site. The next step for the field therefore necessarily includes optimizing the efficiency with which thermal spin currents are generated and perfecting inverse spin Hall effect (ISHE) detection schemes. To this end, it is unlikely that metallic ferromagnets such as NiFe will find widespread use in functional spintronics elements, simply because the thermal spin current generation efficiency is very small (owing to the small magnon mean free path as spin diffusion length) and the possibility for magneto-thermoelectric contamination of miniature signals is presently impossible to avoid.

Unless a drastic solution is found, magnetic insulators such as YIG will likely form the foundation of our next-generation spintronic devices. Since ISHE-based electrical schemes for detecting spin currents are fairly robust in YIG (since magneto-thermoelectric artefacts are ideally eliminated in magnetic insulators), one might wonder about the future of our optical detection scheme, and whether it is just a novelty with no future. To answer that question, I remind you that the ISHE voltage is strictly able to

measure spin currents only when the spin orientation is perpendicular to J_s. Our optical technique is not limited by any such geometrical considerations, and can be easily adapted to measure in-plane or out-of-plane spin currents where the magnetization vector is either in-plane or out-of-plane. This freedom opens a whole new dimension of research possibilities, which I believe will be key in thoroughly understanding the fundamental physics governing the spin Seebeck effect. This understanding will then allow the spin caloritronics community to optimize the magnitude of the effect so that it may have some hope of real-world engineering applications.

The magneto-optic Sagnac interferometer microscope at the University of Utah will be used for similar projects investigating the spin Seebeck effect, while another is being constructed in the lab of Dr. Dali Sun, who was my primary mentor during this project as the rest of my time as a graduate student. In Dr. Sun's lab, the spin Seebeck effect will be investigated in traditional magnetic insulators as well as non-traditional magnets, including organic ferromagnets. I wish them many years of continued success in their research efforts.

5.1 Implications of MFE Spectroscopy in Amorphous Silicon

We have shown that the relatively wide variety of magnetic field effects (MFEs) in both the photoluminescence and the photoconductivity of amorphous hydrogenated silicon (a-Si:H) may be explained by only two physical mechanisms. Those mechanisms are hyperfine-mediated spin mixing between spin manifold of exchange-coupled electron-hole pairs and the "delta-g mechanism" which results in oscillation between spin states in the presence of a magnetic field. The identification of these magnetic field

effects allows us to discern interesting information about charge generation and transport, including the average electron-hole pair interaction time before radiative recombination takes place (~0.1 to ~0.4 ns depending on carrier energy) and the average "on-site" hopping time before tunneling occurs between localized states during charge transport (~10ns).

From our results studying magnetic field effects in both "good" amorphous silicon (after annealing away many defects) and "bad" amorphous silicon (after many hours of light and air exposure[107]), we know that there is a competition between various recombination processes and that the signature magnetic field effects of each process is different. In other words, from the relative contribution of each mechanism (hyperfine-mediated MFE due to dangling bonds, delta-g MFE due to band tail recombination, etc.) to the total observed MFE, is should be possible to gain information about the relative rates of various recombination mechanisms. It should go without saying that this information is of great value to the field of a-Si:H photovoltaics, where the exact nature of charge transport and recombination is not perfectly understood. I particular, recent EPR-based studies have shown that dangling-bond traps are not just one type of defect, but rather two distinct categories of defects with different dynamics and different responses to annealing. A clear next step for our MFE spectroscopy might be to team up with an EPR experiment to see whether these different types of dangling-bond defects have different MFE responses. For example, it has been shown that a degraded sample can be partially annealed (at a lower temperature and shorter duration than the conventional recipe), and only one type of defect will remain. The existence of one species of defect can be confirmed by EPR, and the corresponding MFE on

photoluminescence or photoconductivity can be measured. Then the MFE might be measured on a real a-Si:H solar cell to see if one type of defect contributes more to the deterioration by the Staebler-Wronski effect[107] than the other. In this way, our understanding of MFE mechanisms may help the industry move forward by increasing the efficiency of a-Si:H solar cells or by inventing tools to solve the light-induced degradation process if we understand which defects really contribute to the degradation.

REFERENCES

[1] H. Ohno, Nat. Mater. **9**, 952 (2010).

[2] G. Bauer, E. Saitoh, and B. J. van Wees, Nat. Mater. **7**, 885 (2012).

[3] K. Uchida, S. Takahashi, K. Harii, J. Ieda, W. Koshibae, K. Ando, S. Maekawa, and E. Saitoh, Nature **455**, 778 (2008).

[4] K. Uchida, H. Adachi, T. An, T. Ota, M. Toda, B. Hillebrands, S. Maekawa, and E. Saitoh, Nat. Mater. 10, 737 (2011).

[5] S. Bosu, Y. Sakuraba, K. Uchida, K. Saito, T. Ota, E. Saitoh, and K. Takanashi, Phys. Rev. B **83**, 224401 (2011).

[6] C. M. Jaworski, J. Yang, S. Mack, D. D. Awschalom, J. P. Heremans, and R. C. Myers, Nat. Mater. **9**, 898 (2010).

[7] C. M. Jaworski, J. Yang, S. MacK, D. D. Awschalom, R. C. Myers, and J. P. Heremans, Phys. Rev. Lett. **106**, 186601 (2011).

[8] K. Uchida, J. Xiao, H. Adachi, J. Ohe, S. Takahashi, J. Ieda, T. Ota, Y. Kajiwara, H. Umezawa, H. Kawai, G. E. W. Bauer, S. Maekawa, and E. Saitoh, Nat. Mater. **9**, 894 (2010).

[9] K. Uchida, H. Adachi, T. Ota, H. Nakayama, S. Maekawa, and E. Saitoh. Appl. Phys. Lett. **97**, 172505 (2010).

[10] A. Kirihara, K. Uchida, Y. Kajiwara, M. Ishida, Y. Nakamura, T. Manako, E. Saitoh, and S. Yorozu, Nat. Mater. **11**, 686 (2012).

[11] T. Kikkawa, K. Uchida, Y. Shiomi, Z. Qiu, D. Hou, D. Tian, H. Nakayama, X. F. Jin, and E. Saitoh, Phys. Rev. Lett. **110**, 067207 (2013).

[12] K. Uchida, M. Ishida, T. Kikkawa, a Kirihara, T. Murakami, and E. Saitoh, J. Phys. Condens. Matter **26**, 343202 (2014).

[13] G. Siegel, M. C. Prestgard, S. Teng, and A. Tiwari, Sci. Rep. **4**, 4429 (2014).

[14] M. Agrawal, V. I. Vasyuchka, A. A. Serga, A. Kirihara, P. Pirro, T. Langner, M. B. Jungfleisch, a. V. Chumak, E. T. Papaioannou, and B. Hillebrands, Phys. Rev. B **89**, 224414 (2014).

[15] C. M. Jaworski, R. C. Myers, E. Johnston-Halperin, and J. P. Heremans, Nature **487**, 210 (2012).

[16] S. M. Wu, J. E. Pearson, and A. Bhattacharya, Phys. Rev. Lett. **114**, 186602 (2015).

[17] A. D. Avery, M. R. Pufall, and B. L. Zink, Phys. Rev. Lett. **109**, 196602 (2012).

[18] M. Schmid, S. Srichandan, D. Meier, T. Kuschel, J. M. Schmalhorst, M. Vogel, G. Reiss, C. Strunk, and C. H. Back, Phys. Rev. Lett. **111**, 187201 (2013).

[19] I. V. Soldatov, N. Panarina, C. Hess, L. Schultz, and R. Schäfer. Phys. Rev. B **90**, 104423 (2014).

[20] D. Meier, D. Reinhardt, M. Schmid, C. H. Back, J.-M. Schmalhorst, T. Kuschel, and G. Reiss. Phys. Rev. B **88**, 184425 (2013).

[21] D. Meier, D. Reinhardt, M. van Straaten, C. Klewe, M. Althammer, M. Schreier, S. T. B. Goennenwein, A. Gupta, M. Schmid, C. H. Back, J,-M. Schmalhorst, T. Kuschel, and G. Reiss, Nat. Commun. **6**, 8211 (2015).

[22] D. R. Birt, K. An, A. Weathers, L. Shi, M. Tsoi, and X. Li. Appl. Phys. Lett. **102**, 082401 (2013).

[23] M. Agrawal, V. I. Vasyuchka, A. A. Serga, A. D. Karenowska, G. A. Melkov, and B. Hillebrands. Phys. Rev. Lett. **111**, 107204 (2013).

[24] J. Xiao, G. E. W. Bauer, K. C. Uchida, E. Saitoh, and S. Maekawa, Phys. Rev. B **81**, 214418 (2010).

[25] H. Adachi, K. I. Uchida, E. Saitoh, J. I. Ohe, S. Takahashi, and S. Maekawa, Appl. Phys. Lett. **97**, 252506 (2010).

[26] H. Adachi, K. Uchida, E. Saitoh, and S. Maekawa. Rep. Prog. Phys. **76**, 036501 (2013).

[27] M. Schreier, A. Kamra, M. Weiler, J. Xiao, G. E. W. Bauer, R. Gross, and S. T. B. Goennenwein. Phys. Rev. B **88**, 094410 (2013).

[28] S. M. Rezende, R. L. Rodríguez-Suárez, R. O. Cunha, A. R. Rodrigues, F. L. A. Machado, G. A. Fonseca Guerra, J. C. Lopez Ortiz, and A. Azevedo, Phys. Rev. B **89**, 014416 (2014).

[29] Y. K. Kato, R. C. Myers, A. C. Gossard, and D. D. Awschalom, Science **306**, 1910 (2004).

[30] S. A. Crooker, M. Furis, X. Lou, C. Adelmann, D. L. Smith, C. J. Palmstrøm, P. A. Crowell. Science, **309**, 2191 (2005)

[31] G.-M. Choi and D. G. Cahill, Phys. Rev. B **90**, 214432, 1 (2014).

[32] P. N. Argyres, Phys. Rev. **97**, 334 (1955).

[33] A. Slachter, F. L. Bakker, J-P. Adam, and B. J. van Wees Nat. Phys. **6**, 879-882 (2010).

[34] G.-M. Choi, C.-H. Moon, B.-C. Min, K.-J. Lee, and D. G. Cahill. Nat. Phys. **11**, 576-581 (2015).

[35] J. Kimling, G.-M. Choi, J. T. Brangham, T. Matalla-Wagner, T. Huebner, T. Kuschel, F. Yang, and D. G. Cahill. arXiv: 1608.00702.

[36] J. Xia, P. T. Beyersdorf, M. M. Fejer, and A. Kapitulnik, Appl. Phys. Lett. **89**, 062508 (2006).

[37] K. Uchida, T. Ota, H. Adachi, J. Xiao, T. Nonaka, Y. Kajiwara, G. E. W. Bauer, S. Maekawa, and E. Saitoh. J. Appl. Phys. **111**, 103903 (2012).

[38] C. J. Glassbrenner and G. A. Slack, Phys. Rev. **134**, A1058 (1964).

[39] N. L. Hecht, D. E. Mccullum, and G. G. A, Ceram. Eng. Sci. Proc. **9**, 1313 (1988).

[40] M. Faheem and K. Lynn, Am. J. Anal. Chem. **5**, 695 (2014).

[41] R. Berman, E. L. Foster, and J. M. Ziman, Proc. R. Soc. London. Ser. A. Math. Phys. Sci. **237**, 344 (1956).

[42] Hatami *et al.* Phys. Rev. Lett. **99**, 066603 (2007).

[43] M. Johnson and R. H. Silsbee, Phys. Rev. B **35**, 4959 (1987)

[44] M. Johnson, J. Supercond. **16**, 679 (2003).

[45] J.-E. Wegrowe, Phys. Rev. B **62**, 1067 (2000).

[46] Y. Tserkovnyak, A. Brataas, and G. Bauer. Phys. Rev. Lett. **88**, 117601 (2002).

[47] Arkhipov, V., Emelianova, E., Heremans, P., and Bässler, H. Phys. Rev. B **72**, 2–6 (2005).

[48] Baldo, M. and Forrest, S. Phys. Rev. B **64**, 1–17 (2001).

[49] Behrends, J. *et al*. J. Non. Cryst. Solids **354**, 2411–2415 (2008).

[50] Behrends, J., Lips, K., and Boehme, C. Phys. Rev. B - Condens. Matter Mater. Phys. **80**, 1–8 (2009).

[51] Boehme, C., Behrends, J., Maydell, K., Schmidt, M., and Lips, K. J. Non. Cryst. Solids **352**, 1113–1116 (2006).

[52] Boulitrop, F. Phys. Rev. B **28**, 6192–6208 (1983).

[53] M. Mews *et al.* Appl. Phys. Lett. **105**, 122113 (2014).

[54] Brodsky, M. H. and Title, R. S. Phys. Rev. Lett. **23**, 581–585 (1969).

[55] Dersch, H., Schweitzer, L., and Stuke, J. Phys. Rev. B **28**, (1983).

[56] Fuhs, W. J. Non. Cryst. Solids **354**, 2067–2078 (2008).

[57] Gliesche, A. *et al*. Phys. Rev. B - Condens. Matter Mater. Phys. **77**, 1–7 (2008).

[58] Herring, T. W. *et al*. Phys. Rev. B - Condens. Matter Mater. Phys. **79**, 1–5 (2009).

[59] Homewood, K. P., Cavenett, B. C., Spear, W. E. and LeComber, P. G. J. Phys. C Solid State Phys. **16**, 427–431 (1983).

[60] Juška, G., Arlauskas, K., Viliūnas, M., and Kočka, J. Phys. Rev. Lett. **84**, 4946–4949 (2000).

[61] Kato, Y., Myers, R. C., Gossard, A. C., and Awschalom, D. D. Nature **427**, 50–53 (2004).

[62] Lee, S. Y. *et al*. Appl. Phys. Lett. **97**, 97–100 (2010).

[63] Lips, K., Boehme, C., and Ehara, T. J. Optoelectron. Adv. Mater. **7**, 13–24 (2005).

[64] Lips, K. and Fuhs, W. J. Appl. Phys. **74**, 3993–3999 (1993).

[65] Mell, H., Mavaghar, B., and Schweitzer, L. Phys. Status Solidi Basic Res. **88**, 531–535 (1978).

[66] Müller, J. G. *et al*. Phys. Rev. B - Condens. Matter Mater. Phys. **72**, 1–10 (2005).

[67] Oheda, H. J. Appl. Phys. **101**, (2007).

[68] Overhof, H. J. Non. Cryst. Solids **227**, 15–22 (1998).

[69] Pankove, J. I. and Carlson, D. E. Mater. Sci. **10**, 43–63 (1980).

[70] Pfost, D., Liu, H., Vardeny, Z., and Tauc, J. Phys. Rev. B **30**, (1984).

[71] Proctor, C. M., Kuik, M., and Nguyen, T.-Q. Prog. Polym. Sci. **38**, 1941–1960 (2013).

[72] Schnegg, A., Behrends, J., Fehr, M., and Lips, K. Phys. Chem. Chem. Phys. **14**, 14418–38 (2012).

[73] Scott, J. C. J. Vac. Sci. Technol. A Vacuum, Surfaces, Film. **21**, 521 (2003).

[74] Shklovskii, B. I., Fritzsche, H., and Baranovskii, S. D. Phys. Rev. Lett. **62**, (1989).

[75] Stachowitz, R., Schubert, M., and Fuhs, W. Phys. Rev. B **52**, 10906–10914 (1995).

[76] Street, R. A. Phys. Rev. B **21**, 5775–5784 (1980).

[77] Street, R. A., Biegelsen, D. K., and Weisfield, R. L. Rev. B **30**, 5861–5870 (1984).

[78] Street, R. A., Cowan, S., and Heeger, a. J. Phys. Rev. B - Condens. Matter Mater. Phys. **82**, 11–13 (2010).

[79] Street, R. A. and Schoendorf, M. Phys. Rev. B **81**, 1–12 (2010).

[80] Street, R. A. and Biegelsen, D. K. J. Non. Cryst. Solids **35**, 651–656 (1980).

[81] Stutzmann, M., Brandt, M. S., and Bayerl, M. W. 266–269, 1–22 (2000).

[82] Taylor, P. C. Journ. Non. Cryst. Solids **352**, 839–850 (2006).

[83] Thomas, P. A., Brodsky, M. H., Kaplan, D. and Lepine, D. Phys. Rev. B **18**, 3059–3073 (1978).

[84] Tiwari, S. and Greenham, N. C. Opt. Quantum Electron. **41**, 69–89 (2009).

[85] Umeda, T., Yamasaki, S., Isoya, J., and Tanaka, K. Phys. Rev. B - Condens. Matter Mater. Phys. **62**, 15702–15710 (2000).

[86] Umeda, T., Yamasaki, S., Isoya, J., Matsuda, A., and Tanaka, K. J. Non. Cryst. Solids 227–230, 353–357 (1998).

[87] Ur Rehman Sagar, R., Zhang, X., Wang, J., and Xiong, C. J. Appl. Phys. **115**, 123708 (2014).

[88] J. Xia *et al.* Appl. Phys. Lett. **89**, 062508 (2006).

[89] Wang, J., Zhang, X., Wan, C., Vanacken, J., and Moshchalkov, V. V. Carbon N. Y. **59**, 278–282 (2013).

[90] Wilson, B. A., Hu, P., Harbison, J. P., and Jedju, T. M. Phys. Rev. Lett. **50**, 1490–1493 (1983).

[91] Yamasaki, S., Okushi, H., Matsuda, A., Tanaka, K. and Isoya, J. Phys. Rev. Lett. **65**, 756–759 (1990).

[92] Zhang, Z. *et al*. Renew. Energy **63**, 145–152 (2014).

[93] Georges Sagnac. Comptes Rendus **157** (1913), S. 708-710

[94] P. N. Argyres, Phys. Rev. **97**, 2 (1995).

[95] Xia, J. *et al*., Phys. Rev. Lett. **97**, 167002 (2006).

[96] Xia, J. Ph.D. dissertation, Stanford University, (1997).

[97] Dyakonov, M.I., Perel, V.I. Phys. Lett. A. **35** 459 (1971).

[98] An. Z. *et al.* Scientific Reports **2**, 388 (2012).

[99] M.-H. Kim, V. Kurz, G. Acbas, C. T. Ellis, and J. Cerne, J. Opt. Soc. Am. B **28**, 199-207 (2011)

[100] P. W. Anderson Phys. Rev. **109**, 1492 (1958)

[101] Mott, N.F. Phil. Mag. **19**: 835. (1969)

[102] VS Zapasskii *et al.* Phys. Rev. Lett. **110** (17), 176601 (2013)

[103] S. A. Crooker, D. D. Awschalom and N. Samarth, IEEE Journal of Selected Topics in Quantum Electronics **1**, 4, 1082-1092 (1995).

[104] P. Jansen *et al.* Nature Communications **4**, 2286 (2013).

[105] C. Zhang *et al.* Nature Physics **11**, 427–434 (2015)

[106] S.P. Kersten *et al.* Phys. Rev. Lett. **106**, 197402 (2011).

[107] Staebler, D. L. and Wronski, C. R. Applied Physics Letters. **31** (4): 292. (1977).

[108] Cutler, M. and Mott, N. Physical Review. **181** (3): 1336. (1969).

[109] A L Efros and B I Shklovskii , J. Phys. C8, L49 (1975).

[110] Herve Lefevre, *The Fiber-Optic Gyroscope*, (Artech House Publishers, 1993).

[111] R.C. Chittick *et al.* J. Electrochem. Soc. **116**, 77-81 (1969).